Modelling Ionospheric vertical drifts over the African low latitude region

A thesis submitted in fulfilment of the

requirements for the degree of

DOCTOR OF PHILOSOPHY

of

RHODES UNIVERSITY

by

Makhosonke Berthwell Dubazane

15 December 2017

Abstract

Low/equatorial latitudes vertical plasma drifts and electric fields govern the formation and changes of ionospheric density structures which affect space-based systems such as communications, navigation and positioning. Dynamical and electrodynamical processes play important roles in plasma distribution at different altitudes. Because of the high variability of $\mathbf{E} \times \mathbf{B}$ drift in low latitude regions, coupled with various processes that sometimes originate from high latitudes especially during geomagnetic storm conditions, it is challenging to develop accurate vertical drift models. This is despite the fact that there are very few instruments dedicated to provide electric field and hence $\mathbf{E} \times \mathbf{B}$ drift data in low/equatorial latitude regions. To this effect, there exists no ground-based instrument for direct measurements of $\mathbf{E} \times \mathbf{B}$ drift data in the African sector. This study presents the first time investigation aimed at modelling the long-term variability of low latitude vertical $\mathbf{E} \times \mathbf{B}$ drift over the African sector using a combination of Communication and Navigation Outage Forecasting Systems (C/NOFS) and ground-based magnetometer observations/measurements during 2008-2013. Because the approach is based on the estimation of equatorial electrojet from ground-based magnetometer observations, the developed models are only valid for local daytime. Three modelling techniques have been considered. The application of Empirical Orthogonal Functions and partial least squares has been performed on vertical $\mathbf{E} \times \mathbf{B}$ drift modelling for the first time. The artificial neural networks that have the advantage of learning underlying changes between a set of inputs and known output were also used in vertical $\mathbf{E} \times \mathbf{B}$ drift modelling. Due to lack of $\mathbf{E} \times \mathbf{B}$ drift data over the African sector, the developed models were validated using satellite data and the climatological Scherliess-Fejer model incorporated within the International Reference Ionosphere model. Maximum correlation coefficient of ~ 0.8 was achieved when validating the developed models with C/NOFS $\mathbf{E} \times \mathbf{B}$ drift observations that were not used in any model development. For most of the time, the climatological model overestimates the local daytime vertical $\mathbf{E} \times \mathbf{B}$ drift velocities. The methods and approach presented in this study provide a background for constructing vertical $\mathbf{E} \times \mathbf{B}$ drift databases in longitude sectors that do not have radar instrumentation. This will in turn make it possible to study day-to-day variability of vertical $\mathbf{E} \times \mathbf{B}$ drift and hopefully lead to the development of regional and global models that will incorporate local time information in different longitude sectors.

Acknowledgements

Publications from this thesis

1. Dubazane M. B., J. B. Habarulema and J.C. Uwamahoro (2017); Modelling ionospheric vertical drifts over Africa low latitudes using Empirical Orthogonal functions and comparison with climatological model; Advances in Space Research 61(1), 326-336. This paper used the expression developed by Anderson et al. (2004) to derive vertical $\mathbf{E} \times \mathbf{B}$ drift based on magnetometer observations (ΔH) over the African sector. The derived vertical $\mathbf{E} \times \mathbf{B}$ drift data was later used in modelling with the help of Empirical Orthogonal Functions for the first time. Details on this paper are presented in Chapter 4.

2. Dubazane, M. B. and Habarulema, J. B. (2017); An empirical Model of vertical Plasma drift over the African sector, Space Weather (Under Review). This paper dealt with the development of the mathematical relationship between C/NOFS vertical $\mathbf{E} \times \mathbf{B}$ drift and magnetometer observations (ΔH) over the African sector. The developed expression was then used to derive the long-term local daytime vertical $\mathbf{E} \times \mathbf{B}$ drift as a function of magnetometer (ΔH) data. The resulting dataset was used in modelling by utilisation of partial least squares and neural network techniques. Details are presented in Chapter 5.

Contents

Acronyms and Abbreviations

AE	Atmospheric Explorer
ANN	Artificial neural network
CERTO	Coherent Electromagnetic Radio Tomography
CHAMP	CHallenging Minisatellite Playload
CINDI	Coupled Ion-Neutral Dynamics Investigation
CITP	Coupled Ionosphere-Thermosphere-Plasmasphere
CIR	Corotating Interaction Region
C/NOFS	Communications/Navigation Outage Forecasting System
CME	Coronal Mass Ejections
DE	Dynamics Explorer
DMSP	Defense Meteorological Satellite Program
EEJ	Equatorial electro-jet
EIA	Equatorial ionization anomaly
EOF	Empirical Orthogonal Function
EUV	Extreme ultra violet
FAC	Field aligned current
GPS	Global positioning system
IMF	Interplanetary magnetospheric field
IRI	International Reference Ionosphere
ISR	Incoherent scatter radar
IVM	Ion velocity meter
JULIA	Jicamarca Unattended Long-term studies of the Ionosphere and Atmosphere
LS	Least squares
LT	Local time

MAD	Median absolute deviation
NIPALS	Non-linear Iterative Partial Least Squares
NN	Neural network
PC	Principal component
PLP	Planar Langmuir Probe
PLS	Partial least squares
PRE	Pre-reversal enhancement
QBO	Quasi-Biennal Oscillation
RMS	Root Mean Square
RMSE	Root mean square error
ROCSAT	Republic of China Satellite
SFU	Solar flux unit
SIMPLS	Statistical Inspired Modification-Partial Least Squares
Sq	Solar quiet
SSN	Solar spot number
TEC	Total electron content
TIEGCM	Thermosphere-Ionosphere-Electrodynamic General Circulation Model
TID	Travelling ionspheric disturbance
UT	Universal time
VEFI	Vector electric field instrument

Chapter 1

Introduction

Low/equatorial latitude ionospheric changes are controlled by both dynamic and electrodynamic processes. For-example, vertical coupling between low and higher altitude regions exhibit influences from E-region migrating and non-migrating tides' effect on the electric field and this varies longitudinally (Millward et al., 2001; Lühr et al., 2008). Electro-dynamical processes mainly arise from changes in solar quiet-day (Sq) wind dynamo current system within the E-region (90-120 km) partly due to differential heating of the Earth's atmosphere (e.g., Richmond, 1973; Immel et al., 2006a). Continuous changes in the wind dynamo current system and the orientation of the Earth's magnetic field in the equatorial regions result in Lorentz force which is the primary factor in determining the latitudinal distribution of plasma in low latitudes (Anderson, 1973; Sastri, 1990). Therefore, equatorial vertical $\mathbf{E} \times \mathbf{B}$ drift and dynamo electric field $\mathbf{E}$ in the E- and F-region ionosphere are important parameters driving low latitude electrodynamics (e.g., Rishbeth, 1971, 1997; Fejer, 2011). Vertical drifts are mainly driven by complex interactions of E- and F-regions processes which vary substantially with the solar cycle, season, local time, geomagnetic activity and longitude (e.g., Fejer et al., 1979; Fejer, 1997). During quiet geomagnetic conditions, daytime $\mathbf{E} \times \mathbf{B}$ drift is mostly upward and reverses to downward during the nighttime (e.g., Scherliess and Fejer, 1999; Kil et al., 2007). However, ionospheric disturbance dynamo and solar wind-magnetospheric electric fields significantly affect vertical drifts during geomagnetic active periods (e.g., Scherliess and Fejer, 1997). Prompt penetrating electric fields during the southward turning of the interplanetary magnetic field z component (IMF Bz) usually enhances the eastward electric field during the local daytime and are westward during nighttime causing further downward drift in equatorial latitude regions (e.g., Spiro et al., 1988; Fejer and Scherliess, 1995;

Peymirat et al., 2000). Electric fields due to ionospheric disturbed dynamo are westward and eastward during local daytime and nighttime respectively (Blanc and Richmond, 1980; Sastri, 1988; Scherliess and Fejer, 1997; Fejer and Emmert, 2003). There is therefore a complex variability of low latitude vertical $\mathbf{E} \times \mathbf{B}$ drifts with local time and in different longitudes due to different contributions relating mainly to effects of E region tides on the electric field (e.g., Millward et al., 2001; Lühr et al., 2004; Maute et al., 2012), coupling between E and F-region electrodynamical phenomena (e.g., Heelis et al., 1974; Richmond, 1995a; Anderson, 1973), geomagnetic activities especially on short-time scales during disturbed conditions (e.g., Fejer et al., 1979; Gonzales et al., 1979; Fejer, 1997; Scherliess and Fejer, 1997) and solar activity on long-term scale in different seasons (e.g., Fejer et al., 1991; Chandra et al., 1997). Understanding the variability of vertical $\mathbf{E} \times \mathbf{B}$ drifts is critical for both scientific and practical purposes such as the ones which involve the use of communication and navigation applications (Anderson et al., 2004). Due to the nature and dynamics of different contributors to vertical $\mathbf{E} \times \mathbf{B}$ drifts, it is important to develop models in different longitude regions as a result of unusual observations made over time. For-example, it has been observed and reported that vertical $\mathbf{E} \times \mathbf{B}$ drifts are higher in the American sector than in the African sector and yet the latter experiences more ionospheric irregularities (e.g, Yizengaw et al., 2014b).

Despite the demonstrated importance of vertical $\mathbf{E} \times \mathbf{B}$ drift, direct observations of low latitude electric field are very scarce, only available in few longitude sectors. The only place where day-to-day direct measurements of low latitude vertical drifts are made is Jicamarca (11.8°S, 77.2°W; 0.8°N geomagnetic) where there is an incoherent scatter radar (ISR) that has been in existence since 1960s (Woodman and Hagfors, 1969). However due to operational costs, the radar is not run on a continuous basis through out the year. Advances have been made in using other instrumentation to monitor day-to-day vertical $\mathbf{E} \times \mathbf{B}$ variability. Results showing that Doppler velocities of 150 km echoes were a representation of F-region vertical $\mathbf{E} \times \mathbf{B}$ drifts and changes in equatorial electrojet derived from ground-based magnetometer measurements (e.g., Kudeki and Fawcett, 1993; Chau, 1998; Woodman and Villanueva, 1995; Chau and Woodman, 2004) have broadened the data coverage of low latitude vertical drift studies in some longitude sectors such as India and Indonesia (e.g., Patra and Rao, 2006; Patra et al., 2008, 2012) during local daytime. To date, there exists no direct vertical drifts in the African sector using ground-based instrumentation such as ISR or the operational back scatter radars in India and Indonesia (Patra and Rao, 2006; Patra et al., 2008) that

provide 150 km echoes during local daytime. Inference of the changes in vertical $\mathbf{E} \times \mathbf{B}$ drifts over the African sector is usually done using empirical models such as the one developed using Jicamarca ISR data along with space based observations from the Atmospheric Explorer (AE) and Republic of China Satellite (ROCSAT-1) which are climatological in nature (Scherliess and Fejer, 1997, 1999; Fejer et al., 2008). There also exists theoretical models which estimate vertical $\mathbf{E} \times \mathbf{B}$ drifts globally when provided with relevant inputs/parameters. Examples of these are the thermosphere-ionosphere-electrodynamic general circulation model (TIEGCM) which self consistently solves the thermosphere-ionosphere dynamics from first principles (Richmond et al., 1992) and the thermosphere/ionosphere general circulation model (CTIP) that couples the thermosphere and ionosphere while allowing inclusion of tidal forcing (Millward et al., 2001).

Other low latitude vertical drift investigations in the African sector which are mainly case studies determine $\mathbf{E} \times \mathbf{B}$ drifts using virtual height observations from ionosonde data (e.g., Bilitza et al., 2004; Oyekola and Oluwafemi, 2007; Adebesin et al., 2013; Grodji et al., 2017) and EEJ with the help of ground-based magnetometers (e.g., Doumouya et al., 1998, 2003; Haile, 2003; Rabiu et al., 2011; Yizengaw et al., 2012; Habarulema et al., 2016). The utilization of magnetometer observations relies on the differential approach where observations at the equator and away from the equator (6-9 degrees) are subtracted to obtain a proxy of daytime vertical $\mathbf{E} \times \mathbf{B}$ drifts (e.g., Rastogi and Klobuchar, 1990; Anderson et al., 2004). This gives what is normally known as $\triangle H$ (nT) derived from horizontal components of the Earth's magnetic field data at the two magnetometer stations; which is directly related to the vertical $\mathbf{E} \times \mathbf{B}$ drift during local daytime. Therefore $\triangle H$ refers to variation of field values detected by magnetometer at equatorial latitude which are subsequently used for deriving vertical plasma drifts. It has also been demonstrated that in situ satellite observations from the Communications and Navigation Outage Forecasting System (C/NOFS) can be used to study climatological changes in vertical $\mathbf{E} \times \mathbf{B}$ drifts (e.g., Rodrigues et al., 2011; Stoneback et al., 2011; Yizengaw et al., 2014a). Satellite data provide the extended global coverage, but are non-continuous over particular longitude sectors and local time and are hence more suitable for developing climatological models. On the other hand, ground-based magnetometer data is continuous and with high temporal resolution in addition to being inexpensive to maintain and operate a magnetometer. In this thesis, efforts to model vertical $\mathbf{E} \times \mathbf{B}$ drifts over the African sector using local African data have been attempted for the first time. A combination of ground-based magnetometer and C/NOFS observations have been used

during the period 2008–2013 when magnetometers were simultaneously operational in the African low latitude region.

1.1 Aims and Objectives

The overall aim of the study is to investigate possibilities of modelling vertical $\mathbf{E} \times \mathbf{B}$ drifts over the African low latitude region using local data. This first involved a detailed review of $\mathbf{E} \times \mathbf{B}$ drift studies in low/equatorial over other longitude sectors to benchmark the requirements for the African region investigation. The specific objectives included

- Consolidation and processing of magnetometer observations over the African low latitude region in a format suitable for estimation of vertical $\mathbf{E} \times \mathbf{B}$ drift

- Investigation of different approaches used in $\mathbf{E} \times \mathbf{B}$ drift modelling along with the relevant inputs

- Development of the mathematical expression relating in situ satellite (C/NOFS) vertical $\mathbf{E} \times \mathbf{B}$ drifts and magnetometer derived EEJ over the African sector, for the first time.

It is important to mention that there are no previous vertical $\mathbf{E} \times \mathbf{B}$ drift modelling studies that concentrated on the African sector for comparisons and therefore the comparative analysis of the results was performed using outputs from the global Scherliess-Fejer (SF) model (Scherliess and Fejer, 1999).

1.2 Overview of the thesis

The thesis has six chapters. Chapter 1 has provided an introduction to the study and the broad motivation/objectives that necessitated us to carry out this investigation. Chapter 2 provides the brief background theory about the ionosphere and a relatively detailed treatment of the low latitude electrodynamics. In Chapter 3, measurements and modelling techniques are described. Measurements include C/NOFS vertical $\mathbf{E} \times \mathbf{B}$ drift observations over equatorial region and necessary data processing steps. Moreover the procedure followed in estimating the EEJ from magnetometer data is also described. Some details of modelling techniques that have been employed in the thesis (empirical orthogonal functions, partial least squares and artificial neural networks) are provided.

Chapter 4 describes the application of empirical orthogonal functions on modelling vertical $\mathbf{E} \times \mathbf{B}$ drift for the first time. The source of the modelled data was based on the analytical empirical expression developed by Anderson et al. (2004) which was used to derive vertical $\mathbf{E} \times \mathbf{B}$ drift using magnetometer data over the African sector.

In Chapter 5, an expression relating C/NOFS vertical $\mathbf{E} \times \mathbf{B}$ drift velocities and magnetometer data (derived from the H-component, $\triangle H$) has been established. The developed expression is later used to derive $\mathbf{E} \times \mathbf{B}$ drift data for the entire $\triangle H$ data from 2008–2013 that is used to develop both partial least squares and neural network models using relevant physical and geophysical inputs. Chapter 6 provides a summary of the findings of the study and puts forward suggestions to improve on this research in future.

Chapter 2

Earth's Atmosphere, ionosphere and low latitude electrodynamics

2.1 Introduction

The rapid increase of space-based technologies with applications mainly in communications and navigation systems poses serious challenges for accurately predicting temporal and spatial variations of the ionospheric plasma and thus space weather forecasting (e.g., Fuller-Rowell et al., 1997; Fejer, 2011). Low latitude electric field $\mathbf{E}$ and vertical ionospheric vertical drifts play significant role in the dynamics of the ionosphere. At equatorial ionosphere, a daytime eastward $\mathbf{E}$ drives ionospheric vertical drifts and equatorial electrojet (EEJ) current which are processes governing the ionospheric composition and distribution leading to the generation of plasma waves and density structures. Morphology of vertical $\mathbf{E} \times \mathbf{B}$ drift has been studied extensively over the South American sector with incoherent and coherent scatter radar measurements (e.g., Woodman and Hagfors, 1969; Kudeki and Fawcett, 1993; Chau, 1998). However, over the African sector, fewer studies of vertical $\mathbf{E} \times \mathbf{B}$ drift derived from ionosonde measurements (e.g., Oyekola and Oluwafemi, 2007; Adebesin et al., 2013) and daytime equatorial magnetic field from magnetometer observations (e.g., Yizengaw et al., 2012) have been undertaken. Launching of satellites such as Atmospheric Explorer-E (AE-E) and Republic of China Satellite (ROCSAT-1)(e.g., Su et al., 1999), Dynamics Explorer-B (DE-2) (Coley and Heelis, 1989), Communications/Navigations Outage Forecasting Systems (C/NOFS) (de La Beaujardière et al., 2004; de La Beaujardiere et al., 2009) and CHallenging Minisatellite Playload (CHAMP) (Wickert et al., 2001) into space provided an op-

portunity to study the longitudinal variability of vertical $\mathbf{E} \times \mathbf{B}$ drift, EEJ, spread-F, electron density and total electron content (TEC) (e.g., Su et al., 1999; Lühr et al., 2004; Fejer et al., 2008; Fejer, 2011). Empirical models of vertical $\mathbf{E} \times \mathbf{B}$ drift are mainly based on radar measurements and satellite observations (e.g., Batista et al., 1996; Scherliess and Fejer, 1997, 1999; Fejer et al., 2008; Alken, 2009). Numerical modelling efforts include the SAMI2 (Sami2 is Another Model of the Ionosphere) (Huba et al., 2000), Coupled Thermosphere-Ionosphere-Plasmasphere (CTIP)(e.g., Millward et al., 1996), and time-dependent National Center for Atmospheric Research (NCAR) models (Thermosphere-Ionosphere-Electrodynamics General Circulation Model, TIE-GCM or Thermosphere Ionosphere Mesosphere Electrodynamics General Circulation Model, TIME-GCM) (Richmond et al., 1992). The following sections will briefly introduce the atmosphere/ionosphere and comprehensively discuss the fundamental ionospheric vertical drifts from E and F region dynamos and the associated changes in ionospheric currents which is the major focus of this thesis.

2.2   The Earth's Atmosphere

The atmosphere is a highly variable medium and extends from the surface of the Earth to many orders of kilometers above it. It is relatively dense near the Earth's surface and consists of gases such as oxygen (O_2), nitrogen (N_2), while traces of carbon dioxide (CO_2), various other gases and water also exist. Characteristics and properties of the atmosphere such as composition, pressure, temperature and ion/electron density have been shown to largely depend on altitude, latitude, longitude and season (Hargreaves, 1992; Schunk and Nagy, 2009; Kelley, 2009). Temperature gradient divides the neutral atmosphere into distinct layers known as troposphere, stratosphere, mesosphere, and thermosphere. Figure 2.1 shows temperature and plasma density profiles at different altitudes (Kelley, 2009). The distinction between daytime and nighttime is obvious on plasma density profile.

Characteristics and properties of the atmospheric layers are different. In the troposphere, the temperature decreases with altitude at a rate of $\sim$ 7 K/km, while temperature increases with altitude in the stratosphere due to absorption of mainly solar ultra-violet radiation by ozone layer (e.g., Hines, 1965; Finlayson-Pitts and Pitts Jr, 1999; Craig, 2016). Temperature in the
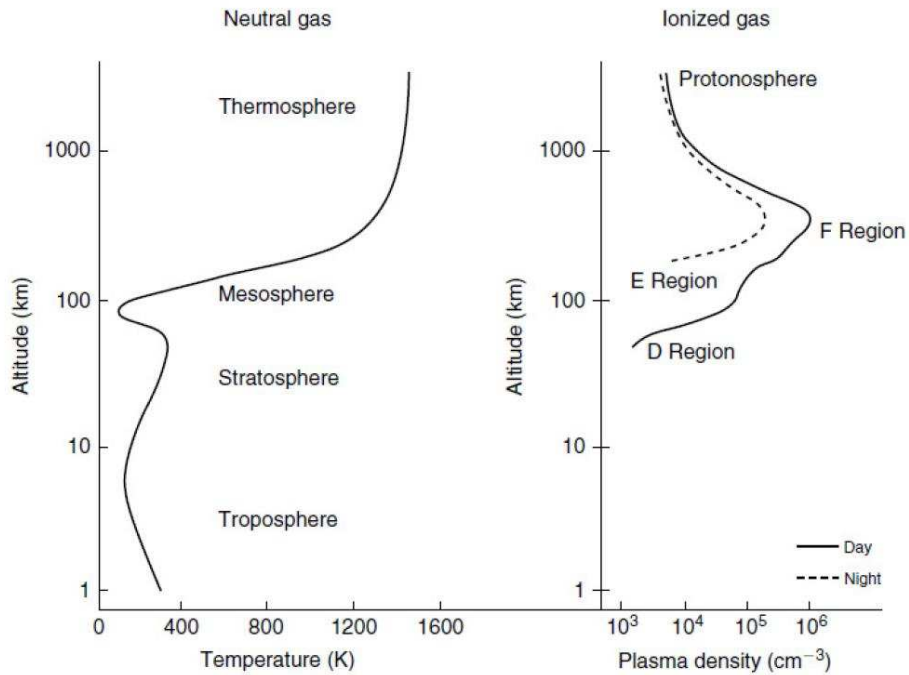
Figure 2.1: Temperature distribution of neutral atmosphere with altitude (left). Plasma density profile with altitude during daytime and nighttime (right) (Kelley, 2009).

mesosphere decreases with altitude mainly because of radiative cooling, while in the thermosphere the temperature rises exponentially with altitude reaching a steady value of about 1000 K near 500 km (e.g., Kelley, 2009). In this altitude range, neutral particles maintain diffusive equilibrium, thus the vertical distribution of the neutrals is governed by respective masses of the species (Rees, 1989).

2.3 Ionosphere

Characteristics and properties of ionosphere depend on longitude, season, altitude, local time, solar and magnetic activities (Davies, 1990). While the neutral species are the main constituents at low altitudes (neutral species density decreases with altitude), solar ultra-violet radiation and X-ray emissions penetrate into neutral atmosphere causing photo-ionization and heating of atmospheric species to steady temperature (generally over 1000 K) from an altitude of about 500 km (Hargreaves, 1992; Kelley, 2009). Although, the proportion of charged particles is very small ($\sim 1\%$) in comparison with neutral species, they significantly affect properties and behavior of the atmosphere (e.g., Richmond, 1995d). Since atmospheric layers at different altitudes absorb

different amount of solar energies, the ionosphere is layered into D ($\sim$ 60-90 km), E ($\sim$ 90-150 km) and F ($\sim$ 150-500 km) regions as shown in Figure 2.1. The D and E regions ionosphere are dominated by photo-chemical processes (e.g., Rishbeth and Garriott, 1969). Higher pressure in the D region enables both major and minor species to participate in photo-ionization processes. This layer is generated when NO absorbs X-rays (0.1–0.8 nm), H Ly α (121.6 nm) and cosmic rays. The D region is responsible for the absorption of high frequency radio waves (Ondo and Marubashi, 2000). Typical electron densities in the D layer are in the range $10^2 - 10^4$ cm^{-3} during daytime and negligible at nighttime (Kelley, 2009).

Unlike the D region ionosphere, the E region consists of NO^+ and O_2^+ ions and is dominated by the transport processes which re-distribute electrons and ions to higher altitudes (Seaton, 1955). Ionization in the E region ionosphere is mainly via soft X-rays (0.8–14 nm), Ly β and UV radiations of wavelengths in the range 79.6–102.7 nm (Rishbeth and Garriott, 1969). The typical electron densities are $\sim 10^5$ cm^{-3} and 10^4 cm^{-3} during daytime and nighttime (Hargreaves, 1992), respectively.

Daytime F region ionosphere is defined by two sub-regions, $F1$ (150-250 km) and $F2$ (250-500 km). While production and loss of charged species are still more dominant in the $F1$ region, production and transport processes dominate in the $F2$ region ionosphere (e.g., Rishbeth and Garriott, 1969; Schunk and Nagy, 2009). From F1 layer to about 600 km, the ionosphere is dominated by atomic oxygen ions (O^+). The typical electron densities in $F1$ layer are $10^5 - 10^6$ cm^{-3} during daytime and negligible during nighttime. Typical electron densities of the $F2$ layer are 10^6 cm^{-3} and 10^5 cm^{-3} during daytime and nighttime (Hargreaves, 1992; Kelley, 2009), respectively.

Ionospheric sounding based instruments such as ionosonde and radars have been used in the study of E, $F1$ and $F2$ ionospheric layers since 1920s (e.g., Breit and Tuve, 1926; Villard, 1976; Adams et al., 1986; Vincent and Lesicar, 1991). In the case of ionosonde, the resulting ionograms show critical frequencies of the layers ($f_\circ E$, $f_\circ F1$ and $f_\circ F2$) which are measure of the maximum electron densities of the respective layers (e.g., Smith and Kirby, 1937; Davies, 1990). Since the electron density changes with time and altitude, the critical frequencies and other electron density parameters are used in the ionospheric plasma studies at different heights. The D region ionosphere has lower density and thus has been studied with instruments such as rockets (Mechtly and Smith, 1968; Sechrist, 1968). Recent measurements of D layer involve using broadband VLF and low-frequency (30–300 kHz) radio signals from lightning discharges (e.g.,

Cummer et al., 1998; Lay and Shao, 2011). Nowadays, satellites such as C/NOFS, ROCSAT, CHAMP and DMSP are commonly used to study the ionosphere at different heights and longitudes (e.g., Su et al., 1999; Lühr et al., 2004; de La Beaujardiere et al., 2009; Fejer et al., 2008; Fejer, 2011)

2.3.1 Ionospheric variability

As mentioned earlier, ionospheric variability depends on solar activity, season, latitude, longitude, local time and geomagnetic activity (Davies, 1990). Long- and short-term variability studies of the ionosphere have been possible through monitoring the spatial and temporal electron density changes over some extended time (Davies, 1990). Among these dependencies, activities of the Sun mostly govern the ionospheric variability. The major factors influencing the ionospheric variability are briefly described as follows,

- Diurnal variation:

  - Day-night electron density varies as a result of the Earths rotation with respect to the Sun (Chapman, 1931). Large EUV and X-ray radiations from the Sun cause large electron density during the daytime compared to nighttime where photo-ionization is absent (Chapman, 1931; Rishbeth and Garriott, 1969; Kelley, 2009). Since solar radiation ionizes neutral species, which then dissociate into electrons and corresponding positive ion species, recombination greatly reduces the electron density during the night, but some free electrons still remain until dawn (McNamara, 1991).

- Solar activity:

  - Intensity of the 10.7 cm radio flux, rate at which flares occur and sunspot number (SSN) on the solar disk change with the activity of the Sun going through a 11-year cycle (Davies, 1990). Solar cycle defines periods of high and low ionospheric variability based on the levels of photo-ionization. Figure 2.2 shows the long-term variation of total electron content (TEC) with solar spot number (SSN). Generally, high and low electron density values are expected during high and low solar activity periods respectively.
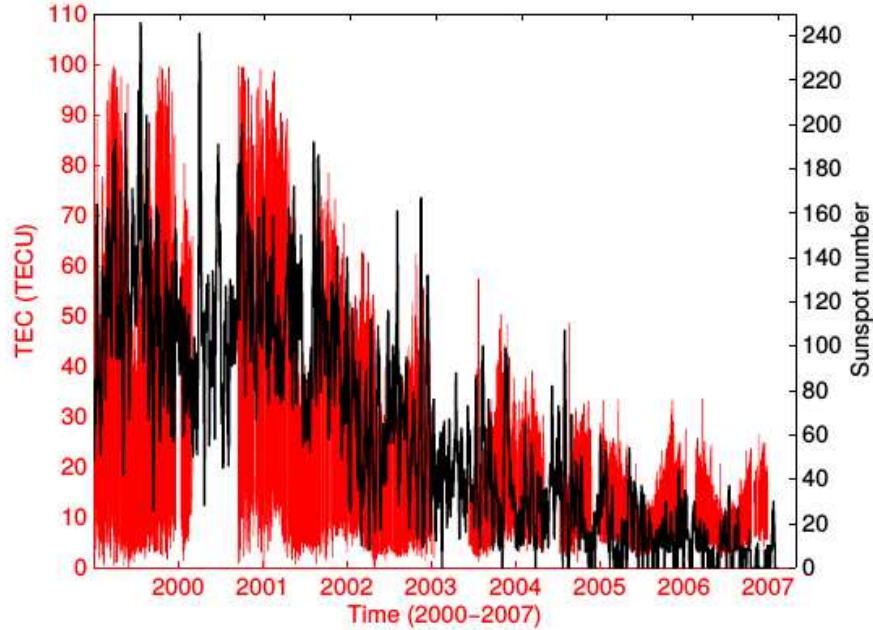
- Latitudinal variation:

Figure 2.2: Variation of sunspot number (black curve) and TEC observations (red curve) over Sutherland (32.38°S,20.81°E) during 2000-2007 (Habarulema, 2011).

– The Sun is irradiating directly overhead at geographic equator, while the solar radiation arrives at an oblique angle at other latitudes away from equator (Chapman, 1931). Hence, we expect large decrease of ionospheric ionization as the Sun moves far from the equator. The solar zenith angle (SZA) determines the ionization levels over a range of latitudes, thus geographic locations with low SZA are expected to show higher electron densities (McNamara, 1991). Figure 2.3 shows the latitudinal variation of ionospheric plasma using the total electron content (TEC) during the quiet (left) and disturbed (right) conditions in July 2017. Large enhancement in TEC variation are observed during disturbed geomagnetic condition (2017-07-16) than quiet time period (2017-07-05) and the variability extends to midlatitude regions. Vertical $\mathbf{E} \times \mathbf{B}$ drift and therefore EEJ govern the ionospheric variability at low/equatorial latitude regions. Since the equatorial electrojet (EEJ) and therefore vertical $\mathbf{E} \times \mathbf{B}$ drift are typical features of low/equatorial latitude ionosphere (Baker and Martyn, 1952; Hirono, 1952), they influence electron density distribution during both quiet and disturbed conditions. For example, ions and electrons lifted to higher altitudes by vertical $\mathbf{E} \times \mathbf{B}$ drift diffuse along magnetic field $\mathbf{B}$ resulting in equatorial ionization anomaly (EIA) formation at

11

$15° − 18°$ from geomagnetic equator (Anderson, 1981; Sastri, 1990). The EIA can extend towards mid latitude regions during storm conditions.

- Seasonal variation:

    - Due to changing orientation of the Sun with respect to the Earth's axis, high electron density values are generally observed around the equinoxial months (March and September) and in summer, while low values are seen in winter (Chapman, 1931). Although one may expect large electron densities in the ionosphere (for both hemispheres) during summer than in winter, this may not be necessarily true since the neutral atmospheres composition also exhibits seasonal variations (e.g., McNamara, 1991; Balan et al., 1998; Meggs, 2005). Large electron density during equinoxes (in March and September) occurs during both solar maximum and minimum (McNamara, 1991).

- Geomagnetic activity:

    - The EUV radiation from the Sun governs the thermal convection at ionospheric heights, and thus leads to the movement of ions and electrons across the geomagnetic field **B**. Consequently, ionospheric currents are generated and they give rise to a magnetic field around the ionosphere, the variations of which are subsequently observed on the Earths surface as geomagnetic field fluctuations (Ondo and Marubashi, 2000). During periods of geomagnetic storms, the ionospheric electron density may get enhanced or reduced leading to either positive or negative storm effects depending on the nature/characteristics of disturbances and latitudes (Prölss, 1993; Prölss and Bird, 2004). The right panel of Figure 2.3 demonstrates that TEC was enhanced (compared to the quiet day 2017-07-05 at the same time of 12 UT) as a result of geomagnetic storm that occurred on 2017-07-16. This is an illustration of a positive storm effect.

2.4   Low latitude electrodynamics

Diurnal absorption of solar ultra-violet radiation governs changes in the thermospheric winds and therefore leads to the development of day-to-night pressure gradient (Jursa et al., 1985; Hargreaves, 1992). The thermosphere is a region of the atmosphere above ~ 100 km in which the ionosphere is
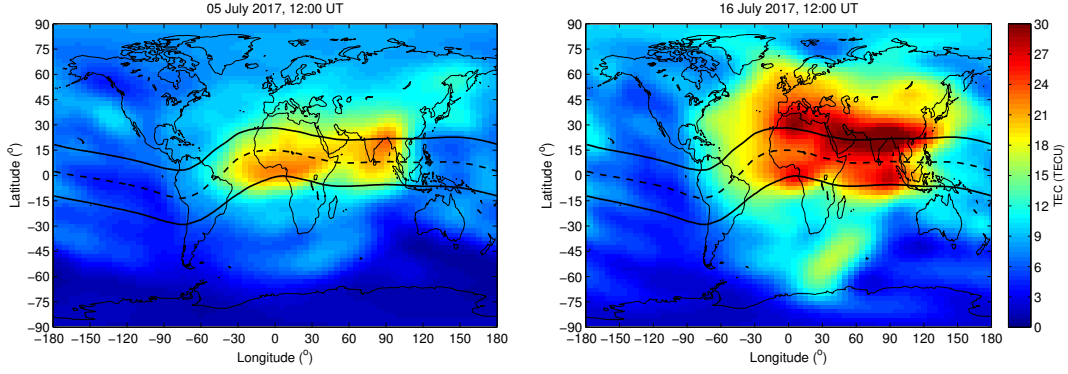
Figure 2.3: Global total electron content (TEC) map during quiet and disturbed periods in July 2017. Data source: ftp://cddis.gsfc.nasa.gov/pub/gps/products/ionex.

embedded. Thermospheric winds refer to neutral winds which are blowing at those high altitudes. Since the horizontal dimension (defined by zonal and meridional components) of the Earth's atmosphere is large in comparison with the vertical extent, winds and neutral motions considered are mainly in the horizontal direction. Meridional winds can move plasma up or down the geomagnetic field $\mathbf{B}$ (Krishna Murthy et al., 1990). Zonal winds are blowing westward during daytime and eastward during the nighttime. At high altitudes when collision rates are low, winds enable the electrons to move relative to the ions and thus generating electric fields and currents (Hargreaves, 1979), the resulting dynamo equations (Blanc and Richmond, 1980) can be defined as follows,

$$\mathbf{J} = \sigma_P \left(\mathbf{E}_\perp + \mathbf{u} \times \mathbf{B} \right) + \sigma_H \mathbf{b} \times \left(\mathbf{E} + \mathbf{u} \times \mathbf{B} \right) + \sigma_\circ \mathbf{E}_\parallel \tag{2.1}$$

$$\bigtriangledown \cdot \mathbf{j} = 0 \tag{2.2}$$

$$\mathbf{E} = - \bigtriangledown \phi \tag{2.3}$$

where σ_P, σ_H, $\sigma_\circ$ are Pedersen, Hall and direct conductivities; $\mathbf{E}_\parallel$ and $\mathbf{E}_\perp$ are parallel and perpendicular components of $\mathbf{E}$ with reference to geomagnetic field $\mathbf{B}$; $\mathbf{b}$ is unit vector parallel to $\mathbf{B}$, and thus showing direction of $\sigma_\circ$ which increases exponentially upwards but limited at great heights by ion-electron collisions; ϕ is the electrostatic potential. The Pedersen conductivity, σ_P, acts along the direction $\mathbf{E}$, but perpendicular to $\mathbf{B}$. It peaks at altitudes where the ratios $\left(\frac{\nu_i}{\omega_i} = \frac{\nu_e}{\omega_e} \approx 1 \right)$ for both ions and electrons are comparable and each nearly equals to unity which often occurs at altitudes around 125 km (Rishbeth, 1997). In the ratios above, ν_i and ω_i, refer to collision and gyro-frequencies for ions, respectively. Similarly, ν_e and ω_e are collision and gyro-frequencies for electrons. σ_H is described in the direction perpendicular to both $\mathbf{E}$ and $\mathbf{B}$. Near

magnetic equator where $\mathbf{B}$ is nearly horizontal, σ_H results from electrons moving in the $\mathbf{E} \times \mathbf{B}$ direction and peaks at around 105 km (Richmond, 1995c; Rishbeth, 1997).
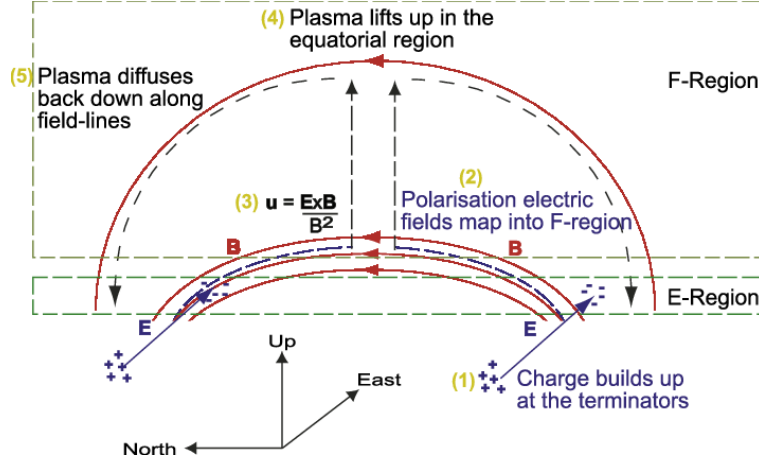

Figure 2.4: Schematic describing the evolution of the equatorial ionospheric anomaly (Immel et al., 2006b).

Figure 2.4 shows a schematic picture illustrating the dynamo action leading to ionospheric features such as fountain effect, EEJ and $\mathbf{E}$ and vertical $\mathbf{E} \times \mathbf{B}$ drift during daytime (Immel et al., 2006b). While the E region ionosphere has large conductivity (Hall conductivity) during daytime, the F region dynamo actions during daytime are suppressed and they operate rather differently (e.g., Rishbeth, 1977, 1997; Fang et al., 2008; Maute et al., 2012). E region dynamo action results in eastward electric field $\mathbf{E}$ which can be transferred into F region via equipotential $\mathbf{B}$ near magnetic equator (Heelis et al., 1974). The dynamo actions of E and F regions can be described as voltage and current generators, respectively. Given the westward zonal wind velocity $\mathbf{U}$ in the E and F regions, then the E region dynamo processes can be described as follows,

1. For neutral wind with velocity $\mathbf{U}$ blowing across the geomagnetic field $\mathbf{B}$, electric field $\mathbf{E}_I = \mathbf{U} \times \mathbf{B}$,

2. The field $\mathbf{E}_I$ drives a current, $\mathbf{j} = \boldsymbol{\sigma}(\mathbf{E}_I + \mathbf{E}_p)$, where $\boldsymbol{\sigma}$ is conductivity tensor and $\mathbf{E}_p$ is polarization electric field which originates from (i) a distribution of electrostatic charges to maintain divergence free currents ($\bigtriangledown \cdot \mathbf{j} = 0$) everywhere, and (ii) magnetospheric fields which reach the low latitude ionosphere through magnetic field from polar regions (Rishbeth, 1997).

If there is eastward $\mathbf{E}$ and is perpendicular to $\mathbf{B}$, Hall currents flow downward within the E region ionosphere. The Hall current which is carried by electrons, polarizes the E-region iono-
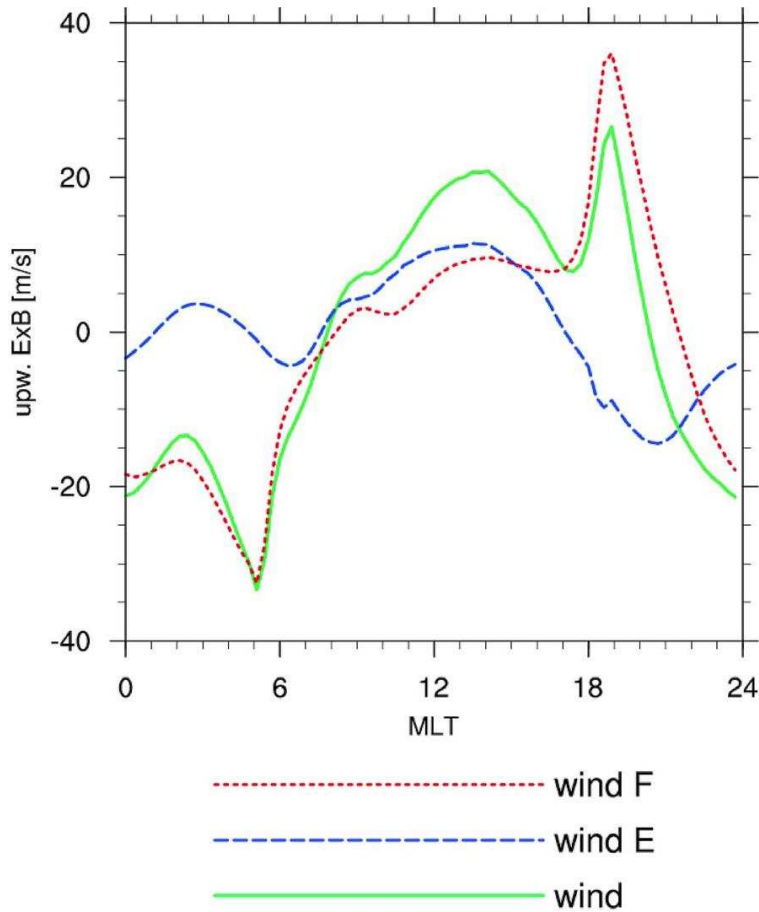
Figure 2.5: Simulated vertical $\mathbf{E} \times \mathbf{B}$ drift at 12 UT due to neutral winds (solid-green curve), neutral wind in the E-region below approximately 140 km (long dashed/blue curve) and neutral wind in the F region above approximately 140 km (short-dashed/red curve) (Maute et al., 2012).

sphere so that an upward directed polarization electric field ($\mathbf{E}_p$) is produced (Kelly, 1989). The Pedersen current due to the primary eastward electric field ($\mathbf{E}_I$) and the eastward Hall current due to the $\mathbf{E}_p$ and geomagnetic field $\mathbf{B}$, add up to yield a substantial eastward current known as equatorial electrojet (EEJ). It is a strip of enhanced current flowing within $\pm 3°$ of dip equator which causes large enhancement in the horizontal component of geomagnetic field (H) near the equator (Rastogi and Klobuchar, 1990).

Figure 2.5 shows results from simulations demonstrating the contribution of winds in the magnitude and direction of E and F regions vertical $\mathbf{E} \times \mathbf{B}$ drift (Maute et al., 2012). Diurnal variation of simulated $\mathbf{E} \times \mathbf{B}$ drift is represented with reference to geomagnetic longitudes, hence MLT=12 shows the variability at noon when the Sun is directly overhead. Similarly, MLT=0 or MLT=24 refers to positions where there is no solar irradiation. During nighttime, F region dynamos are

significant as the E region ionosphere significantly decreases. After sunset the polarization field in the F region is enhanced and results in vertical $\mathbf{E} \times \mathbf{B}$ drift reaching the velocity of winds ($\mathbf{U}$). Large enhancement of vertical drift around sunset is known as pre-reversal enhancement (PRE) and is attributed to zonal electric field associated with F region dynamo and Pedersen conductivity (Rishbeth, 1971). Therefore, the E region dynamo action is no longer effective after sunset. The large enhancement of $\mathbf{E} \times \mathbf{B}$ drift in Figure 2.5 during late hours may reflect a rapid decrease of Hall conductivity in comparison with Pedersen conductivity in the F region ionosphere (Rishbeth, 1997). Large polarization fields in F region also increases the wind speed during the nighttime (Rishbeth, 1971). The daytime F region dynamo near geomagnetic equator results from the horizontal orientation of equipotential $\mathbf{B}$ lines ($\nu \ll \omega$) enabling electrons to move with electrodynamical force. Therefore electrons move in the direction perpendicular to $\mathbf{B}$ given in Kelley (2009) as follows,

$$(\mathbf{V'}_i)_\perp = \left(1/B^2\right) \left[\mathbf{E'} - \left(\frac{k_B T_i}{q_i}\right) \frac{\bigtriangledown n}{n} + \left(\frac{M}{q_i}\right) g \right] \times \mathbf{B} \tag{2.4}$$

where $(\mathbf{V'}_i)_\perp$ is the plasma drift velocity; the second and third terms refer to pressure and gravity forces. In most altitudes, the electric field $\mathbf{E'}$ contribution (first term) is identical for electrons and ions since it is independent on the electric charge. Moreover, $\mathbf{E'}$ dominates over plasma pressure and gravity forces (e.g., Kelley, 2009). Therefore $(\mathbf{V'}_i)_\perp$ is mainly governed by ambient electric field $\mathbf{E}$ perpendicular to the $\mathbf{B}$, thus it is commonly referred to as $\mathbf{E} \times \mathbf{B}$ drift. In the F region, the zonal $\mathbf{E}$ causes the plasma to drift upward during the day and downward during the night in the low latitudes, while the vertical electric field $\mathbf{E}$ causes zonal drifts which are westward during the daytime and eastward during the night (Fejer et al., 1991). Vertical $\mathbf{E} \times \mathbf{B}$ drift results in fountain effect, lifting plasma upwards where it eventually diffuses along geomagnetic field lines forming crests at latitudes about $15° - 18°$ from the equator (Sastri, 1990; Anderson, 1981).

While vertical $\mathbf{E} \times \mathbf{B}$ drift and EEJ are permanent features of low/equatorial latitude ionosphere, changes in geomagnetic activity may significantly influence the variations of the electric fields (e.g., Blanc and Richmond, 1980; Fejer et al., 1979; Retterer and Kelley, 2010). Modification of low/equatorial latitude electric fields during storm conditions is mainly due to ionospheric disturbed dynamo (Blanc and Richmond, 1980) and prompt penetrating electric fields of magnetospheric origin (Fejer et al., 1979; Fejer, 1997). Usually, prompt penetrating electric fields lead to eastward (westward) electric fields and therefore enhances (decreases) vertical $\mathbf{E} \times \mathbf{B}$ drift during local daytime (nighttime) in low latitude ionosphere (Fejer, 1997). Figure 2.6 shows a comparison
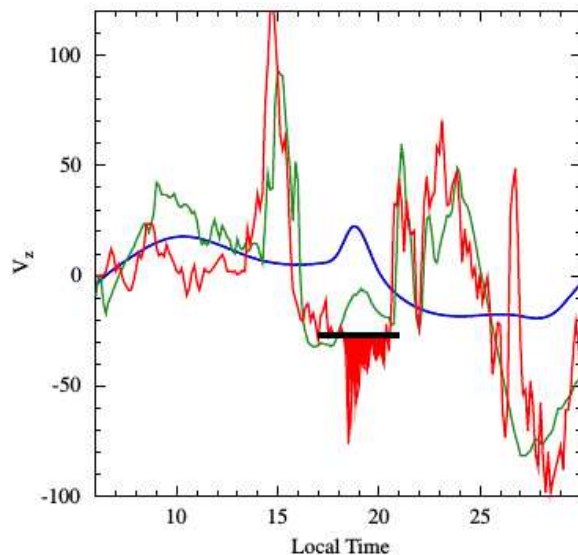
Figure 2.6: Vertical $\mathbf{E} \times \mathbf{B}$ drift observations (red) at Jicamarca during geomagnetic storm, 09 November 2004. Quiet time Scherliess-Fejer model (blue) and the quiet time plus Kelley model for the penetration field (green) are shown (Retterer and Kelley, 2010).

of vertical $\mathbf{E} \times \mathbf{B}$ drift (red curve) over Jicamarca with quiet time Scherliess-Fejer model (blue curve) (Scherliess and Fejer, 1999) and the quiet time model plus the Kelley model for penetrating electric fields (green curve) during the disturbed period of 09 November 2004 (Retterer and Kelley, 2010). Retterer and Kelley (2010) reported enhanced penetration of westward daytime electric field leading to counter electrojet conditions during the abrupt turning of IMF Bz into the northward direction that may have suppressed the normal evening pre-reversal enhancement. The horizontal black bar in Figure 2.6 shows downward pre-reversal enhancement occurring at the time of usual PRE (Retterer and Kelley, 2010).

Due to thermosphere-ionosphere coupling, $\mathbf{E}$ and therefore vertical ionospheric drifts can be easily perturbed by lower atmospheric gravity waves and planetary waves, even during magnetically quiet periods and by magnetospheric processes emanating from high-latitude ionosphere during magnetically disturbed periods (e.g., Rishbeth and Garriott, 1969; Rishbeth, 1971; Forbes, 1995; Richmond, 1995b,c; Muller-Wodarg, 1997; Millward et al., 2001; Kelley et al., 2003). Tides of different wavelengths rise from lower and middle atmosphere and affect the wind structure and temperatures of the lower atmosphere. In the E region of equatorial ionosphere, the largest amplitude diurnal modes are the west wave number one migrating tide (W1) and the diurnal eastward propagating tide with zonal wave number 3 (DE3) (e.g., Fesen et al., 2002; England et al., 2006).

17

Radiative heating of the troposphere mainly govern the formation of W1, while additional contributions come from radiative heating in the stratosphere, mesosphere and lower thermosphere (Forbes, 1982). DE3 primarily affects longitudinal wind structure and temperatures in the lower atmosphere, thus some longitudinal dependence on the modulation of equatorial dynamo can be attributed to it (England et al., 2006). The formation of DE3 is mainly governed by latent heat release in the troposphere (Hagan and Forbes, 2002).

Figure 2.7 shows the vertical $\mathbf{E} \times \mathbf{B}$ drift (ion drift) over different longitudinal sectors estimated by SF (Scherliess and Fejer, 1999) and coupled ionosphere-thermosphere-plasmasphere (CTIP) (Millward et al., 1996) models. CTIP model allows contribution of tidal forcing in vertical ion drift (Millward et al., 2001). In the simulation study by Millward et al. (2001) only migrating tides of different modes were considered. Their finding showed that the semi-diurnal tides dominate the daytime equatorial electrodynamics (vertical $\mathbf{E} \times \mathbf{B}$ drift) for both solar minimum and maximum conditions, while diurnal tides contribute very little. Similar work by Fesen et al. (2002) which was based on TIME-GCM simulation produced almost the same results which also agree with observations.

Figure 2.8 shows the seasonal and longitudinal variability of vertical $\mathbf{E} \times \mathbf{B}$ drift measured by the IVM instrument on-board the C/NOFS satellite for the period within 2009–2013 (Yizengaw et al., 2014a). The C/NOFS $\mathbf{E} \times \mathbf{B}$ drift observations were taken within $\pm 8°$ of geomagnetic equator around different longitudes (shown at the top axis of Figure 2.8) and below 500 km in altitudes. The C/NOFS $\mathbf{E} \times \mathbf{B}$ drift velocities for the period studied were time averaged for each longitudinal sector. The results shows that the vertical $\mathbf{E} \times \mathbf{B}$ drift velocities are generally stronger in the American sector compared to the African sector during almost all local times. The longitudinal dependence of C/NOFS $\mathbf{E} \times \mathbf{B}$ can be attributed to non-migrating tides and difference in geomagnetic field (e.g., Immel et al., 2006b; Yizengaw et al., 2014a).

2.5 Summary

Vertical $\mathbf{E} \times \mathbf{B}$ drift results from complex interaction between the E and F region process which changes with seasons, solar cycle, local time, geomagnetic activity and longitude (e.g., Fejer et al., 1979; Fejer, 1997; Forbes, 1995; Kelley et al., 2003; Kelley, 2009). Different tidal components resulting from upward propagating tides and their non-linear interactions, generally govern and
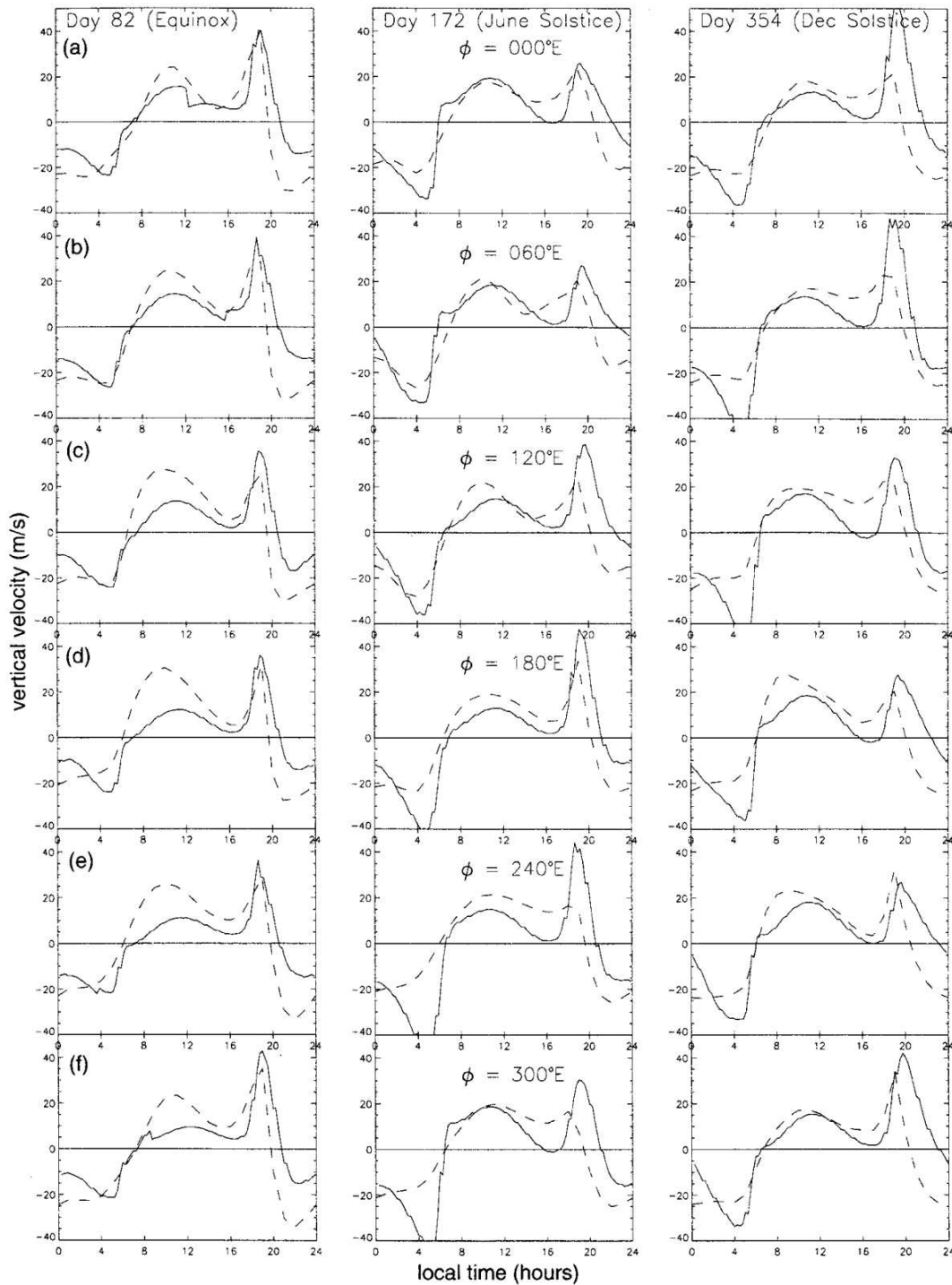
Figure 2.7: Diurnal variation of vertical $\mathbf{E} \times \mathbf{B}$ drift from CTIP (solid curve) and SF (dashed curve) models for solar maximum conditions ($F10.7 = 180$) and with a solitary (2, 2) tidal components (semi-diurnal tide). Rows show longitudinal variation of vertical $\mathbf{E} \times \mathbf{B}$ drift, while columns describe the corresponding seasonal variations based on results from both models (Millward et al., 2001).
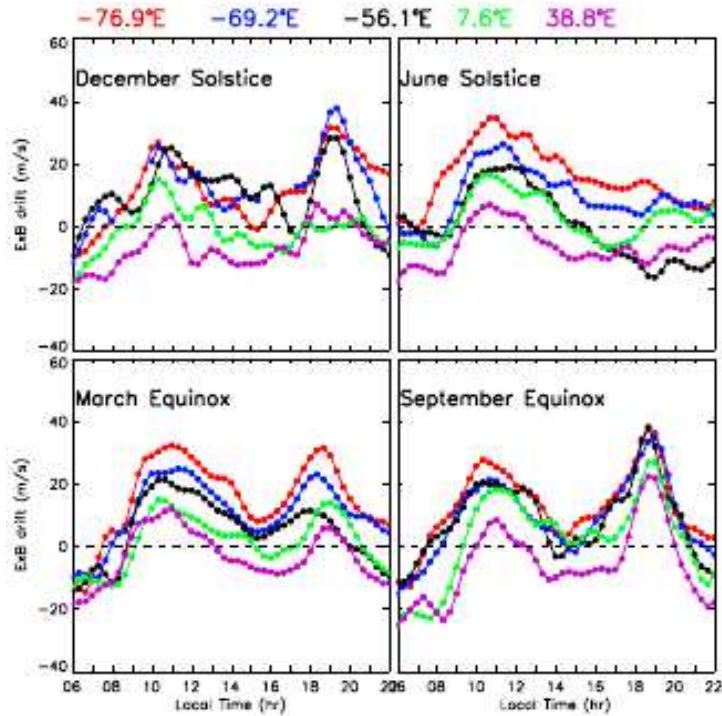
Figure 2.8: Diurnal, seasonal, and longitudinal variation of vertical $\mathbf{E} \times \mathbf{B}$ from ion velocity meter (IVM) on-board C/NOFS satellite for the period 2009–2013. Colors of the curves are associated with different geographic longitudes (sectors) shown on the axis above (Yizengaw et al., 2014a).

modulate the neutral winds at different altitudes (within E and F regions). Migrating tides move westward with the apparent motion of the Sun, while the non-migrating tides move at different speed with the apparent motion of the Sun. Diurnal and semi-diurnal migrating tides have dominant effects in upward $\mathbf{E} \times \mathbf{B}$ drift (Maute et al., 2012). Diurnal eastward propagating tide with zonal wave number 3 (DE3) are dominant non-migrating tides (Hagan et al., 2007). Non-migrating tides results in regular wave-4 pattern in the upward $\mathbf{E} \times \mathbf{B}$ drift during daytime (Lin et al., 2007; Kil et al., 2007). Wave-4 pattern is a wavelike characteristics observed in the longitudinal structure of the ionosphere (Sagawa et al., 2005). However, Maute et al. (2012) showed that longitudinal variation of upward $\mathbf{E} \times \mathbf{B}$ drift are mostly due to the strength of geomagnetic main field which changes with longitudes. Their finding confirms large $\mathbf{E} \times \mathbf{B}$ drift reported over South American sector in comparison with the weak vertical ionospheric drift over the African sector (Yizengaw et al., 2014a). The migrating and non-migrating tides modulates the E and F region dynamos and they change with seasons, solar cycle and local time (e.g., Crain et al., 1993; Lühr et al., 2012; Maute et al., 2012). The simulation results from Millward et al. (2001) were used to demonstrate

the influence of semi-diurnal migrating tides in longitudinal and seasonal variations of vertical $\mathbf{E} \times \mathbf{B}$ drift. Their results showed mostly larger amplitudes (in comparison with the vertical ionospheric drifts from SF model) and they were sometimes slightly shifted in local time distribution, confirming the importance of migrating semi-diurnal tides in the equatorial electrodynamics. During storm conditions, changes of low/equatorial latitude electric fields and hence vertical $\mathbf{E} \times \mathbf{B}$ drifts are mainly due to disturbed Ionospheric dynamo and penetration electric fields of magnetospheric origin (e.g., Blanc and Richmond, 1980; Fejer, 1997).

Comparison of 1-year geomagnetic field data recorded in 2009 (mean annual sunpot number $R_z = 3.1$) over South American, Philippine and African sector have recently been used to investigate longitudinal variation of EEJ and CEJ during quiet conditions ($A_p \leq 3$) (Rabiu et al., 2017). Their results revealed larger occurence of CEJ over the African sector; AAE and Ilorin are dominated by morning and evening CEJ, respectively. Previously, (e.g., Yizengaw et al., 2011b) showed in a case study a prominent occurence of CEJ in the African sector than in the American sector. CEJ occurence during morning and afternoon hours over the western Africa longitudinal sectors was reported as seasonal effect (Doumouya et al., 1998).

Using ground-based magnetometer and $\mathbf{E} \times \mathbf{B}$ drift (JULIA) data over the African and American sectors, Habarulema et al. (2016) discovered and confirmed that poleward travelling ionospheric disturbances (TIDs) which are of geomagnetic equator origin may be due to changes in ionospheric electrodynamics.

Oyekola and Kolawole (2010) estimated vertical $\mathbf{E} \times \mathbf{B}$ drift from the hourly hmF2 values acquired from ionogram data over a near dip equatorial station Ouagadougou (12.4°N, 358.5°E, dip angle 5.9°N) in Africa. When comparing the ionosonde derived $\mathbf{E} \times \mathbf{B}$ drift with $\mathbf{E} \times \mathbf{B}$ drift from IRI, larger values (than those of IRI) were observed during daytime and smaller values at nighttime.

Chapter 3

Measurements and Modelling techniques

3.1 Introduction

In this chapter, C/NOFS satellite and magnetometer observations are described. Previous studies related to vertical $\mathbf{E} \times \mathbf{B}$ drift over the African and other longitudinal sectors are briefly presented. Different modelling techniques used in the estimation of ionospheric vertical drift are also presented.

3.2 Measurements

Since the E region ionosphere is present only during daytime, dynamo action is effective during daytime and results in eastward electric field $\mathbf{E}$ which can be transferred into F region via equipotential magnetic field $\mathbf{B}$ near magnetic equator (Heelis et al., 1974). Figure 3.1 shows components of Earth's geomagnetic fields in geographic coordinate system. The horizontal component of geomagnetic field, $\mathbf{H} = \sqrt{\mathbf{X}^2 + \mathbf{Y}^2}$ was used in this work as measurements from the pair of low latitude magnetometers, where $\mathbf{X}$ and $\mathbf{Y}$ are northward and eastward components of $\mathbf{B}$. For small declination angle, $\mathbf{D} = arctan(\mathbf{Y}/\mathbf{X})$, $\mathbf{X}$ is approximately equal to $\mathbf{H}$, since $\mathbf{X} = \mathbf{H}cos\mathbf{D} \approx \mathbf{H}$. Due to the orthogonal orientation of eastward $\mathbf{E}$ with nearly horizontal $\mathbf{B}$ at the magnetic equator, collective effort of $\mathbf{E}$ and $\mathbf{B}$ (Lorentz force) known as vertical $\mathbf{E} \times \mathbf{B}$ drift moves ions and electrons in the E and F regions. Ionospheric vertical drifts primarily drive low latitude electrodynamic processes such as fountain effect, changes in equatorial electrojet (EEJ), plasma irregularities and ionospheric density structures (e.g., Anderson, 1973; Fejer, 1997).

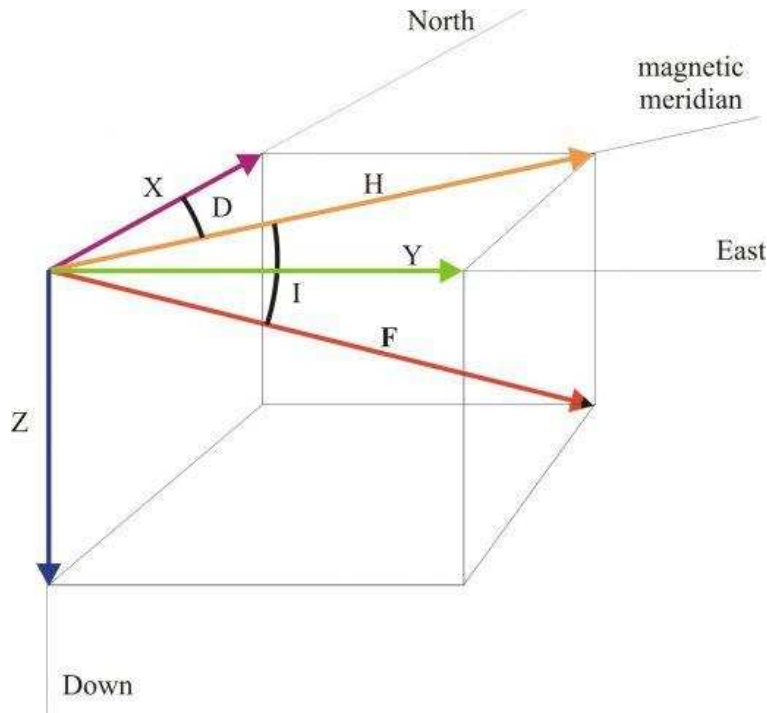As described earlier, EEJ is a strip of enhanced current flowing within $\pm 3°$ of dip equator which

Figure 3.1: Schematic which shows components of Earth's magnetic field in geographic coordinate system. **D**=magnetic declination and **I** is magnetic inclination which is positive downward. **F** is the total intensity of magnetic fields. Source: http://roma2.rm.ingv.it/en/research_areas/1/earth-s_magnetic_field/8/.

causes large enhancement in the horizontal component of geomagnetic field (H) near the equator (Richmond, 1973; Forbes, 1981; Rabiu et al., 2013). Figure 3.2 shows variation of simulated horizontal component of Earth's magnetic field during daytime near dip equator, Jicamarca (11.8°S, 77.2°W; 0.8°N geomagnetic) and another off the magnetic equator, Piura (5.18°S, 80.64°W; 6.8°N geomagnetic) over the South American sector (Fang et al., 2008). The horizontal fields ($\triangle H$) from stations near dip equator and $\approx 6 - 9°$ away, represents variation of EEJ current and therefore $\mathbf{E} \times \mathbf{B}$ drift during local daytime (Fang et al., 2008). Due to the importance of vertical $\mathbf{E} \times \mathbf{B}$ drift, the effort of measuring it started decades ago in Jicamarca (Woodman and Hagfors, 1969). Incoherent scatter radar (ISR) was the primary instrument to measure vertical $\mathbf{E} \times \mathbf{B}$ drift in the F region. ISR determines the direction of $\mathbf{B}$ and can measure plasma velocities perpendicular to the magnetic field. Doppler effect radar which provides vertical $\mathbf{E} \times \mathbf{B}$ drift at about 150 km (around E region) are now taking over ISR because of their low operation cost (e.g., Kudeki and Fawcett, 1993; Chau, 1998; Alken, 2009; Patra et al., 2014). However, they provide observations during daytime since they are applicable when the E region is present (E-region is negligible during night-
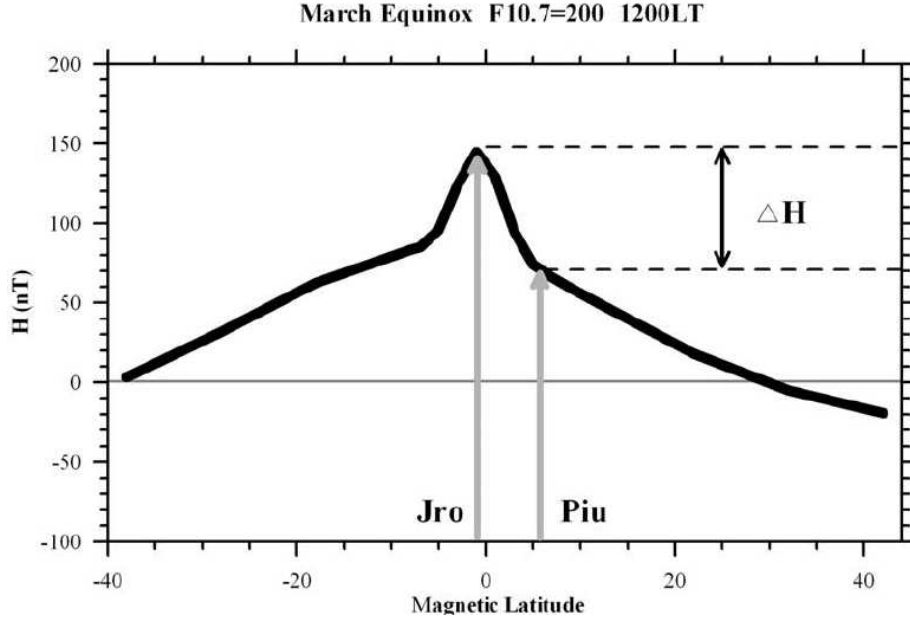
Figure 3.2: Latitudinal H field variations and the corresponding magnetic perturbation $\triangle H$. The white arrows point to the location of magnetometer stations at dip equator (Jicamarca, Jro) and outside EEJ footprint (Piura, Piu) (Fang et al., 2008).

time). Satellite-based sensors such as Atmospheric Explorer E (AE-E), Republic of China Satellite 1 (ROCSAT-1) and Communication/Navigation Outage Forecasting System (C/NOFS) have been providing equivalent measurements at higher altitudes and enable studies of longitudinal variation of ionospheric vertical drifts. However satellite data have poor local time coverage, thus cannot provide conclusive ionospheric variability over a single location. In the absence of instruments providing ionospheric vertical drifts over the African sector, studies of vertical $\mathbf{E} \times \mathbf{B}$ drift and therefore EEJ have been ongoing with the help of mainly ionosondes (e.g., Bilitza et al., 2004; Oyekola and Oluwafemi, 2007; Adebesin et al., 2013) and magnetometers (e.g., Doumouya et al., 1998, 2003; Haile, 2003; Rabiu et al., 2011). However, ionosonde vertical $\mathbf{E} \times \mathbf{B}$ drift measurements during daytime are often underestimated from actual values since photo-chemistry governs the reflection height of the F layer (e.g., Bertoni et al., 2006; Joshi and Sripathi, 2016). Since the deployment of pairs of low latitude and equatorial magnetometer stations over the African sector, differential magnetometers approach has been a preferred method in the estimation of vertical $\mathbf{E} \times \mathbf{B}$ drift (e.g., Yizengaw et al., 2012). However this approach only provides $\mathbf{E} \times \mathbf{B}$ drift during daytime since it is based on EEJ current. Despite the importance of $\mathbf{E} \times \mathbf{B}$ drift, there is still a lack of instruments and local models providing ionospheric vertical drifts over the African sector.

Hence, the motivation to estimate the vertical ionospheric drifts on long term over this longitude sector based on magnetometer data, with the aim of developing models based on African data. Global empirical models of plasma drift have been developed and mainly use Jicamarca $\mathbf{E} \times \mathbf{B}$ drift observations from ISR and satellite-based sensors on-board the Atmospheric Explorer E (AE-E), Republic of China Satellite 1 (ROCSAT-1) (e.g., Scherliess and Fejer, 1999; Fejer et al., 2008). There have been other regional $\mathbf{E} \times \mathbf{B}$ drift models developed (e.g., Abdu et al., 1995; Batista et al., 1996; Sastri, 1996; Alken, 2009). The Scherliess-Fejer (SF) model (Scherliess and Fejer, 1997, 1999) has been incorporated in other global empirical models such as SAMI2 (SAMI2 is Another Model of the Ionosphere) (e.g., Huba et al., 2000) and International Reference Ionosphere (IRI) (Bilitza and Reinisch, 2008). The global models have longitudinal coverage and thus can estimate $\mathbf{E} \times \mathbf{B}$ drift along any equatorial regions. Regional models such as the one that was developed in Brazil (Batista et al., 1996) cannot work well in other longitude sectors because of tidal effect and local times. Alken (2009) developed vertical $\mathbf{E} \times \mathbf{B}$ drift model using JULIA observation and although this model was validated against global model by Scherliess and Fejer (1999), it can only work well in South American longitude sector.

However global models are climatological in nature and are mainly based on observations over the South American sector and therefore may not be accurate over the African sector. In this work, an effort is made to develop empirical model to estimate vertical $\mathbf{E} \times \mathbf{B}$ drift over the African sector based on ground magnetometer and C/NOFS measurements/observations. Figure 3.3 shows geographic location of instruments (magnetometers) and an examples of a possible orbit followed by the C/NOFS satellite over the region of study. Magnetometer stations used are Addis Ababa, AAE 9.0°N, 38.8°E, 0.18°N geomagnetic and Adigrat, ETHI (14.3°N, 39.5°E, 6.0°N geomagnetic). Details related to magnetometer and satellite data processing are described in the following sections.

3.2.1 Magnetometer observations

A pair of magnetometers one near dip equator (EEJ region) and another 6°–9° away, can be used in the estimation of equatorial electrojet (EEJ) current during daytime and thus $\mathbf{E} \times \mathbf{B}$ drift (e.g., Rastogi and Klobuchar, 1990; Anderson et al., 2004). Equatorial and low latitude magnetometers measure the same currents from different sources such as magnetopause, ring currents, main field, solar quiet S_q, and field aligned current (FAC), but in addition EEJ currents are also observed by
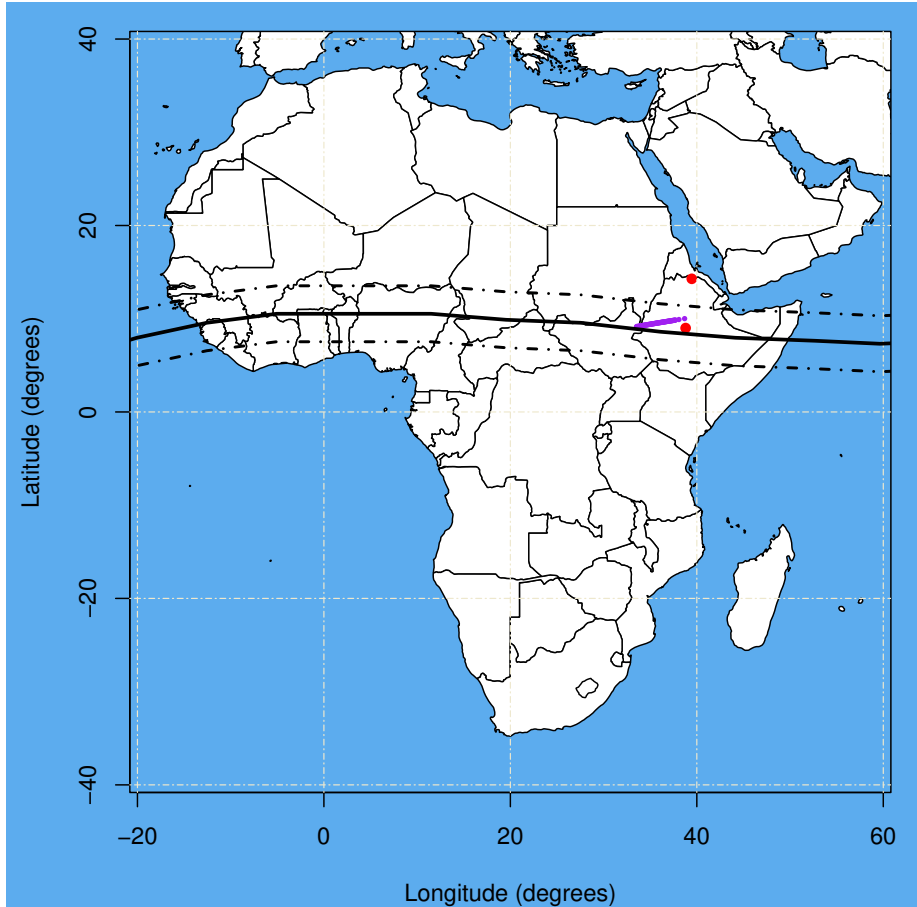
Figure 3.3: Map demonstrating geographic location of the ground-based magnetometers (red dots) used for this study and possible regions near Addis Ababa, AAE (9.0°N, 38.8°E, 0.18°N geomagnetic) where C/NOFS satellite passes (orbit number = 20515 shown in connected magenta solid dots). The nearly horizontal solid line (black) depicts the geomagnetic equator, and the two dashed lines (black) indicate the EEJ region.

equatorial station. The main field originates from convection of the Earth's core and the changes associated with this field during magnetically quiet days is known as solar quiet S_q variation (Chapman and Bartels, 1940). While FAC are typically a high-latitude phenomenon, the electric field and currents from the dynamos in the magnetosphere flow down to the equatorial ionosphere via the polar ionosphere. Since FAC are mainly divided into region 1 (R1 FAC) and region 2 (R2 FAC) currents, R1 FAC connects the currents in the ionosphere to currents in the magnetopause and the magnetotail, while R2 FAC connects to the partial ring current in the inner magnetosphere (e.g., Iijima and Potemra, 1978; Cowley, 2000; Clausen et al., 2013; Coxon et al., 2014). Depending on the direction of IMF Bz, R2 FAC can reduce penetrating magnetospheric origin

electric field and therefore causing westward equatorial electric during daytime (such electric fields are possible source of CEJ (e.g., Daglis et al., 1999; Kikuchi et al., 2000; Yizengaw et al., 2011*a*). Because of the additional EEJ contribution into the equatorial magnetometer observations, differencing the respective H-components from locations at the equator and outside the EEJ footprint (6–9 degrees away from the equator) provides the EEJ current (Rastogi and Klobuchar, 1990) which is linearly related to the vertical $\mathbf{E} \times \mathbf{B}$ drift during local daytime (e.g., Anderson et al., 2002, 2004; Yizengaw et al., 2012). Since the geomagnetic field $\mathbf{B}$ at the magnetic equator are orientated approximately horizontally, variation of EEJ is represented by horizontal components of geomagnetic field near dip equator ($\triangle H$). In this work, horizontal components of geomagnetic field (H) measurements for the magnetometer stations Addis Ababa, AAE (9.0°N, 38.8°E, 0.18°N geomagnetic) and Adigrat, ETHI (14.3°N, 39.5°E, 6.0°N geomagnetic) were corrected each day for different offset values associated with magnetometers at different locations before computation of daytime $\triangle H$ variations. Nighttime ionospheric currents are weak to be clearly detected by ground magnetometers. Hence the average of the hourly H field measurements was computed for each day during 23:00-03:00 LT as a baseline value (Yizengaw et al., 2012).

Figures 3.4 (a)-(d) and (e)-(h) show variations and processing of H fields during quiet (2008-11-19) and disturbed (2012-01-25) conditions leading to the computation of $\triangle H$ variations. Subtraction of baseline values (shown as dashed lines) from geomagnetic field measurements of a corresponding day yields daytime H field variations ($dH_\circ$). In Figure 3.4 (a)-(d) and (e)-(h), variations at ETHI and AAE are plotted in green and red colors respectively. However, the effect of ring current, main field, magnetopause, FAC and solar quiet (S_q) are still involved in the variations of $dH_\circ$. Thereafter differencing of these measurements from two stations was done on a corresponding day and local time to yield $\triangle H$ variations which reflects only changes in EEJ current (e.g., Rastogi and Klobuchar, 1990; Anderson et al., 2002). The final computed $\triangle H$ variations representing EEJ changes are shown in Figure 3.4 (d) and (h) for quiet (2008-11-19) and disturbed (2012-01-25) days respectively.

Figure 3.5 shows the daytime $\triangle H$ data at one minute time intervals obtained by considering available data from AAE and ETHI during 2008–2013. Although part of $\triangle H$ data is missing, the magnitudes of daytime $\triangle H$ for different months are also oscillating at different periods. Equatorial and low latitude geomagnetic fields have been reported to change at different periods, such as pole tide signal of 14-months (e.g., Rao and Rangarajan, 1978) and Quasi-biennial Oscillation (QBO)
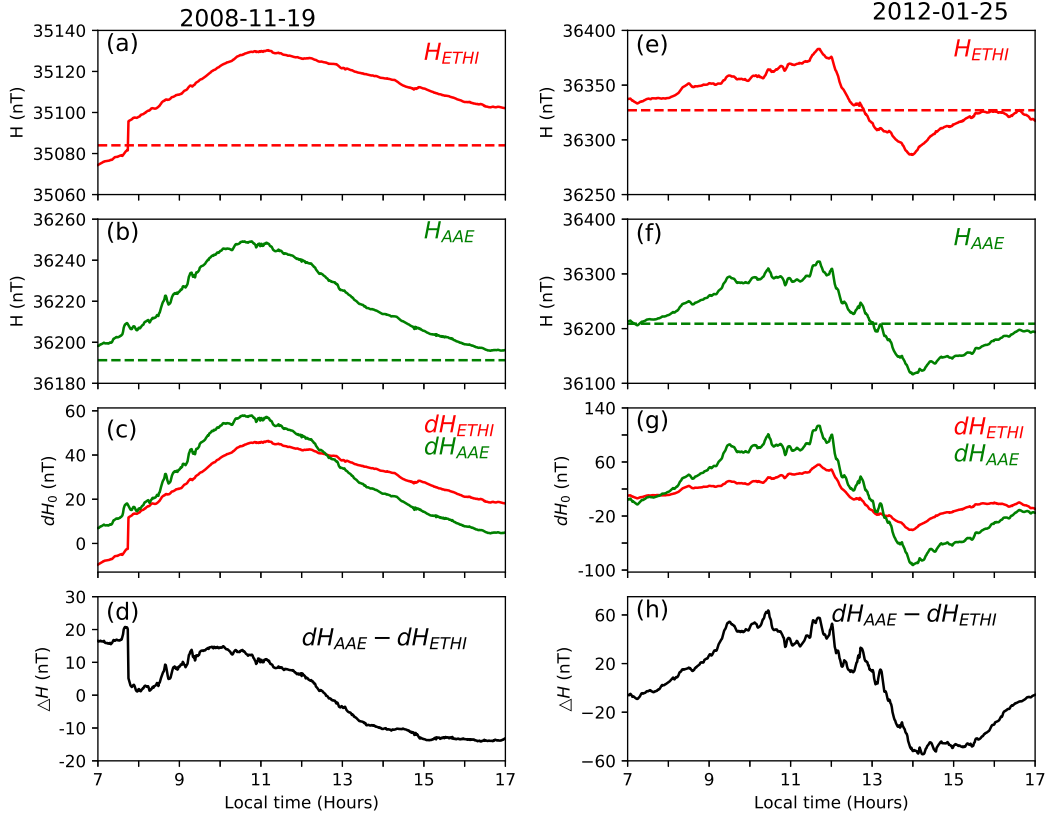
Figure 3.4: (a)-(b) Comparison of H field variations from AAE (green curve) and ETHI (red curve) relative to their baseline values (green and red dashed horizontal lines) during quiet day of 2008-11-19. (c)-(d) Corresponding daytime variation of H fields ($dH_\circ$) and subsequently computation of $\triangle H$ (black curve), and (e)-(h) similarly derivation of $\triangle H$ during the storm day of 2012-01-25.

(e.g., Sugiura, 1976; Rangarajan, 1985). QBO has been reported prominent near geomagnetic equator due to enhanced Cowling conductivity (e.g., Kane, 1996). It results from strong signals of period $\sim$ 2-years especially in meteorological and geomagnetic parameters (e.g., Bhardwaj, 2009) and can contribute to the observed $\triangle H$ oscillations. Long-term variation of $\triangle H$ data is worth being investigated to confirm the nature of such oscillations. Previous studies have shown that $\mathbf{E} \times \mathbf{B}$ inferred from the equatorial and low latitude pair of magnetometers compare well with those of Jicamarca's ISR, Jicamarca Unattended Long-term studies of the Ionosphere and Atmosphere (JULIA) in Peru (e.g., Anderson et al., 2002, 2004), and ion velocity meter (IVM) instrument on-board C/NOFS satellite over the African sector (e.g, Yizengaw et al., 2012). Magnetometer inferred vertical $\mathbf{E} \times \mathbf{B}$ observations from different longitude sectors (Peruvian, Philippine, and Indian) were found to agree well with Scherliess-Fejer model (e.g. Anderson et al., 2006; Anghel et al., 2007) on
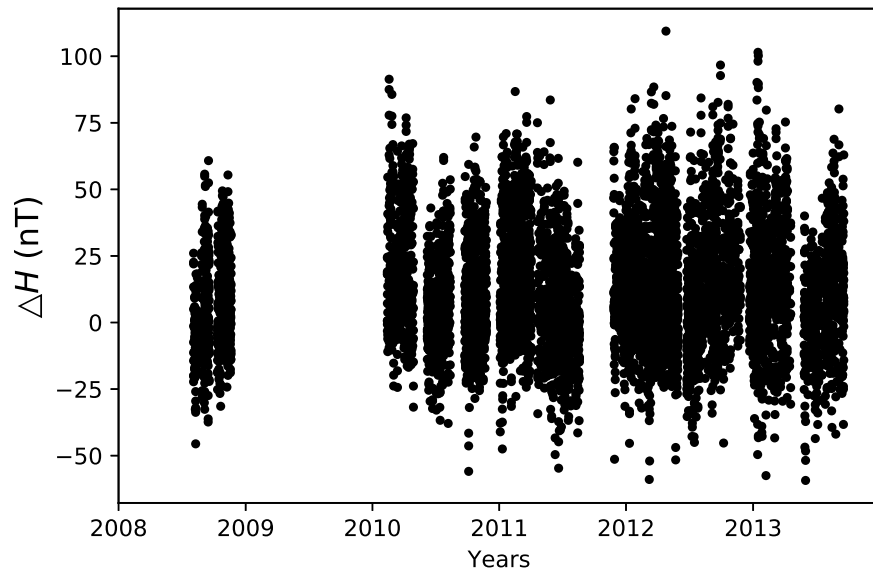
Figure 3.5: Distribution of daytime one-minute $\triangle H$ measurements for the period 2008-2013 over AAE.

a climatological basis.

3.2.2 C/NOFS observations

The C/NOFS satellite was launched into a low Earth orbit at 13° inclination in April 2008. It had an orbital period of 97.3 minutes, with its perigee and apogee are at about 405 km and 850 km, respectively. The main purpose of C/NOFS was monitoring and forecasting ionospheric irregularities which strongly affect communications and navigation systems (de La Beaujardière et al., 2004; de La Beaujardiere et al., 2009). It consisted of six instruments (VEFI-Vector Electric Field Instrument, CERTO-Coherent Electromagnetic Radio Tomography, CORISS-C/NOFS Occultation Receiver for Ionospheric Sensing and Specification, CINDI-Coupled Ion-Neutral Dynamics Investigation which consists of sensors (IVM-Ion Velocity Meter and NWM-Neutral Wind Meter), PLP-Planar Langmuir Probe), for measuring electric fields $\mathbf{E}$, plasma characteristics, the strength of scintillation, ion drifts and neutral winds (de La Beaujardière et al., 2004; de La Beaujardiere et al., 2009). In this work, IVM sensor is used as a source of $\mathbf{E} \times \mathbf{B}$ observations. Based on International Geomagnetic Reference Field (IGRF) model, the measured ion drift is resolved into components parallel and perpendicular to field $\mathbf{B}$. Both components of the ion drift are then resolved into components with respect to magnetic meridian plane. The perpendicular component of ion drift in the magnetic meridian plane (meridional) is used as vertical $\mathbf{E} \times \mathbf{B}$ in this work (Stoneback et al., 2011). Since the accuracy of IVM depends on the O^+ concentration, the vertical $\mathbf{E} \times \mathbf{B}$ drift observations were taken when the altitudes of satellite were within $\sim$ 400-550 km (e.g., Stoneback et al., 2011; Patra et al., 2014). While it is desirable to use C/NOFS $\mathbf{E} \times \mathbf{B}$ observations at reasonable low altitudes for comparison with other $\mathbf{E} \times \mathbf{B}$ observations from other sources such as 150 km echo radar and ISR, the satellite's lowest altitude is about $\sim$ 400 km. Vertical $\mathbf{E} \times \mathbf{B}$ observations are taken as the satellite passes over AAE within $0.18°N \pm 4°$ geomagnetic latitude and $38.8°E \pm 11.2°$ geographic longitude at an altitude range within $\sim$ 400-550 km (e.g., Stoneback et al., 2011). The selection of the spatial extent between satellite and ground-magnetometer based on their longitudinal and latitudinal separation will be discuss later. Large C/NOFS vertical $\mathbf{E} \times \mathbf{B}$ drifts ($\approx$200 m/s) which follow large plasma depletion were reported at dawn during quiet condition (low solar activity period) in the America–Africa and India–Indonesia longitude sectors by (e.g., de La Beaujardiere et al., 2009). However, 15-minute average annual vertical ionospheric drift velocities over AAE for the period 2009–2013 were within $\approx$ -25–25 m/s during daytime (Yizengaw et al., 2014b). Quiet time C/NOFS $\mathbf{E} \times \mathbf{B}$ observations in the range -50 m/s–50 m/s were seen at longitude sectors 0°–60°E during spring in 2010 (Stoneback et al., 2011). Therefore, in-situ C/NOFS ion drift observations in

our work were within ± 60 m/s considering possible geomagnetic disturbances. These observations were further corrected for any potential outliers using median filtering procedure for each satellite pass. Rodrigues et al. (2011) compared the C/NOFS vertical $\mathbf{E} \times \mathbf{B}$ drift with ISR $\mathbf{E} \times \mathbf{B}$ drift observations and climatological model during 25–30 January 2009 (Scherliess and Fejer, 1999). They corrected C/NOFS observations using 15-point median filtering for each satellite pass. In this work, a technique based on medians together with median absolute deviation (MAD) is used. After correcting for outliers $\sim 5\%$ of the observations were removed. The calculated mean (-10.05 m/s) and median (-10.06 m/s) from the overall C/NOFS $\mathbf{E} \times \mathbf{B}$ observations are nearly equal, and therefore suggesting low volume of outliers within dataset (Smith et al., 2015). Median is normally stable to outliers than mean, it has a breakpoint of 50% (Huber, 1981). That is to say, the median filtering can start to fail for observations consisting of about 50% of outliers. Similarly, the MAD has 50% breakpoint and thus it can be used together with medians in removing outliers in C/NOFS $\mathbf{E} \times \mathbf{B}$ drift observations. As the name suggests, MAD is the median of the absolute deviation of observations from a particular median value (Huber, 1981),

$$MAD = b \cdot M_i(\|X_i - M_j(X_j)\|), \tag{3.1}$$

where M_i and M_j are median values for i-th absolute deviation and j-th observations and b is the numeric value describing the distribution of data. As a rule of thumb, datasets with Kurtosis and Skew distribution less than ± 1 enable making an assumption of normal distribution valid, hence the upper and lower limit for a median filter can be written as follows,

$$X_{upper} > M + MAD \text{ and } X_{lower} < M - MAD \tag{3.2}$$

where M is the median value of C/NOFS $\mathbf{E} \times \mathbf{B}$ drift per satellite pass and $b = 1/Q(0.75) = 1.4826$ for normal distributed observations (Huber, 1981) was used in the computation of MAD (small Skewness, ≈ 0.1 and Kurtosis, ≈ 0.5). $1/Q(0.75)$ refers to a 0.75 percentile of underlying distribution.

Only one MAD was used (equation (3.2)) in order to suppress large fraction of potential outliers with the intention of possibly increasing the correlation between the $\triangle H$ and $\mathbf{E} \times \mathbf{B}$ drift observations as it will be shown later.

Figure 3.6 (a)–(d) shows the $\mathbf{E} \times \mathbf{B}$ drift observations during quiet and storm periods 2008/11/19 and 2012/01/25 used for illustration. These days were extracted from large dataset during the period 2008–2013 as they have reasonable amount of observations and again for comparison with
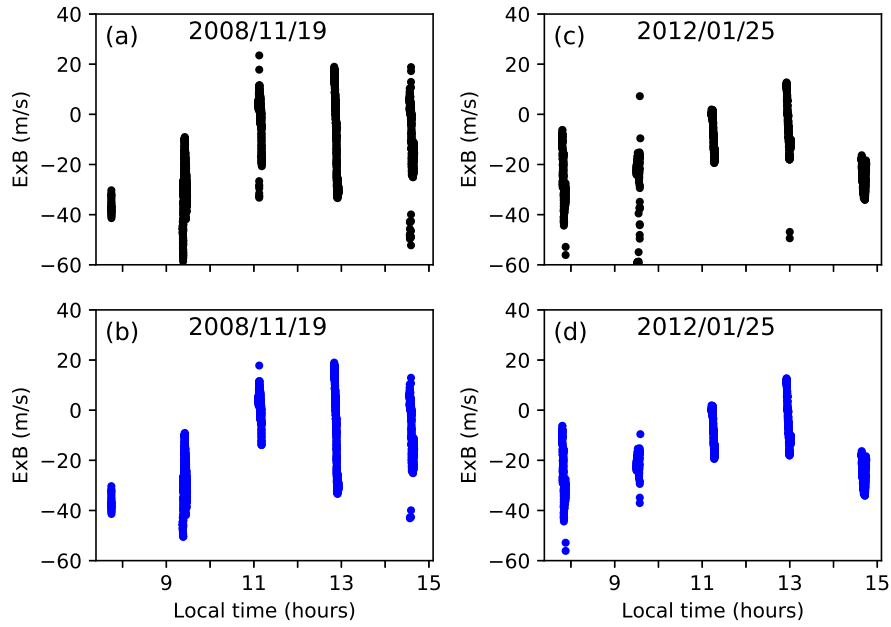
Figure 3.6: C/NOFS vertical $\mathbf{E} \times \mathbf{B}$ drift before and after removing outliers using median and MAD filtering technique ((a) and (b)) during the quiet day of 2008-11-19. Panels (c)-(d) show C/NOFS vertical $\mathbf{E} \times \mathbf{B}$ drift before and after correction for outliers on a disturbed day of 2012-01-25.

$\triangle H$ measurements in Figure 3.4. Through visual inspection of $\mathbf{E} \times \mathbf{B}$ drift observations in Figure
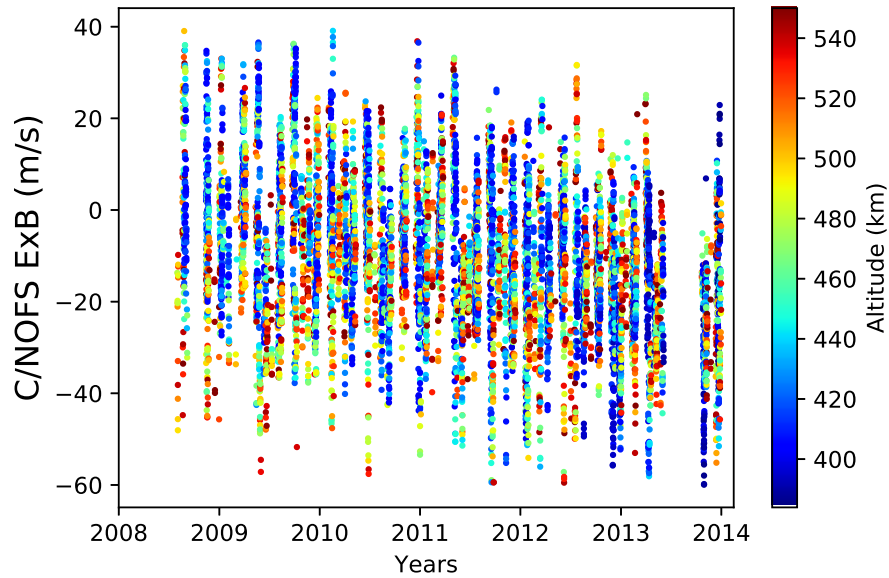
Figure 3.7: Vertical $\mathbf{E} \times \mathbf{B}$ drift observations from IVM sensor on-board the C/NOFS satellite at one-minute interval for the period 2008–2013 after correction for outliers.

3.6, it can be evident that few data-points were removed as outliers for both quiet and disturbed

periods. Figure 3.7 shows the resulting $\mathbf{E} \times \mathbf{B}$ drift observations for period 2008–2013 after limiting the magnitudes of vertical ionospheric drifts and removal of possible outliers. Since C/NOFS $\mathbf{E} \times \mathbf{B}$ drift measurements are provided at 0.5 seconds resolution, large observations can be seen per satellite pass. In this way, relatively large $\mathbf{E} \times \mathbf{B}$ drift values centered nearly close to a minute were averaged alongside their corresponding altitudes. Hence, $\mathbf{E} \times \mathbf{B}$ drift values shown in Figure 3.7 are given in one minute intervals and at different altitudes around AAE. C/NOFS data are available through an open repository (http://cdaweb.gsfc.nasa.gov/).

Patra et al. (2014) compared quiet time C/NOFS $\mathbf{E} \times \mathbf{B}$ drift observations with $\mathbf{E} \times \mathbf{B}$ drift observations from two radars over Kototabang (10.36°S magnetic latitude, Indonesia) and Gadanki (6.5°N magnetic latitude, India) and they found correlation coefficient value of ~ 0.86 (when using 175 points) at both stations. Rodrigues et al. (2011) also compared C/NOFS $\mathbf{E} \times \mathbf{B}$ drift observations over Jicamarca (77.2° ± 40°) longitude with ISR and climatological model during sudden stratospheric warming event in 25–30 January 2009. In their analysis, most radar observations fell within one standard deviation of C/NOFS $\mathbf{E} \times \mathbf{B}$ variability, suggesting a good agreement between two different observations (Rodrigues et al., 2011). They also reported large deviation between C/NOFS $\mathbf{E} \times \mathbf{B}$ drift and respective values from climatological model (Scherliess-Fejer) for a particular day (27 January 2009) where $\mathbf{E} \times \mathbf{B}$ drift values of -20 m/s and ~ 5 m/s were seen for C/NOFS and climatological model at about 1300–1400 LT. Stoneback et al. (2011) compared C/NOFS $\mathbf{E} \times \mathbf{B}$ drift with $\mathbf{E} \times \mathbf{B}$ drift from climatological model and ISR for longer period 2008–2010. They showed that C/NOFS $\mathbf{E} \times \mathbf{B}$ drift observations compare approximately well especially with the ISR observations than climatological model, but also reported some deviations especially during morning, afternoon and nighttime hours.

3.3 Modelling techniques

Three different empirical modelling techniques were used to estimate vertical $\mathbf{E} \times \mathbf{B}$ drift based on $\triangle H$ measurements. These modelling techniques are empirical orthogonal functions (EOFs), neural network (NN) and partial least squares (PLS) whose performances in estimating ionospheric vertical drifts were compared in next chapters. Brief descriptions of these modelling techniques are presented in the next subsections.

3.3.1 Empirical Orthogonal Functions (EOFs)

EOFs have the capability of revealing hidden patterns and reducing the dimensions of a series of images and continuous signals along with their proportion of variance (Lorenz, 1956). In the field of signal processing and mathematical statistics, method of EOF analysis is a decomposition of signal or data based on orthogonal basis functions. Unlike other decomposition techniques such as Fourier and Wavelets analysis which decompose data using pre-defined base functions (e.g., Butzer and Nessel, 1971; Mallat, 1989), the orthogonal basis functions used in EOF analysis are derived purely from variations of dataset (e.g., Lorenz, 1956; Kelly, 1985). Hence, the eigen series defined by these basis functions converge quickly, making it possible to represent most variance of original dataset with fewer EOF components. While EOF decomposition technique is equivalent to the principal components (PCs) analysis, EOF method describes both spatial and temporal patterns (e.g., Lorenz, 1956; Kelly, 1985). The underlying physical meaning of EOF analysis is finding uncorrelated linear combinations of the different variables that explain maximum variance of spatio-temporal field X_m such that,

$$X_m = \sum_{i=1}^{M} u_i(s)c_{im}(t),$$
$$(3.3)$$

where M is the number of orthogonal basis functions (modes), while $u_i(s)$ and $c_{im}(t)$ are associated EOF coefficient and EOF basis function satisfying the relation,

$$\sum_{m}^{M} u_{im}u_{jm} = \delta_{ij} = \begin{cases} 1 & i = j \\ 0 & i \neq j \end{cases}$$
$$(3.4)$$

and

$$\overline{c_i(t)c_j(t)} = \lambda_i \delta_{ij}$$
$$(3.5)$$

where the over-bar in equation (3.5) refers to a time averaged of $c_i(t)$, and λ_i is the variance (eigenvalue) of the i-th eigenvector such that, $\lambda_i \geq \lambda_{i+1} \geq \lambda_{i+2} \geq \ldots\ldots \geq \lambda_M$. Hence, it is possible to write the relation as follows,

$$\overline{c_i^2(t)} = \frac{1}{N} \sum_{m=1}^{M} c_i^2(t_m) = \lambda_i$$
$$(3.6)$$

where N refers to the number of associated EOF coefficients (time series). It can be shown that c_i and u_i always satisfy the constraints defined in equations (3.3), (3.5) and (3.6). Let $\mathbf{E}$ be a matrix with columns being the spatial patterns (u_i) and matrix $\mathbf{A}$ constructed such that rows are time

series (c_i), then the summation over the eigenvector above of the product of time series and spatial patterns shown in equation (3.3) is simply the matrix product:

$$\mathbf{X} = \mathbf{EA} \tag{3.7}$$

The matrix $\mathbf{E}$ needs to satisfy the property,

$$\mathbf{AA}^T = \lambda \mathbf{I} = \mathbf{\Lambda} \tag{3.8}$$

where $\mathbf{I}$ is the identity matrix, while Λ is a matrix where off-diagonal elements are zero and diagonal elements (λ_i) are arranged in descending order (e.g., Hannachi et al., 2007).

The covariance matrix $\mathbf{C}_e$ can be constructed from eigenvectors $c_i(t)$,

$$\mathbf{C}_e = \mathbf{XX}^T = \begin{pmatrix} c_{11} & c_{12} & c_{13} & . & . & . & c_{1k} \\ c_{21} & c_{22} & c_{23} & . & . & . & c_{2k} \\ c_{31} & c_{32} & c_{33} & . & . & . & c_{3k} \\ . & . & . & . & . & . & . \\ . & . & . & . & . & . & . \\ . & . & . & . & . & . & . \\ c_{k1} & c_{k2} & c_{k3} & . & . & . & c_{kk} \end{pmatrix}. \tag{3.9}$$

From above relations it follows that,

$$\mathbf{XX}^T = \mathbf{EA}(\mathbf{E}^T\mathbf{A}^T) = \mathbf{EAA}^T\mathbf{E}^T = \mathbf{E}(\lambda\mathbf{I})\mathbf{E}^T = \mathbf{E\Lambda E}^T = \mathbf{\Lambda EE}^T$$

The orthogonal basis functions $u_i(s)$ are typically obtained from computing the eigenvalues/eigenvectors of the covariance matrix c_i based on dataset,

$$c_i u_i = \lambda_i u_i \tag{3.10}$$

where λ_i are the eigenvalues.

However, EOF technique is mainly based on using the spatial correlation of continuous field variable, i.e. covariance matrix only considers simultaneous information (in time) between grid points. Dynamical structures such as oscillations, propagation structures, and trends are ignored in the conventional EOF technique. In an attempt to capture propagation structures, EOF has been generalized into Extended EOF (EEOF) (Weare and Nasstrom, 1982) and Hillbert EOF (HEOF) (e.g., Rasmusson et al., 1981; Von Storch, 1999). Unlike EEOF, HEOF method does not explicitly incorporate the lagged information, hence it avoids using lagged auto-covariance matrix and thus

avoiding the problems associated with choosing the lag-window. Magnitude of spatial EOF pattern can be forced to change with time using complex part of the continuous time series,

$$Y(t) = A \cdot exp(i\omega t) + \Phi \tag{3.11}$$

are used in the analysis. A is the wave amplitude, while ω and ϕ are its frequency and phase shift (at the origin). More details related to the theory and implementation of EEOF and HEOF can be obtained from several studies (e.g., Rasmusson et al., 1981; Weare and Nasstrom, 1982; Von Storch, 1999). Here, EOF analysis is used in modelling the vertical $\mathbf{E} \times \mathbf{B}$ drift for the first time. EOF technique used in this study is based on spatial correlation. It has been valuable in other ionospheric studies including modelling of critical frequency, $f_o F2$ (Zhang et al., 2011); peak height, $h_m F2$ and propagation factor $M(3000)F_2$ (Zhang et al., 2009, 2010) of the F2-layer, and total electron content (TEC) (e.g. A et al., 2011; Uwamahoro and Habarulema, 2015).

3.3.2 Partial Least Squares (PLS)

PLS regression is a multivariate method which has been proven to be particularly suited to highly collinear data (Dhanjal et al., 2009; Montgomery et al., 2012). Since its discovery, PLS technique has been mainly used in the field of chemometrics (e.g., Wold et al., 1966, 1984; Lindberg et al., 1983; Geladi and Kowalski, 1986; Höskuldsson, 1988) and has also found applications in modelling and process monitoring (e.g., Fuller et al., 1988; Wise and Ricker, 1990; Qin, 1998; Rosipal and Krämer, 2006; Helland et al., 1992). PLS is well established framework for estimation, regression, and classification whose main objective is predicting a set of dependent variables (responses or even one response) from a set of independent variables (predictors) through the extraction of a small number of latent variables (also known vectors/components). An introduction to PLS is well presented in another sources (e.g., Manne, 1987; De Jong, 1993). Assuming linearly related set of predictors ($\mathbf{X}$) and responses ($\mathbf{Y}$) as matrices then,

$$\mathbf{Y} = \mathbf{X}\mathbf{A} + \mathbf{R_n}, \tag{3.12}$$

where $\mathbf{A}$ and $\mathbf{R_n}$ are coefficients and noise matrices, respectively. PLS uses principal component analysis (PCA) on both predictor ($\mathbf{X}$) and response ($\mathbf{Y}$) variables, while their relationship is mainly governed by covariance. PLS regression method builds a linear model by decomposing both $\mathbf{X}$ and $\mathbf{Y}$ matrices into bilinear terms,

$$\mathbf{X} = \mathbf{T}\mathbf{P}^T + \mathbf{E} \quad \text{and} \quad \mathbf{Y} = \mathbf{U}\mathbf{Q}^T + \mathbf{F} \tag{3.13}$$

where $\mathbf{T}$ and $\mathbf{U}$ are matrices of latent vectors $\mathbf{t}_i$ and $\mathbf{u}_i$, while $\mathbf{P}$ and $\mathbf{Q}$ are corresponding matrices of loading vectors $\mathbf{p}_i$ and $\mathbf{q}_i$, and $\mathbf{E}$ and $\mathbf{F}$ are residuals corresponding to $\mathbf{X}$ and $\mathbf{Y}$ respectively. $\mathbf{P}^T$ and $\mathbf{Q}^T$ are transpose matrices of $\mathbf{P}$ and $\mathbf{Q}$, respectively. Since the latent vectors are determined iteratively, $\mathbf{t}_1$ and $\mathbf{u}_1$ correspond to the first set of latent vectors and they are eigenvectors of $\mathbf{XX}^T\mathbf{YY}^T$ and $\mathbf{YY}^T\mathbf{XX}^T$, respectively (Manne, 1987; Wold et al., 1993; Montgomery et al., 2012). Since $\mathbf{YY}^T\mathbf{XX}^T$ is the transpose of $\mathbf{XX}^T\mathbf{YY}^T$ and vice versa, both matrices have identical eigenvalues (e.g., Montgomery et al., 2012). The above defined the PLS outer model, while latent vectors $\mathbf{t}_i$ and $\mathbf{u}_i$ define PLS inner model given as,

$$\mathbf{u}_1 = b_1\mathbf{t}_1 + \mathbf{r}_1 \tag{3.14}$$

where b_1 is the coefficient and $\mathbf{r}_1$ is residual of the first latent vector. The second and other higher order latent vectors are determined from residuals. Nonlinear Iterative PArtial Least Squares (NIPALS) and Statistical Inspired Modification to Partial Least Squares (SIMPLS) describe the iterative algorithms generally followed in the PLS regression technique. For this study, the PLS modelling technique is centered on NIPALS. While it is difficult for PLS method to model time varying processes, recursive PLS (RPLS) algorithms were first reported by Helland et al. (1992) and later improved to allow an existing model to get updated for every new observations added (Dayal and MacGregor, 1997; Qin, 1993; Wang et al., 2003). RPLS techniques are mainly used in the industrial process monitoring (e.g., Wang et al., 2003). Some of the algorithms related to RPLS are discussed in details by Qin (1998). As there are several algorithms implemented by PLS technique, this work provides detailed description of NIPALS which is used throughout, and also describes SIMPLS which is common alternative algorithm.

3.3.2.1 Nonlinear Iterative PArtial Least Squares (NIPALS)

NIPALS is the simplest algorithm used in PLS technique. This algorithm is initialized with a random value of the latent vector $\mathbf{u}_i$ (Geladi and Kowalski, 1986). Given that $\mathbf{Y}$ is one-dimensional, NIPALS assigns $\mathbf{u}_0$ values to first latent vector $\mathbf{u}_1$ as a random 1-dimensional vector or uses $\mathbf{Y}$ as a vector (**step** (a)) for initialization of the iterative process. A series of latent vectors (orthogonal components) $\mathbf{t}$ and $\mathbf{u}$ which are principal components describing the partial regression of $\mathbf{Y}$ on $\mathbf{X}$ in the orthogonal subspace are computed stepwise. An iterative process is used to find a set of weights $\mathbf{w}$ and $\mathbf{c}$ such that $\mathbf{X}$ and $\mathbf{Y}$ are represented in orthogonal subspaces as latent vectors $\mathbf{t} = \mathbf{Xw}$ and $\mathbf{u} = \mathbf{Yc}$, with constraints that $\mathbf{w}^T\mathbf{w} = 1$, $\mathbf{t}^T\mathbf{t}$ and $\mathbf{t}^T\mathbf{u}$ be maximal (e.g.,

Geladi and Kowalski, 1986; Rosipal and Krämer, 2006; Ciclo and Stefania, 2013). The iterative process starts with estimates of first latent/orthogonal vectors leading to a PLS model and process defined as follows,

1. $\mathbf{X}_1 = \mathbf{X}$, $\mathbf{Y}_1 = \mathbf{Y}$ ($\mathbf{Y}$ is 1-dimensional since one parameter $\mathbf{E} \times \mathbf{B}$ drift is being modeled. The process iterates over i PLS components commonly known as latent/orthogonal vectors.)

2. Iterate over i until $\mathbf{X}_i^T \mathbf{X}_i = 0$: ($\mathbf{u}_0$ (random number or $\mathbf{Y}$) initializes the process)

    (a) $\mathbf{u}_1 = \mathbf{u}_0$;

    (b) $\mathbf{w}_i = \frac{\mathbf{X}_i^T \mathbf{u}_i}{\mathbf{u}_i^T \mathbf{u}_i}$ (compute covariance weight $\mathbf{w}_i$);

    (c) $\mathbf{t}_i = \mathbf{X}_i \mathbf{w}_i$ and calculate corresponding loading vector $\mathbf{p}_i = \frac{\mathbf{X}_{i-1}^T \mathbf{t}_i}{\mathbf{t}_i^T \mathbf{t}_i}$;

    (d) $\mathbf{c}_i = \frac{\mathbf{Y}_i^T \mathbf{t}_i}{\mathbf{t}_i^T \mathbf{t}_i}$;

    (e) $\mathbf{u}_i = \mathbf{Y}_i \mathbf{c}_i$ and calculate corresponding loading vector $\mathbf{q}_i = \frac{\mathbf{Y}_{i-1}^T \mathbf{u}_i}{\mathbf{u}_i^T \mathbf{u}_i}$;

    (f) $\mathbf{E}_i = \mathbf{X}_{i-1} - \mathbf{t}_i \mathbf{p}_i^T$ and $\mathbf{F}_i = \mathbf{Y}_{i-1} - \mathbf{u}_i \mathbf{q}_i^T$ (return information contained within i-th set of vectors while the next components contain information that can be extracted from residuals ($\mathbf{E}_i$ and $\mathbf{F}_i$) by repeating steps (b)-(f).)

Upon convergence of each i-th iteration, $\mathbf{Y}$ is partially regressed on residual $\mathbf{E}$ which was computed from previous step until $\mathbf{X}$ is an empty matrix. As can be seen from NIPALS algorithm (**steps** (a)-(f)), partial regression of $\mathbf{Y}$ on $\mathbf{X}$ involves computing the covariance weight $\mathbf{w}$ (**step** (b)) and then computing latent vector of predictors $\mathbf{t}$ (**step** (c)). Therefore $\mathbf{Y}$ is regressed on the linear combination of the inputs set (**step** (d), $\mathbf{t} = \mathbf{a}_1 \mathbf{x}_1 + \mathbf{a}_2 \mathbf{x}_2 + ... + \mathbf{a}_k \mathbf{x}_k = \mathbf{X}\mathbf{w}$), so that the weight $\mathbf{c}$ which is used for projection is computed. Here k refers to the total number of inputs represented in $\mathbf{X}$. Loading vectors $\mathbf{p}$ and $\mathbf{q}$ in (**step** (c)) and (**step** (e)) are coefficients of regressing $\mathbf{X}$ on $\mathbf{t}$ and $\mathbf{Y}$ on $\mathbf{u}$. Hence the PLS model $\hat{\mathbf{Y}}$ can be fitted if the requirements and constraints in **steps** (a)-(f) are satisfied. Since $\mathbf{Y} = \mathbf{U}\mathbf{Q}^T + \mathbf{F}$, the estimated response $\hat{\mathbf{Y}}$ is the sum of m optimal latent vectors,

$$\hat{\mathbf{Y}} = \sum_{i=1}^{m} \mathbf{t}_i \mathbf{b}_i \quad \text{where,} \quad \mathbf{b}_i = \mathbf{u}_i^T \mathbf{t}_i (\mathbf{t}_i^T \mathbf{t}_i)^{-1} \tag{3.15}$$

3.3.2.2 Statistical Inspired Modification to Partial Least Squares (SIMPLS)

Latent vectors described above can be calculated from original variables $\mathbf{X}$ and $\mathbf{Y}$ in SIMPLS algorithm (De Jong, 1993). The variables are first centered $\mathbf{X}_0$ and $\mathbf{Y}_0$ prior to the computation

of latent vectors. Learning with SIMPLS algorithm is advantageous since it does not explicitly enforces updating $\mathbf{X}_0$ and $\mathbf{Y}_0$ after each iteration, thus making it computational faster than PLS based on NIPALS algorithm (Martins et al., 2010). SIMPLS algorithm starts by constructing the covariance matrix $\mathbf{S} = \mathbf{X}_0^T\mathbf{Y}_0$. Singular value decomposition (SVD) is used to find the left and right eigenvectors, $\mathbf{r}_1$ and $\mathbf{c}_1$ from $\mathbf{S}$, respectively. The first latent and loading vectors of $\mathbf{X}$ are then calculated as $\mathbf{t}_1 = \mathbf{X}_0\mathbf{r}_1$ and $\mathbf{p}_1 = \mathbf{X}_0^T\mathbf{t}_1$, respectively. The next stage is updating the $\mathbf{S}$ which is then used to compute the next set of vectors, i.e., $\mathbf{S} = \mathbf{S} - \mathbf{p}_1(\mathbf{p}_1^T\mathbf{p}_1)^{-1}\mathbf{p}_1^T\mathbf{S}$. The algorithm follows the steps below.

1. $\mathbf{S} = \mathbf{X}_0^T\mathbf{Y}_0$

2. for i = 1 to k

   (a) if $i = 1, [\mathbf{u}, \mathbf{s}, \mathbf{v}] = \mathrm{SVD}(\mathbf{S})$

   (b) if $i > 1, [\mathbf{u}, \mathbf{s}, \mathbf{v}] = \mathrm{SVD}(\mathbf{S} - \mathbf{P}_{i-1}(\mathbf{P}_{i-1}^T\mathbf{P}_{i-1})^{-1}\mathbf{P}_{i-1}^T\mathbf{S})$

   (c) $\mathbf{r}_i = \mathbf{u}(:,1)$ first left singular vector

   (d) $\mathbf{t}_i = \mathbf{X}_0\mathbf{r}_i$

   (e) $\mathbf{p}_i = \mathbf{X}_0^T\mathbf{t}_i/(\mathbf{t}_i^T\mathbf{t}_i)$

3. end

where $\mathbf{u}$ $(m \times m)$ and $\mathbf{v}$ $(n \times n)$ are real or complex left and right singular vectors, while $\mathbf{s}$ $(m \times m)$ is diagonal rectangular matrix with positive diagonal elements (Golub and Van Loan, 1996). The resulting $\mathbf{t}_i$, $\mathbf{r}_i$, $\mathbf{p}_i$ and $\mathbf{c}_i$ are then stored in $\mathbf{T}_k$, $\mathbf{R}_k$, $\mathbf{P}_k$ and $\mathbf{C}_k$ matrices, respectively. Therefore, estimated coefficient is $\mathbf{B}_{PLS} = \mathbf{R}_k(\mathbf{T}_k^T\mathbf{T}_k)^{-1}\mathbf{T}_k^T\mathbf{Y}_0$, such that $\hat{\mathbf{Y}}_0 = \mathbf{B}_{PLS}\mathbf{X}_0$.

3.3.2.3 PLS summary

For the first time, PLS technique is being investigated for ionospheric modelling. Since it was discovered in the field of chemometrics, it is inherently capable of estimating multiple responses using the same set of inputs. Therefore its success in the field of ionospheric studies can be advantageous.

3.3.3 Neural Networks (NNs)

The development of artificial neural networks was motivated by functioning of biological neurons in a human brain. Desirable characteristics of human brain include (1) learning ability, (2) massive parallelism, (3) distributed representation and computation, (4) adaptivity, (5) inherent contextual information processing, (6) low energy consumption, (7) fault tolerance, and (8) generalization ability (Lippmann, 1987; Jain et al., 1996). However, advancement in technology enables digital computers to outperform humans' capabilities in the domain of numeric computation and related manipulation (Lippmann, 1987; Jain et al., 1996). A neural network (NN) is a computer software which uses a set of processing units (neurons) in a manner nearly analogous to biological neurons in the human brain (e.g., Jesan and Lauro, 2003). The ability of NNs to learn underlying rules (relationships between inputs and outputs) make it more attractive over traditional techniques for classification, function estimation, forecasting and optimization. McCulloch and Pitts (1943) describes NNs with a set of n input signals, x_i $(i = 1, 2, 3, ..., n)$ through neurons which generates an output y if the corresponding weighted sum is above a certain binary threshold value u, otherwise an output is zero. They made simplifying assumptions that are different from biological neurons and yielded a mathematical relationship,

$$y = \theta \left(\sum_{i=1}^{n} w_i x_i - u \right) \tag{3.16}$$

where θ is a binary unit step function at 0, w_i is the weight of associated i-th input. Depending on the nature of problem, there have been a generalization of McCulloch-Pitts neuron, e.g., replacing θ in equation (3.16) with other activation functions such as sigmoid, Gaussian, *tanh* functions (e.g., Kalman and Kwasny, 1992). There are several NN algorithms for different applications (e.g., Specht, 1991; Fausett, 1994; Haykin, 1994; Zell et al., 1995; Bataineh and Marler, 2017; Qiao et al., 2017). For example, feed-forward and recurrent networks are generally known NN and employ different learning rules (Elman, 1990; Haykin, 1994; Watson, 2012). For this study, the feed-forward NN was explored and is briefly described below. Recurrent networks which follow different algorithms are also briefly described for comparative purposes.

3.3.3.1 Feed-forward NNs

NNs pass and process information fed into input, hidden and output layers (units) where connections between layers are all fed into the next layer and therefore no closed paths within the entire

network connections (e.g., Fausett, 1994; Watson, 2012). Back-propagation is a popular learning algorithm of updating connection weights since error information is fed from output layer backwards. Supervised, unsupervised and hybrid learning algorithms refer to a procedure of updating the connection weights of a NN (e.g., Rumelhart and Mcclelland, 1986; Fausett, 1994). Figure 5.11 shows a schematic illustration of the feed-forward NN setup. Each layer can be customized to have different number of neurons during the NN implementation depending on the amount of data being dealt with (Haykin, 1994). It is desirable to speed up the training time required for optimization; therefore increasing the number of hidden layers may make training the neural network easier (Haykin, 1994; Fausett, 1994). Three main stages define back-propagation algorithm (Fausett, 1994),

1. Feed-forward of the input pattern to the input layer,

2. The computation of responses and back-propagation of the errors,

3. Adjustment of the randomly assigned synaptic weights.

In the following description, the notation and mathematical relations in the algorithm are based on material found in Fausett (1994). Feed-forward of input patterns $\mathbf{X}_i, i = 1, 2, 3, ..., n$ via input layer into hidden layer is the first step in neural network shown in Figure 5.11. Each hidden neuron $\mathbf{Z}_j, i = 1, 2, 3, ..., p$ sums the weighted signals from these patterns,

$$z_j^{in} = \upsilon_{0j} + \sum_{i=1}^{n} x_i \upsilon_{ij}, \qquad (3.17)$$

where υ_{0j} refers to bias on the hidden layer neuron j and υ_{ij} is the connection weight between input neuron i and hidden neuron j. The activation function determines the state of each neuron based on its bias/threshold weights of incoming connections and on the states of the neurons connected to it by these connections (e.g., Müller et al., 1990). Random values within some interval, e.g.,(-1,1) are used to initialize the weights at the start of the training in order to achieve generalization. Different activation functions exist, however they should satisfy several characteristics such as being continuous, differentiable, and monotonically non-decreasing (e.g., Müller et al., 1990; Kalman and Kwasny, 1992).

Hidden neurons compute the activation function $z_j = f(z_j^{in})$ and broadcast the response z_j onto the output layer $(\mathbf{Y}_k, k = 1, 2, 3, ..., p)$; weighted sum of z_j are computed as follows,

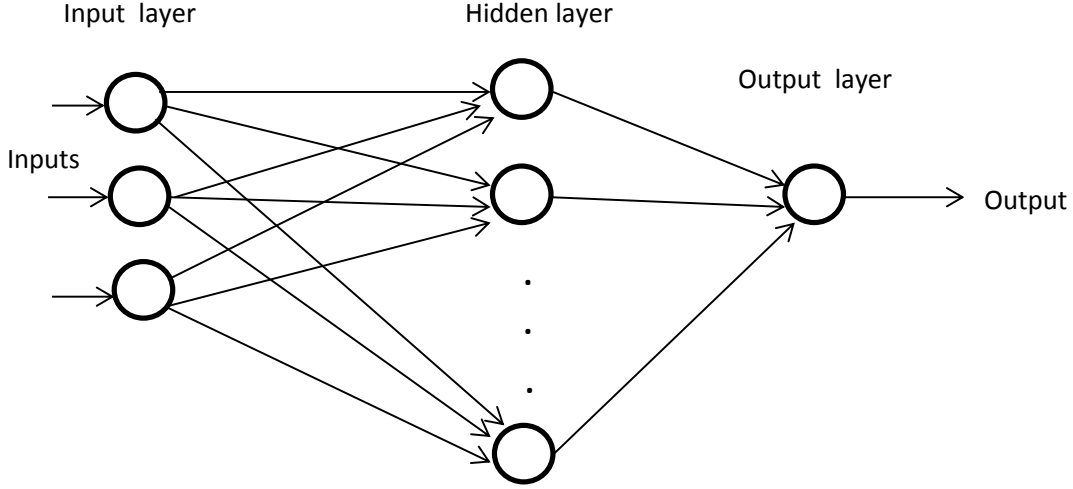$$y_k^{ni} = \omega_{0k} + \sum_{j=1}^{p} z_j \omega_{jk}, \qquad (3.18)$$

Figure 3.8: Schematic showing architecture of feed-forward artificial neural network.

where ω_{0k} refers to bias on the output layer neuron k and ω_{jk} is the connection weight between hidden neuron j and output neuron k. Activation functions are used to calculate the output pattern given by $y_k = f(y_k^{in})$ and this ends the first feed-forward process of the training patterns. One complete feed-forward process defines one epoch. For each estimated response y_k, individual output neuron $(\mathbf{Y}_k, k = 1, 2, 3..., m)$ receives a target pattern corresponding to the input training pattern $\mathbf{X}_i$ and calculates its error information term;

$$\delta_k = (t_k - y_k) f'(y_k^{in}), \tag{3.19}$$

where t_k refers to the target response and δ_k are used to compute weight correction $\triangle\omega_{jk} = \alpha\delta_k z_j$ and bias correction $\triangle\omega_{0k} = \alpha\delta_k$ terms, where α is the learning rate. Subsequently, δ_k are broadcasted back onto neurons in the hidden layer. Since, the error information is being back propagated the weighted δ_k signals are summed,

$$\delta_j^{in} = \sum_{k=1}^{m} \delta_k \omega_{jk} \tag{3.20}$$

In the hidden layer, the error information received by individual neuron is defined as follows,

$$\delta_j = \delta_j^{in} f'(z_j^{in}), \tag{3.21}$$

which is then used to update the υ_{ij}, computed as $\triangle\upsilon_{ij} = \alpha\delta_j x_i$. Subsequently, the bias correction term $\triangle\upsilon_{0j} = \alpha\delta_k x_j$ is computed. Therefore, updates on weights and biases are defined as follows,

(a) For each output neuron $(\mathbf{Y}_k, k = 1, 2, 3..., m)$, the weights and corresponding bias $(j = 0, ..., p)$ are given as follows,

$$\omega_{jk}(\text{current}) = \omega_{jk}(\text{previous}) + \triangle\omega_{jk}. \tag{3.22}$$

42

(b) In the hidden layer, each neuron ($\mathbf{Z}_j, i = 1, 2, 3..., p$) also updates its weights and bias ($i = 0, ..., n$):

$$v_{jk}(\text{current}) = v_{jk}(\text{previous}) + \triangle v_{jk}. \tag{3.23}$$

When training the NN, the data is split into training, validation and testing sets. As the name suggests, training dataset is used for training the NN through the adjustment of weights between neurons in the input, hidden and output layers, while the validation dataset is used to measure the performance of the NN on patterns that were left out during the training process. Subsequently, the overall performance of the NN (Zell et al., 1995) is assessed using testing dataset.

3.3.3.2 Recurrent Neural Networks (RNNs)

A recurrent NN (RNN) is different from standard feed-forward network since it can contain several feed-back connections to allow activations to flow around in a loop (Hecht-Nielsen, 1990; Elman, 1990; Haykin, 1994; Fausett, 1994). RNNs are used in learning time varying patterns and they can have different forms, such as Jordan network, Hopfield network, Echo state network, and Elman network (e.g., Karunanithi et al., 1992; Jaeger, 2001; Haykin and Network, 2004; Elman, 1990). Figure 3.9 shows Elman network comprising of input neurons, hidden neurons, one output neuron and the context neurons.
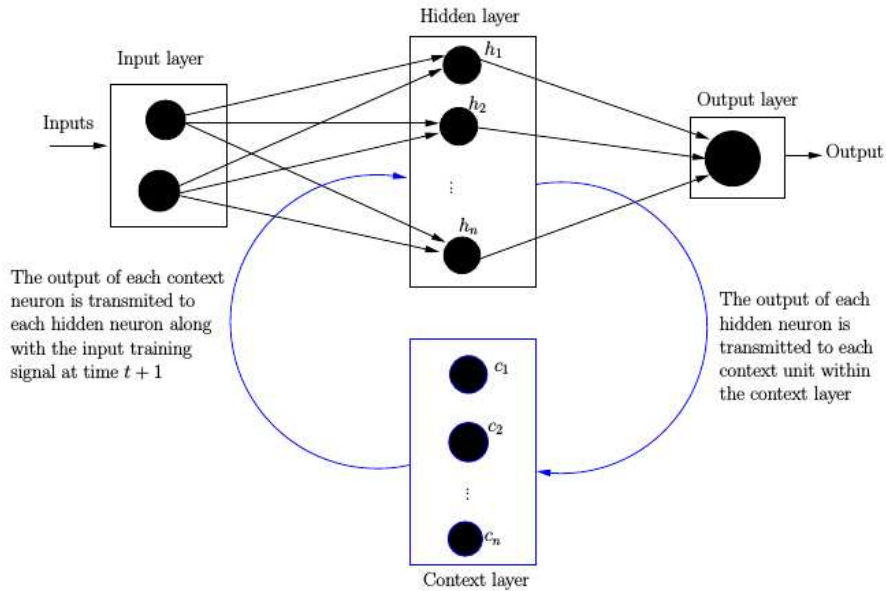

Figure 3.9: Schematic illustration of a simple Elman network with one input, one hidden and one output layer (Habarulema, 2011).

One common type is the standard multi-layer NN with added feed-back loop. For recurrent network which uses multi-layered NN, one can exploit the powerful non-linear mapping capabilities and some form of memory (e.g., Jesan and Lauro, 2003). The outputs of each hidden neuron are propagated to each context neuron and back to neurons in the hidden layer along with the incoming training pattern at time, $t + 1$ from the input layer. The process is iterative and stops when the number of iterations specified within the network is complete. Unlike back-propagation network, weight adjustment of each copy of the network are obtained individually and averaged over the number of time steps used in the training process (e.g., Hertz et al., 1991; Fausett, 1994). Since RNN can be considered as back-propagation in time (Hecht-Nielsen, 1990) these NNs enable correction of the time delay between the corresponding input parameters and the output parameter during the training and validating processes. The major difference is the inclusion of an additional layer consisting of context neurons and therefore allowing hidden layer patterns to be fed back to themselves (Hecht-Nielsen, 1990; Elman, 1990). Therefore, the hidden layer has a corresponding context unit in the RNN and the number of hidden neurons is equal to the number of context units in the context or copy layer (Marra and Morabito, 2005). Detailed information and mathematical relations regarding RNN can be obtained in several sources (e.g., Karunanithi et al., 1992; Jaeger, 2001; Haykin and Network, 2004; Elman, 1990).

3.3.3.3 ANN summary

NNs have capacity to learn the underlying relationships between inputs and outputs in modelling. They have found many applications in ionospheric physics such as modelling electron densities and critical frequencies of different layers (e.g., Cander, 2015; McKinnell and Poole, 2001; Ma et al., 2005; Oyeyemi et al., 2007) and vertical plasma drift (Anderson et al., 2004). In this thesis, NNs are used as one of the modelling techniques to model vertical $\mathbf{E} \times \mathbf{B}$ drift based on C/NOFS drifts and magnetometer observations over the African sector.

3.4 Summary

This chapter provided details of the data sources with focus on magnetometer and C/NOFS vertical $\mathbf{E} \times \mathbf{B}$ drift measurements/observations. The procedure of deriving $\triangle H$ which corresponds to EEJ and hence local daytime vertical $\mathbf{E} \times \mathbf{B}$ was described. The process of minimizing outliers from

C/NOFS vertical $\mathbf{E} \times \mathbf{B}$ drift based on median and median absolute deviation (Huber, 1981) was demonstrated based on quiet and disturbed condition days. Finally, the EOFs, PLS and NNs modelling techniques utilized in thesis were presented.

Chapter 4

$\mathbf{E} \times \mathbf{B}$ drift model based on EOF technique

4.1 Introduction

This chapter presents the model estimating the vertical $\mathbf{E} \times \mathbf{B}$ drift using EOF technique for the first time. Most of the results and description in this chapter rely on the information presented in the published paper (Dubazane et al., 2017). The EOF decomposition of vertical $\mathbf{E} \times \mathbf{B}$ drift provides an opportunity to investigate its overall temporal variability over Addis Ababa, AAE (9.02°N, 38.77°E, 0.18°N geomagnetic). EOF basis functions and their associated coefficients are used in the analysis and vertical $\mathbf{E} \times \mathbf{B}$ drift modelling. As mentioned earlier, EOF technique has been used in ionospheric studies for modelling ionospheric parameters such as critical frequency of the F2 layer, $f_\circ F2$ (Zhang et al., 2011); peak height $h_m F2$ and propagation factor $M(3000)F_2$ (Zhang et al., 2009, 2010) of the F2-layer, and total electron content (TEC) (e.g. A et al., 2011; Uwamahoro and Habarulema, 2015). Derivation of vertical $\mathbf{E} \times \mathbf{B}$ drift from EEJ ($\triangle H$) which was used as observations is also described.

4.2 Magnetometer data and $\mathbf{E} \times \mathbf{B}$ drift observations

Vertical $\mathbf{E} \times \mathbf{B}$ drift is derived from horizontal magnetic field components (H) of low and equatorial stations based on the differential magnetometer approach (Rastogi and Klobuchar, 1990; Anderson et al., 2004; Yizengaw et al., 2014a). Vertical $\mathbf{E} \times \mathbf{B}$ velocities during local daytime

(0700–1700 LT) from 2008–2013 were derived using the empirical expression in equation (4.1) presented in Anderson et al. (2004),

$$\mathbf{E} \times \mathbf{B} = 5.2889 + 0.1947 \triangle H + 0.0001 \triangle H^2 + 0.0000021 \triangle H^3 \tag{4.1}$$

In Anderson et al. (2004), the relationship between $\mathbf{E} \times \mathbf{B}$ and $\triangle H$ was developed based on JULIA observations and magnetic field data for the period 2001–2003 over the Peruvian longitude sector. This relationship was argued to be applicable in other longitudinal sectors (Anderson et al., 2004), since the climatological daytime vertical ionospheric drifts over all the longitudinal sectors are similar (Scherliess and Fejer, 1999). It was later demonstrated applicable over the Peruvian, Phillipine and Indian sectors (e.g., Anderson et al., 2006; Anghel et al., 2007) and African sector (Yizengaw et al., 2012). However, it should be mentioned that the solar activity period used to derive the Anderson et al. (2004) relationship is different from the considered period (2008–2013) in this study. As will be shown later, the applicability of the relationship may depend on the solar activity period when the analysis is performed. In this study, the vertical $\mathbf{E} \times \mathbf{B}$ drift velocities derived from $\triangle H$ for the period 2008–2013 were used throughout the model development and validation in place of observations. However, data for year 2009 were not included since ETHI magnetometer was not operational. In this context, it is important to state that the period of our study includes the anomalous and prolonged solar minimum between solar cycles 23 and 24 (e.g., Chen et al., 2011; Liu et al., 2011; Bakunina et al., 2013; Solomon et al., 2013; Ezquer et al., 2014; Perna and Pezzopane, 2016). The transition period between solar cycles 23 and 24 especially during 2008–2009 exhibited lower thermospheric electron densities compared to the previous solar minimum (e.g., Solomon et al., 2013). There were complex variations in different solar activity indices (e.g., Perna and Pezzopane, 2016) and as a result, it was difficult to model/predict the solar indices for 2008–2009. This led to challenges in accurate modelling and predictions of ionospheric parameters even on a climatological basis (e.g., Bakunina et al., 2013; Zakharenkova et al., 2013). The solar extreme ultra-violet (EUV) radiation represents the main ionization source of the F2 ionospheric layer (e.g., Tobiska, 1996; Chen et al., 2012), explaining most variance (90%) of the ionospheric variability such as hmF2 and f_0F2 (e.g., Elias, 2014). Although solar flux index $F10.7$ correlates well with solar activity based on EUV and X-ray emissions (Solomon et al., 2013), it was shown that $F10.7$ cannot properly described ionospheric variations based on f_0F2 for the very anomalous minimum of solar cycle 23/24 (Perna and Pezzopane, 2016). Levels of geomagnetic

activity were also reduced in solar cycle 23/24 (e.g., Richardson, 2013; Selvakumaran et al., 2016), since geomagnetic activity results from coronal mass ejections (CMEs) and corotating interaction regions (CIRs) originating from the Sun that evolve through the interplanetary medium before impacting the magnetosphere (e.g., Brueckner et al., 1998; Gopalswamy et al., 2010). During the rise of cycle 24, interplanetary CMEs and high-speed stream storm activity were low in comparison with other cycles (e.g., solar cycle 20 and 23), and therefore no severe storm ($Dst < -200$ nT) was seen (Richardson, 2013; Selvakumaran et al., 2016). With regard to our modelling efforts, due to incomplete dataset especially for the ETHI station only 972 days in this period have data and moreover 219 of these days have incomplete dataset which are not included in the model development. Hence, only 753 days were available for the EOF model development. Out of these 753 days, data for 7 days (in different years) were randomly removed and reserved for model validation and hence 746 days were used in developing the EOF model. Figure 4.1 presents histograms showing the number of days (with complete data at 15 minute intervals from 0700–1700 LT) considered per month in a given year from 2008– 2013 (with exception of 2009) in EOF model development.

EOF model was developed using $\mathbf{E} \times \mathbf{B}$ values at 15-minutes intervals during daytime 0700–1700 LT, giving 41 values per day. The time period covered by the model is limited to 0700–1700 LT due to the approach used in estimating $\mathbf{E} \times \mathbf{B}$ drift data. The differential magnetometer approach reliably estimates EEJ and hence $\mathbf{E} \times \mathbf{B}$ drift during daytime only because the nighttime current is too weak to be detected by the magnetometer (e.g., Yizengaw et al., 2012, 2014a). Since EEJ can change abruptly on a day-to-day basis and especially during disturbed conditions, $\mathbf{E} \times \mathbf{B}$ data at 15-minute intervals will not be able to capture some EEJ dynamics. Based on the EOF modelling technique, the 15-minute intervals data was used since it gave larger data-points in comparison with high resolution (1-minute) $\mathbf{E} \times \mathbf{B}$ data.

4.3   E × B drift decomposition using EOF

The matrix of observations $\mathbf{D}$ was constructed by arranging day-to-day vertical $\mathbf{E} \times \mathbf{B}$ drift from 0700–1700 LT along y-axis (rows). Therefore columns of $\mathbf{D}$ show simultaneous temporal evolution of $\mathbf{E} \times \mathbf{B}$ drift for the period 2008–2013. Hence $\mathbf{D}$ has the dimensions of the total number of days (N) used in the modelling and local time (t) where $\mathbf{E} \times \mathbf{B}$ drift values were considered. Since
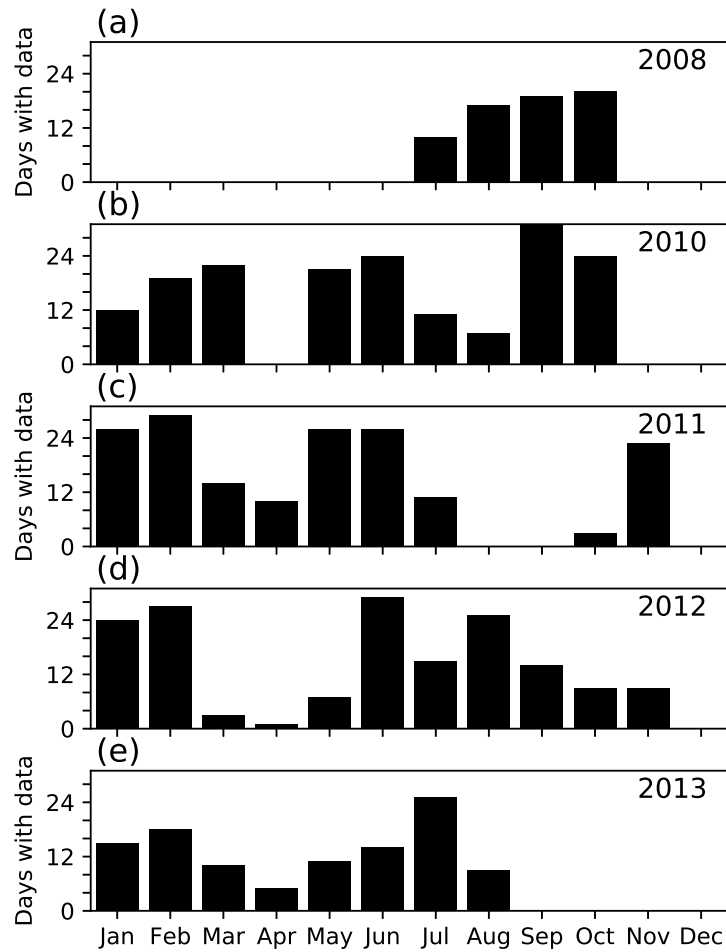
Figure 4.1: Histograms showing number of days per month between 2008 and 2013 (excluding 2009) with complete dataset at 15 minute intervals during 0700–1700 LT.

$N = 746$ days are used in EOF analysis during daytime (0700–1700 LT) where $\mathbf{E} \times \mathbf{B}$ drift values are taken at 15-minute intervals, $\mathbf{D}$ is a 746×41 matrix. $\mathbf{D}$ was used to compute the covariance matrix $\mathbf{C}$ which has $k \times k$ dimension as follows,

$$\mathbf{C} = \mathbf{D}\mathbf{D}^T = \begin{pmatrix} c_{11} & c_{12} & c_{13} & . & . & . & c_{1k} \\ c_{11} & c_{12} & c_{13} & . & . & . & c_{1k} \\ c_{11} & c_{12} & c_{13} & . & . & . & c_{1k} \\ . & . & . & . & . & . & . \\ . & . & . & . & . & . & . \\ . & . & . & . & . & . & . \\ . & . & . & . & . & . & . \\ c_{k1} & c_{k2} & c_{k3} & . & . & . & c_{kk} \end{pmatrix} \tag{4.2}$$

where $\mathbf{D}^T$ is a transpose of data matrix. For i and j sets of observations, entries of $\mathbf{C}$ are co-variance between the entries of $\mathbf{D}_i$ and $\mathbf{D}_j$ defined as,

$$c_{ij} = \frac{1}{N} \sum_{l=1}^{N} (\mathbf{D}_{li} - \bar{\mathbf{D}}_i)(\bar{\mathbf{D}}_{lj} - \bar{\mathbf{D}}_j) \tag{4.3}$$

where l refers to rows of matrix $\mathbf{D}$ and $\bar{\mathbf{D}}_i$ and $\bar{\mathbf{D}}_j$ are average values of the i-th and j-th $\mathbf{E} \times \mathbf{B}$ drift values, while N refers to the number of rows of $\mathbf{D}$ describing the temporal variability. The eigenvectors of $\mathbf{C}$ are $\mathbf{E}_k$, which describe temporal evolution of $\mathbf{E} \times \mathbf{B}$ drift for different orthogonal directions ($k = 41$) and are obtained from equation (e.g., Riley et al., 1999; Zhang et al., 2009),

$$\mathbf{C}\mathbf{E_k} = \lambda_k \mathbf{E}_k \tag{4.4}$$

where λ_k refers to a set of the corresponding eigenvalues. $\mathbf{C}$ is a square symmetric matrix defined by k orthonormal eigenvectors ($\mathbf{E}_k$) and corresponding λ_k which can be obtained by solving the characteristics equation,

$|\mathbf{C}_k\mathbf{E}_k - \lambda_k\mathbf{E}_k| = 0.$

Using the $\mathbf{E} \times \mathbf{B}$ drift values and computed $\mathbf{E}_k$ one can deduce the associated EOF coefficients $\mathbf{A}_k$ as follows

$$\mathbf{A}_k = \mathbf{D}\mathbf{E}_k^T \tag{4.5}$$

where $\mathbf{E}_k^T$ is a transpose of $\mathbf{E}_k$. Hence, observations were decomposed into a series of $\mathbf{E}_k$ and $\mathbf{A}_k$ as follows,

$$\mathbf{E} \times \mathbf{B}(t, d) = \sum_{k=1}^{N=41} \mathbf{A}_k(d)\mathbf{E}_k(t). \tag{4.6}$$

Table 4.1: The first ten EOF components describing variance of $\mathbf{E} \times \mathbf{B}$ drift.

EOF component	Proportion of Variance(%)	Cumulative Proportion of Variance(%)
A1×E1	51.41	51.41
A2×E2	28.11	79.52
A3×E3	9.07	88.59
A4×E4	4.47	93.06
A5×E5	1.58	94.64
A6×E6	1.11	95.75
A7×E7	0.65	96.40
A8×E8	0.52	96.92
A9×E9	0.34	97.26
A10×E10	0.31	97.57

Since most variance of original observations are contained within the first few EOF components (Björnsson and Venegas, 1997), the series defined by equation (4.6) converges quickly. The cumulative proportion of variance Pr_p of the $\mathbf{E} \times \mathbf{B}$ dataset as represented by the first p EOF components is computed as follows,

$$Pr_p = 100 \times \frac{\sum_{k=1}^{p} \lambda_k}{\sum_{j=1}^{N=41} \lambda_j} \% \tag{4.7}$$

Similarly, the ratio of i-th eigenvalue to the sum of all eigenvalues indicates the proportion of the total variance in the original data explained by the i-th EOF component (Hannachi, 2004),

$$r_i = 100 \times \frac{\lambda_i}{\sum_{j=1}^{p} \lambda_j} \% \tag{4.8}$$

Hence, the order of importance of r_i which is known as variance decreases with increasing order of EOF components (PCs).

By considering $\mathbf{E} \times \mathbf{B}$ drift data distributed according to Figure 4.1, proportion of variance of each EOF component are shown in Table 4.1. The EOF components explaining lower than 1% of the total variance in the original dataset were regarded as noise and hence neglected. Therefore the first six EOF components representing 95.75% of original $\mathbf{E} \times \mathbf{B}$ drift dataset were used in EOF modelling. Figure 4.2 shows the variances of origin $\mathbf{E} \times \mathbf{B}$ drift dataset in a orthogonal subspace defined by $\mathbf{E} \times \mathbf{B}$. Since $\mathbf{E}_k$ are eigenvectors of $\mathbf{C}$, the diagonal entries of the covariance matrix provide variances of original $\mathbf{E} \times \mathbf{B}$ drift dataset for each k orthogonal direction. The elbow of the screeplot is often used as a guide of selecting the minimum number of EOF components which are necessary to represent the overall variation of the original dataset (Jolliffe, 2002). The elbow is found at the third orthogonal direction (E3) which is shown as third principal component (PC)
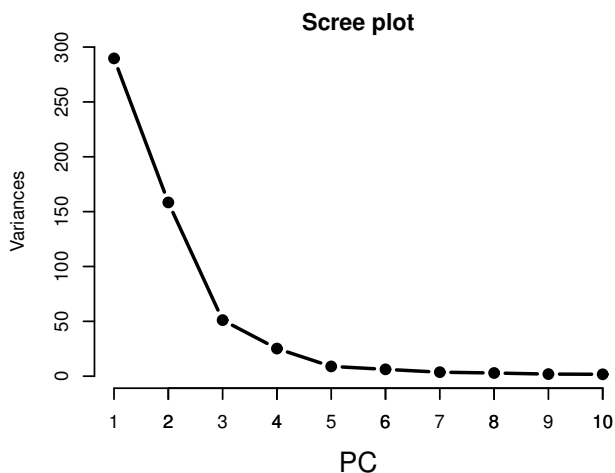
Scree plot

Figure 4.2: Schematic showing distribution of variances of the original dataset in $k = 10$ orthogonal directions ($\mathbf{E}_k$).

in Figure 4.2, thus at least three EOF components representing $\sim 89\%$ of original dataset could have to be used. Hereafter, the eigenvectors ($\mathbf{E}_k$) for each k direction is presented as 'Ek'.

Table 4.1 shows that the first and second EOF components represent $\sim 80\%$ of total variance of $\mathbf{E} \times \mathbf{B}$ drift showing how quickly the EOF series converges. The six EOF components represent $\sim 96\%$ of total variance of $\mathbf{E} \times \mathbf{B}$ drift while the remaining components account for $\sim 4\%$.

Figure 4.3 (a)-(b) shows first six EOF basis functions and the associated EOF coefficients. The dominant variation of the original dataset is represented by E1 (51.41%). E1 (black curve) is highly correlated (correlation coefficient, $R = 0.964$) with average $\mathbf{E} \times \mathbf{B}$ drift (blue curve). Hence, E1 can represent the diurnal variation of vertical drifts. Similarly, E3 (representing 9.07% of the original dataset) showed clear correlation ($R = 0.825$) with average vertical drifts. E2 which represents 28.11% of original $\mathbf{E} \times \mathbf{B}$ drift observations contains semi-diurnal variation (e.g., Anderson and Araujo-Pradere, 2010). With reference to temporal averaged $\mathbf{E} \times \mathbf{B}$ drift (blue curve), E3 is slightly shifted in time. Migrating semi-diurnal tides are thought to be a reason for such local time shift (e.g., Millward et al., 2001)

Figure 4.3 (b) shows variation of different associated EOF coefficients (A4-A6) over a period within 2008–2013. It should be noted that only 746 days within this period are included for analysis. The associated EOF coefficients provide spatial patterns over long period (2008–2013). The first EOF component A1 represents the long term changes of $\mathbf{E} \times \mathbf{B}$ drift with solar activity as will be demonstrated in subsection 4.3.1. Since other higher EOF components present smaller variability of $\mathbf{E} \times \mathbf{B}$ drift which is predominantly quiet during this period of study (e.g., Chen et al.,
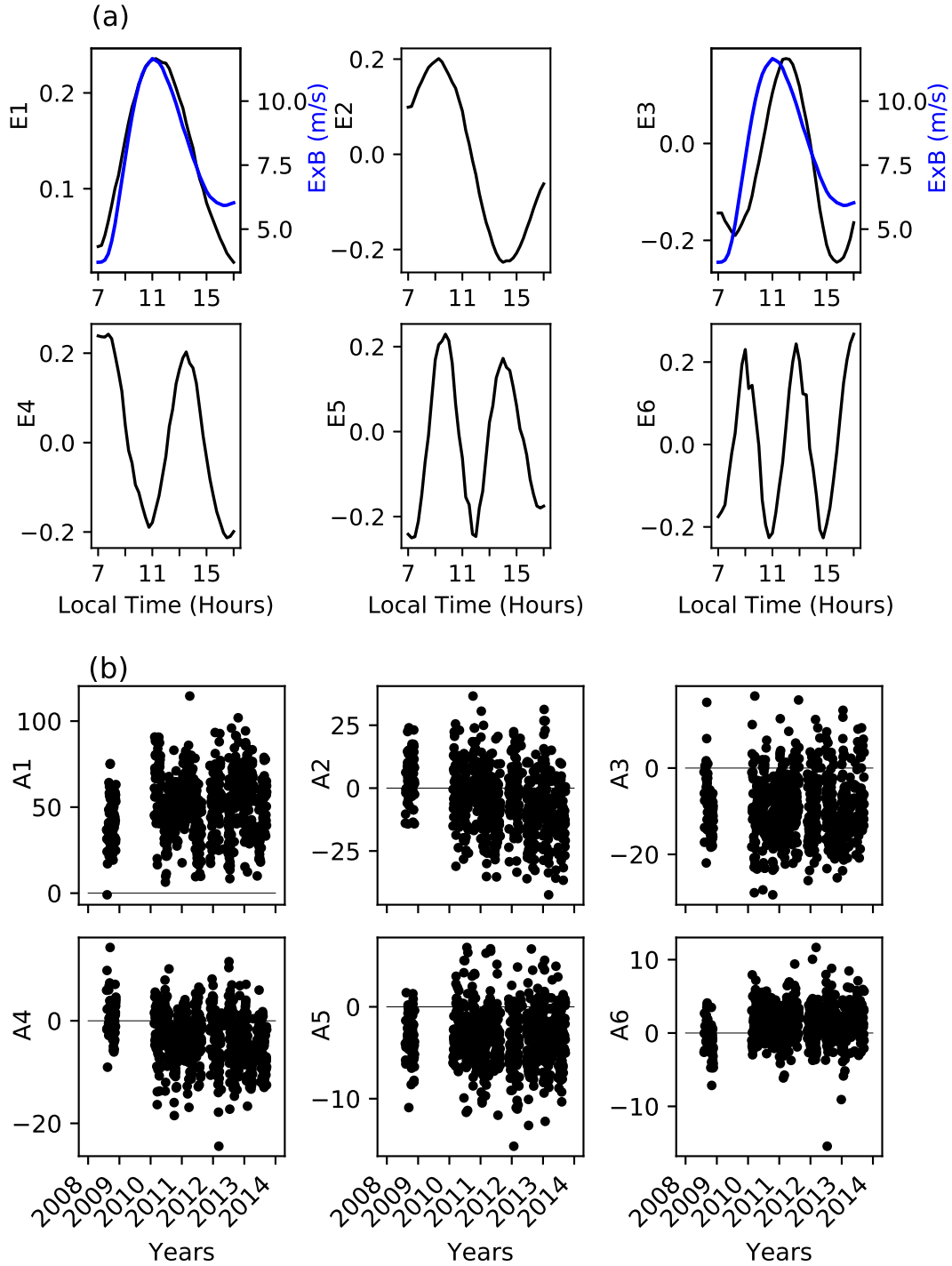
Figure 4.3: Diurnal variation of (a) EOF basis functions E1-E6, and (b) long-term variation of associated EOF coefficients for period 2008–2013. Diurnal averaged $\mathbf{E} \times \mathbf{B}$ drift (blue curve) is shown in the plots of E1 and E3 to show their agreement in variability.

2011; Richardson, 2013; Selvakumaran et al., 2016), the relationship of their associated coefficients (A1-A6) with geomagnetic activity (presented by Dst index) was investigated. Figure 4.4 shows
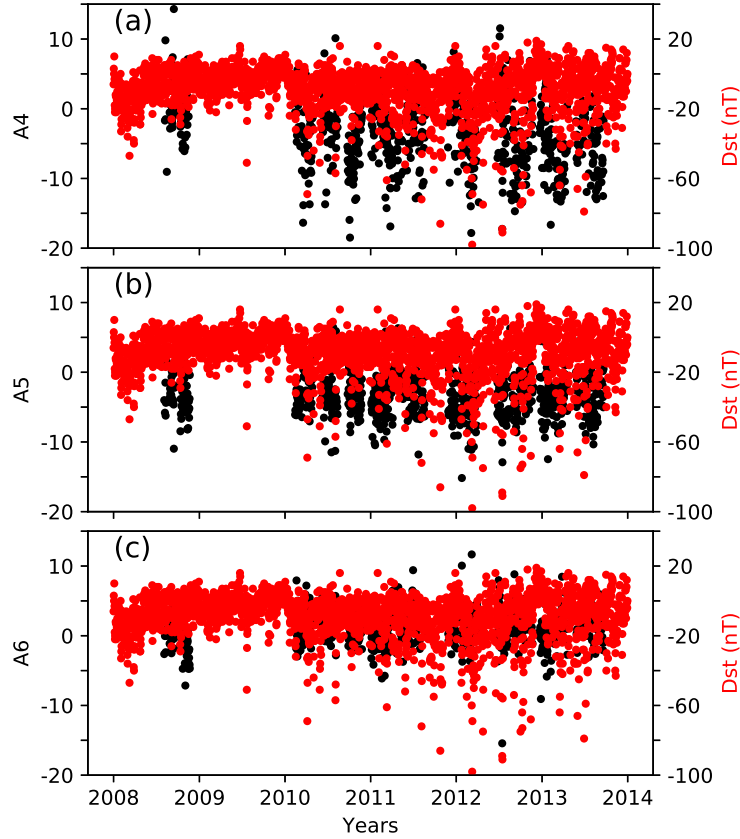
Figure 4.4: Comparison of *Dst* index with three EOF coefficients in panels (a)-(c) during the period within 2008–2013.

long term variation of *Dst* index (which measures the level of energy stored in the ring current) and changes of EOF coefficients (A4-A6) in panels (a)-(c). There is low or no correlation between *Dst* and A4-A6 which can be largely associated with unusual low geomagnetic activity levels observed during this period (e.g., Richardson, 2013; Selvakumaran et al., 2016). There was clear no correlation when A1-A3 (not shown) were compared with changes in *Dst* index.

4.3.1 Modelling of the EOF coefficients A_k

After $\mathbf{E} \times \mathbf{B}$ drift decomposition as shown in equation (4.6), A_k were modeled as a function of inputs which influence vertical drifts. Over one location, the main factors that play a major role in $\mathbf{E} \times \mathbf{B}$ drift variability on a long term include changes in solar activity and geomagnetic activity. Richmond (1973) established that an increase in $\triangle$H (which is proportional to daytime $\mathbf{E} \times \mathbf{B}$ drift) of 10% gave an equal increase (10%) in the maximum electron density of the ionospheric

E-layer (N_mE) over the same time period. The relationship between solar activity and $\mathbf{E} \times \mathbf{B}$ drift is well articulated in Anderson et al. (2004). In general daytime $\triangle$H represents EEJ changes ($\propto$ daytime $\mathbf{E} \times \mathbf{B}$ drift) that are proportional to the product of the ionospheric conductivity σ and the eastward electric field $\mathbf{E}$ in the low latitude E-region. At E region altitudes, the ionospheric conductivity and EEJ have a direct relationship with N_mE which mostly depends on the solar activity $F10.7$ (e.g., Richmond, 1973; Yamazaki et al., 2010; Hamid et al., 2013),

$$EEJ \propto \sigma\mathbf{E} \propto N_mE \propto F10.7 + \text{other factors} \tag{4.9}$$

Therefore in modelling $\mathbf{E} \times \mathbf{B}$ drift, it is appropriate to use a solar activity indicator representing the flux of the ionizing radiation which in this case is the solar radio flux $F10.7$. In contrast, our period of study includes very low values of solar activity which are characterizing the passage between solar cycles 23 and 24, with a weak correlation between the $\mathbf{E} \times \mathbf{B}$ drift and the solar index F10.7 (e.g., Chen et al., 2011; Liu et al., 2011; Solomon et al., 2013). It is well known that the low latitude electric field is influenced during disturbed conditions either due to the disturbed ionospheric dynamo (Blanc and Richmond, 1980) or by the penetrating electric fields of magnetospheric origin (e.g. Fejer et al., 1995; Scherliess and Fejer, 1997). Disturbed ionospheric dynamo leads to westward (eastward) electric field during local daytime (nighttime) while the effect of penetrating electric field is the exact opposite when the Bz component of interplanetary magnetic field (IMF Bz) is southward (Blanc and Richmond, 1980; Fejer and Scherliess, 1995). If the IMF Bz reverses from southward to northward abruptly, westward electric field may be induced within the low latitude ionosphere during daytime (e.g. Kelley et al., 1979; Wei et al., 2009) resulting into downward vertical drift. Eastward electric field increases $\mathbf{E} \times \mathbf{B}$ for local daytime low latitudes, while a westward electric field leads to a decrease in vertical drift. Since the storm-time equatorial/low latitude electric field depends on the level of geomagnetic activity (e.g., Scherliess and Fejer, 1997), the Dst index that represents energy stored in equatorial ring current can be used to account for geomagnetic dependence of $\mathbf{E} \times \mathbf{B}$ variability during modelling. Rastogi and Chandra (2015) used deviation of northward component of geomagnetic field $\triangle\mathbf{X}$ as a proxy of EEJ variation and obtained large correlation coefficient values of ≈ 0.75 and 0.95 between EEJ and Dst index during midday and midnight for days in September and October 1963. Therefore, Dst and $F10.7$ indices were used as inputs since the solar and geomagnetic activities influence the EEJ current and therefore $\mathbf{E} \times \mathbf{B}$ drift (e.g. Yamazaki et al., 2010; Hamid et al., 2013; Scherliess and Fejer, 1997). Considering that $\mathbf{E} \times \mathbf{B}$ drift has annual and semi-annual variations

(e.g. Chapman and Rao, 1965; Stening, 1995; Yamazaki et al., 2009) the associated coefficients were modeled (e.g. A et al., 2011) as follows,

$$A_k(d) = r_{k1}(d) + r_{k2}(d) + r_{k3}(d) + \epsilon_k \qquad (4.10)$$

where ϵ_k is the error associated with each estimate for $k = 1, 2, 3, 4, 5, 6$. The expressions, r_{k1}, r_{k2} and r_{k3}, are described as follows,

$$r_{k1} = a_{k1} + b_{k1}F10.7 + c_{k1}Dst \qquad (4.11)$$

$$r_{k2} = \{q_{k2} + e_{k2}F10.7 + g_{k2}Dst\}cos\left(\frac{2\pi d}{365.25}\right) + \{i_{k2} + j_{k2}F10.7 + s_{k2}Dst\}sin\left(\frac{2\pi d}{365.25}\right) \qquad (4.12)$$

$$r_{k3} = \{q_{k3} + e_{k3}F10.7 + g_{k3}Dst\}cos\left(\frac{4\pi d}{365.25}\right) + \{i_{k3} + j_{k3}F10.7 + s_{k3}Dst\}sin\left(\frac{4\pi d}{365.25}\right) \qquad (4.13)$$

A factor of 0.25 in the denominator of r_{k2} and r_{k3} accounts for leap years, while d represents day of the year. The coefficients a_{k1}, b_{k1}, c_{k1}, q_{k2}, e_{k2}, g_{k2}, i_{k2}, j_{k2}, s_{k2}, q_{k3}, e_{k3}, g_{k3}, i_{k3}, j_{k3} and s_{k3} were computed using least squares method.

From Figure 4.5 (a)-(b), there is a clear expected correlation (for most dataset) between solar activity and ionospheric vertical drifts. However, there seems to be a low correlation between $F10.7$ and $\mathbf{E} \times \mathbf{B}$ during the low solar activity (2008–2011). The reason for this low correlation may be partly related to the level of solar activity during which the relationship between $\triangle H$ and vertical drifts was developed by Anderson et al. (2004). Figure 4.6 shows variation of $F10.7$ index from 1995–2016.

The magenta block in Figure 4.6 shows the period of data availability used to develop the analytical expression by Anderson et al. (2004). The period covered by our model is indicated by the red block. Anderson et al. (2004) developed the expression between $\mathbf{E} \times \mathbf{B}$ and $\triangle H$ based on August 2001-December 2003 data, and as it can be seen in Figure 4.6, this period was more active than our low solar activity study period of 2008–2011. Moreover, it should be emphasized that relationship was developed over Jicamarca (Anderson et al., 2004), although it was demonstrated to be useful in other longitude sectors based on limited datasets in terms of temporal coverage (Anderson et al., 2006; Anghel et al., 2007; Yizengaw et al., 2012). Results in Figure 4.5 suggest
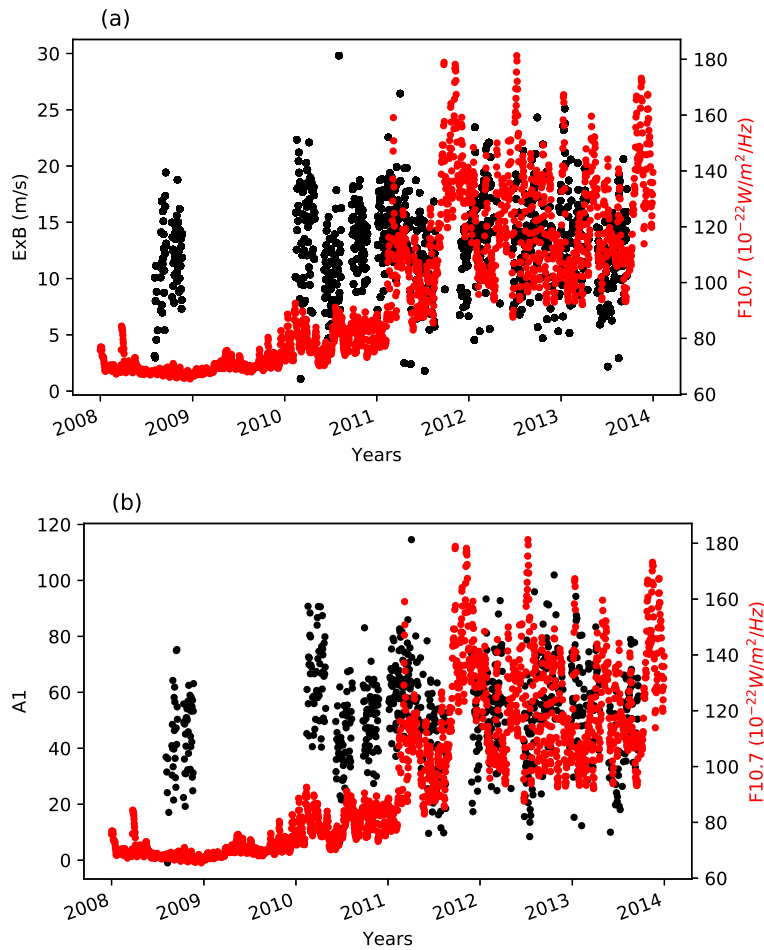
Figure 4.5: Comparison of (a) long-term mean of $\mathbf{E} \times \mathbf{B}$ drift from 1000-1200 LT and $F10.7$ index, (b) the first associated EOF coefficient A1 with $F10.7$ index for 2008–2013.

that the analytical expression in Anderson et al. (2004) may not be valid for all solar activity periods, especially for periods of very low and prolonged solar activity like the one characterizing the transition between solar cycles 23 and 24 (e.g., Chen et al., 2011; Liu et al., 2011; Solomon et al., 2013; Ezquer et al., 2014; Perna and Pezzopane, 2016).

4.4 Modelling results and discussion

4.4.1 Introduction

In this section vertical $\mathbf{E} \times \mathbf{B}$ drift derived for quiet $(K_p \leq 3)$ and disturbed $(K_p > 3)$ conditions were selected for validating the models. Vertical $\mathbf{E} \times \mathbf{B}$ drift velocities used for validation were removed from the dataset utilized in model development. However, it should be noted that
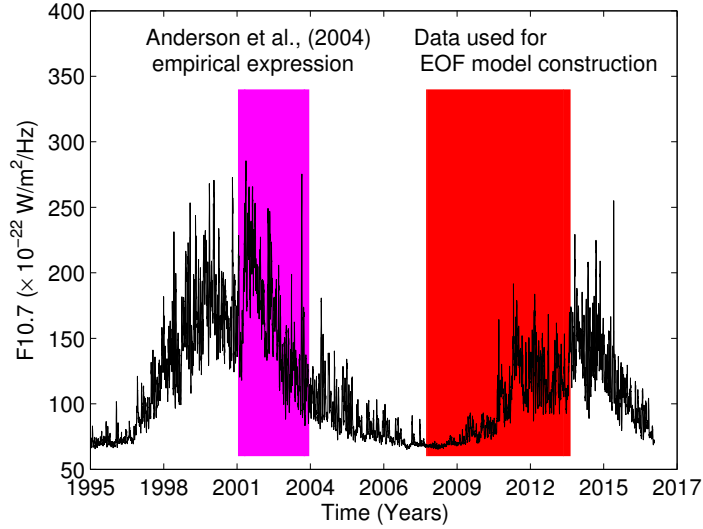
Figure 4.6: Variation solar flux index ($F10.7$) for a period 1995–2016. The magenta block shows the period when the analytical expression between vertical $\mathbf{E} \times \mathbf{B}$ drift and $\triangle H$ was developed by Anderson et al. (2004). The red block shows the period covered by the data used in the study to develop the EOF model based on vertical $\mathbf{E} \times \mathbf{B}$ drift estimated using Anderson et al. (2004) expression.

both datasets (for model development and validation) were derived using the same expression in Anderson et al. (2004). Where possible the C/NOFS $\mathbf{E} \times \mathbf{B}$ observations are used as an additional validation source. For quiet conditions, 6-days from complete (data-points=41 for each day during 0700–1700 LT) and incomplete (data-points<41 for each day during 0700–1700 LT) $\mathbf{E} \times \mathbf{B}$ datasets (which were not used in either decomposition or model development) were selected for different years within our period of study. Two disturbed periods (6-days) from 2011 (06-08 Jan 2011) and 2013 (18-20 Sept 2013) comprising of complete and incomplete $\mathbf{E} \times \mathbf{B}$ drift data was only used for model validation. It should be further emphasized that only 7-days of complete data was only reserved for model validation purposes, while the rest of days used for validation purposes consisted of $\mathbf{E} \times \mathbf{B}$ drift data with gaps (data-points<41 values per day) which was also not used in either decomposition or modelling.

4.4.2 Quiet conditions

The EOF model's results are presented alongside those of Scherliess-Fejer model (Scherliess and Fejer, 1997, 1999) in the estimation of day-to-day variability of $\mathbf{E} \times \mathbf{B}$ drift. Scherliess-Fejer model (here-

after, SF) was developed using vertical $\mathbf{E} \times \mathbf{B}$ drift observations from incoherent scatter radar, ISR (12.0°S, 76.9°W, magnetic dip 2°N) in Jicamarca while the low inclination Atmospheric Explorer E (AE-E) with ion drift meter (IDM) on-board provides longitudinal dependence of vertical ionospheric vertical drifts. The SF model was developed by fitting observations and inputs with cubic-B splines basis functions, while day of the year (d), solar flux (F10.7) and local time (t) were used as inputs (Scherliess and Fejer, 1999). Another quiet time vertical $\mathbf{E} \times \mathbf{B}$ drift model was developed by Fejer et al. (2008) using observations from Republic of China Satellite 1 (ROCSAT-1) for a period within 1999–2004. This model agrees well with SF model, however it showed more clear longitudinal effect that was lacking in the SF model. However, SF model still performs better during nighttime. For storm time, SF model uses auroral electrojet index as the main input and its results agree well with the disturbance dynamo model developed by Blanc and Richmond (1980). As mentioned earlier, the $\mathbf{E} \times \mathbf{B}$ drift used as observations were derived from the relationship by Anderson et al. (2004) which was found applicable in other longitude sectors such as (Peruvian, Philippine, and Indian) (e.g. Anderson et al., 2004, 2006; Anghel et al., 2007) and African sector (Yizengaw et al., 2012) due to the similarity of climatological daytime vertical drifts (Scherliess and Fejer, 1999) at all longitudes. Figure 4.7 shows a comparison of averaged vertical $\mathbf{E} \times \mathbf{B}$ drift from the quantitative relationship (Anderson et al., 2004) and climatological model (SF) in Peruvian, Philippine, Indian longitude sectors during quiet conditions (Anderson et al., 2006; Anghel et al., 2007). It is clear that the diurnal variation of average $\mathbf{E} \times \mathbf{B}$ drift inferred from $\triangle H$ agrees approximately with those from the SF model for most seasons and longitude sectors. However, the magnitude of the $\mathbf{E} \times \mathbf{B}$ drift values at different longitudes, local time and seasons are sometimes slightly different. Standard deviation corresponding to $\triangle H$ inferred vertical ionospheric drifts was about 5 m/s around noon and 2.5 m/s in the morning and afternoon hours. Therefore the overall $\triangle H$ inferred $\mathbf{E} \times \mathbf{B}$ drift over different longitude were comparing reasonable well with the SF model. With reported standard deviation values using climatological values, it is reasonable to expect higher differences when performing day-day $\mathbf{E} \times \mathbf{B}$ drift variability as seen in this chapter.

When available, in-situ C/NOFS $\mathbf{E} \times \mathbf{B}$ observations are included as an independent validation data source. Data from IVM instrument on-board the C/NOFS satellite was used as independent validation data source. The $\mathbf{E} \times \mathbf{B}$ drift at $\pm 6°$ geographic longitude over AAE and within the altitude range $\sim$ 400–500 km (e.g. Stoneback et al., 2011) near magnetic equator ($\pm$ 4.0° geomag-
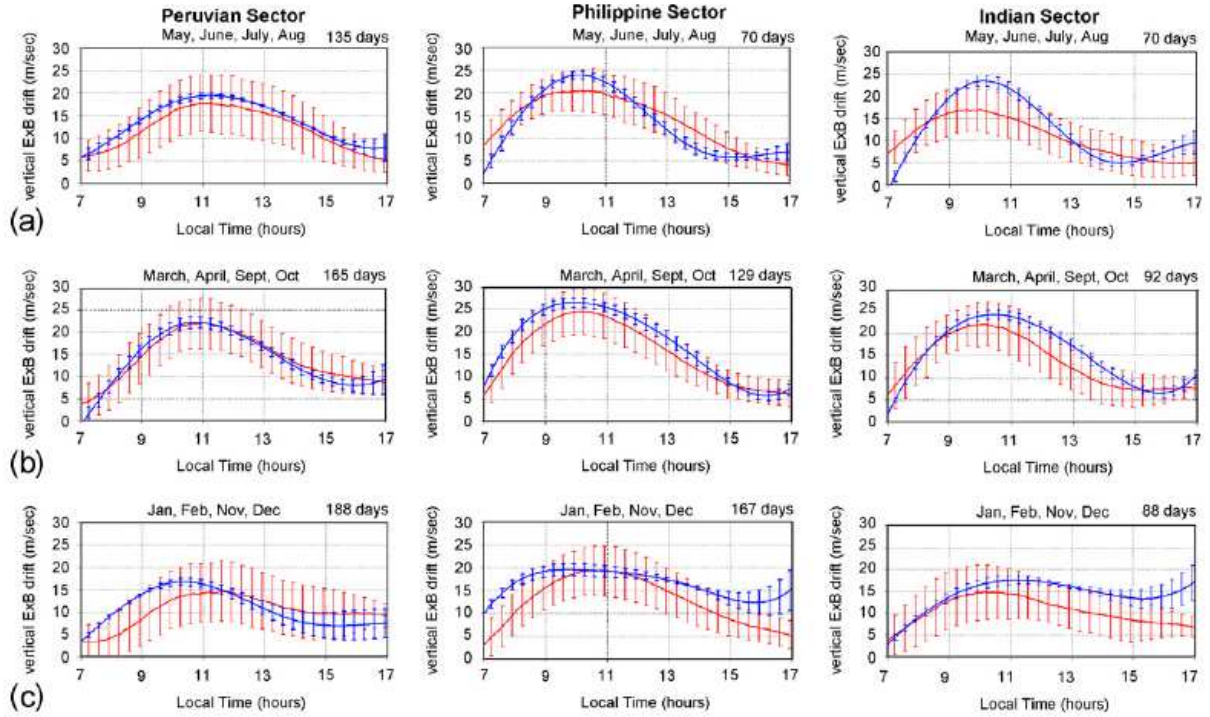
Figure 4.7: Comparison of quiet times averaged vertical $\mathbf{E} \times \mathbf{B}$ drift derived from magnetic field (red) (Anderson et al., 2004) and Scherliess-Fejer model (Scherliess and Fejer, 1999) (blue) for the equinox period, June and December solstices in Peruvian, Philippine and Indian longitude sectors. The number of quiet days used for a corresponding season and longitude are shown in each panel (Anghel et al., 2007).

netic) were considered for validating our EOF modeled results. Figure 4.8 shows diurnal variation of measured/observed $\mathbf{E} \times \mathbf{B}$ (black curve) drift, $\mathbf{E} \times \mathbf{B}$ estimated from EOF (magenta curve) and SF models (blue curve) for selected periods in 2008, 2010, 2011, 2012 and 2013 during quiet geomagnetic conditions ($K_p \leq 3$). In-situ C/NOFS observations are shown as red-dots. It is important to emphasize that the Anderson $\mathbf{E} \times \mathbf{B}$ drift data in Figure 4.8 (black curve) was not used in EOF model development and therefore gives an independent way of evaluating the model's performance. In a similar way, for the rest of the discussion, the validation data was independent of the model. In Figure 4.8, days 2008-09-06, 2012-12-28 and 2013-03-22 had incomplete $\mathbf{E} \times \mathbf{B}$ drift data, however models have advantage of filling in these data gaps.

From Figure 4.8, the determined root mean square (RMS) error between $\mathbf{E} \times \mathbf{B}$ and vertical drifts from SF and EOF models were 6.49 m/s and 1.59 m/s, respectively. SF model's results clearly show larger deviation from magnitude of $\mathbf{E} \times \mathbf{B}$ drift than vertical drifts estimated from
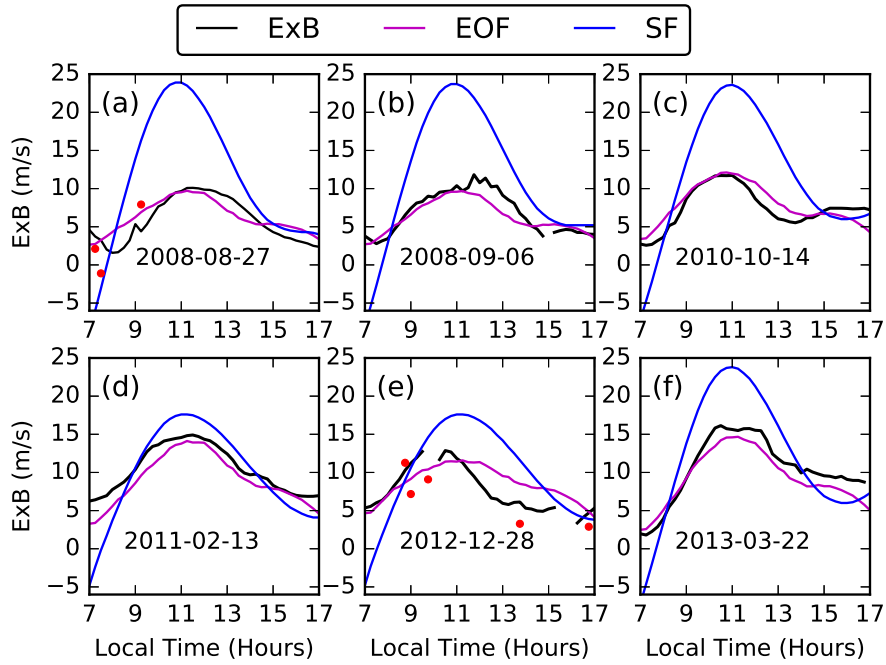
Figure 4.8: Comparisons of SF (blue curve) and EOF (magenta curve) models in estimating the quiet time vertical $\mathbf{E} \times \mathbf{B}$ drift (black curve). In-situ C/NOFS $\mathbf{E} \times \mathbf{B}$ drift observations are shown as red-dots.

EOF model. Figure 4.9 (a)-(b) shows scatter plot of Anderson $\mathbf{E} \times \mathbf{B}$ drift with vertical drifts estimated from EOF and SF models during quiet conditions. Computed correlation coefficient (R) values between Anderson $\mathbf{E} \times \mathbf{B}$ drift and $\mathbf{E} \times \mathbf{B}$ drift from SF and EOF models were 0.728 and 0.90, respectively. Available C/NOFS $\mathbf{E} \times \mathbf{B}$ are closer to Anderson $\mathbf{E} \times \mathbf{B}$ drift (and EOF modeled vertical drifts), than the vertical drifts from climatological SF model. From the limited dataset of 2008-08-27 and 2012-12-28, the R values between observed vertical drifts from C/NOFS and EOF model were 0.891 and 0.577, respectively. The calculated R values between $\mathbf{E} \times \mathbf{B}$ from C/NOFS and SF model were 0.887 and 0.268, for 2008-08-27 and 2008-12-28, respectively. Therefore, EOF model also performs better than SF when estimating the in-situ C/NOFS observations.

Over the African sector there are no previous local modelling efforts to compare our results with. But studies which uses time derivative of peak height of the F2 layer $(\frac{d}{dt}(h_m F2))$ (e.g., Oyekola and Kolawole, 2010; Adeniyi et al., 2014) and $\triangle H$ (e.g., Yizengaw et al., 2012) in the effort to estimate the vertical $\mathbf{E} \times \mathbf{B}$ drift are available. These works are mostly case studies, except the seasonal variability analysis that was presented in Yizengaw et al. (2014a). Figure 4.10 shows quiet time vertical $\mathbf{E} \times \mathbf{B}$ drift derived from ionosonde in the African longitude sector
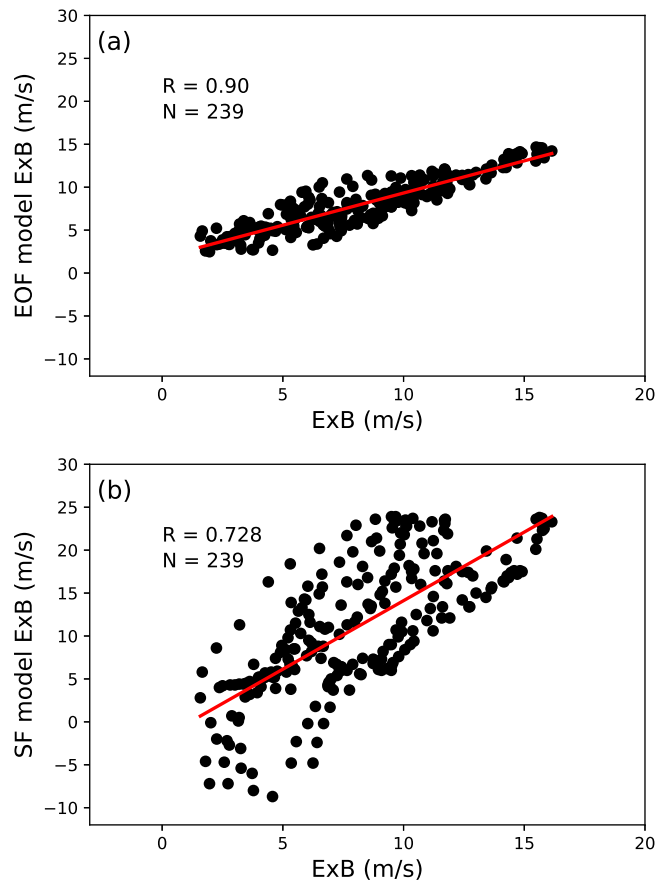
Figure 4.9: Scatter plots of (a) Anderson $\mathbf{E} \times \mathbf{B}$ drift versus EOF model results, and (b) model values (SF model) during quiet conditions
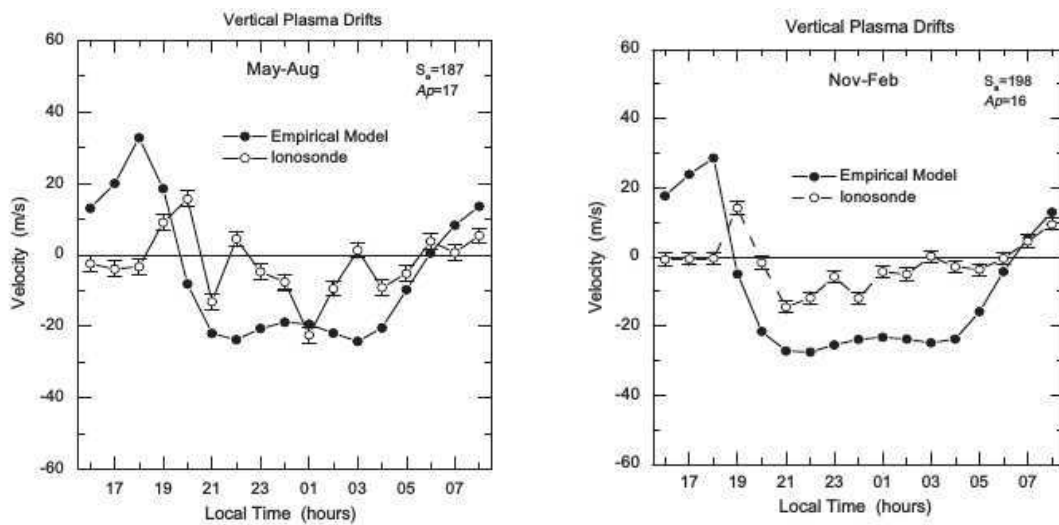

Figure 4.10: Comparison of vertical $\mathbf{E} \times \mathbf{B}$ drift in Africa (Ouagadougou, 12°N, 1.8°W, 15.9°W geomagnetic) and Scherliess-Fejer empirical model (Oyekola and Kolawole, 2010).

(Ouagadougou, 12°N, 1.8°W, 15.9°W geomagnetic) (Oyekola and Kolawole, 2010) using hourly monthly median values data for May-August (left) and November-February (right) in 1989. In Figure 4.10, the SF model (Scherliess and Fejer, 1999) was compared with ionosonde derived $\mathbf{E} \times \mathbf{B}$ drift and it was reported that the SF model values are overestimated and underestimated during daytime and nighttime, respectively.

4.4.3 Disturbed conditions

Lower panels of Figure 4.11(a)-(b) shows diurnal variation of $\mathbf{E} \times \mathbf{B}$ drift, and vertical drifts estimated from the SF and EOF models when $K_p > 3$. Days 2011-01-06 and 2013-09-18 had some missing data points for $\mathbf{E} \times \mathbf{B}$ drift. Variations of the geomagnetic indices (K_p and Dst) are included in top panels, (a) and (b), to show the strengths of geomagnetic activities for each period investigated.

Top panel of Figure 4.11 (a) shows that there was a minor storm which started during nighttime of 06 January 2011 and continued to the next day. Maximum K_p was 5 and Dst reached a minimum of -42 nT at 0600 UT on 07 January 2011. Top panel of Figure 4.11 (b) shows there was a minor storm with maximum K_p of 4, and the minimum Dst value reached was -19 nT at 0500 UT on 19 September 2013. Both storms of 06-08 January 2011 and 18-20 September 2013 recovered very slowly, a characteristic of corotating interactive region (CIR) storms (e.g. Miyoshi and Kataoka, 2005; Borovsky and Denton, 2006; Tsurutani et al., 2014) which normally occur during low solar activity periods. While Figure 4.11(a) shows that the minimum Dst and maximum K_p values were reached at a time not covered by our modelling results, it is known that CIR driven storms have long recovery phases during which the ionosphere could remain active. For-example, Chen et al. (2015) reported that during the recovery phase of CIR driven geomagnetic storms, positive electron density response in low latitudes can last for 2-4 days. Positive storm effects in low latitudes during storms were found to be associated with penetrating electric fields which are well known to cause increase in $\mathbf{E} \times \mathbf{B}$ drift during daytime in low latitudes (e.g., Fejer et al., 1979; Fejer, 1997). Considering the two storm periods, the calculated RMS error values were 4.57 m/s and 1.68 m/s between observed $\mathbf{E} \times \mathbf{B}$ and vertical drifts from the SF and EOF models, respectively.

Figure 4.12 (a)-(b) show scatter plots of vertical drifts from EOF and SF models against Anderson $\mathbf{E} \times \mathbf{B}$ drift during disturbed conditions ($K_p > 3$). The computed R values based on 81 data-points of $\mathbf{E} \times \mathbf{B}$ and vertical drifts from the SF and EOF models were 0.922 and 0.927,
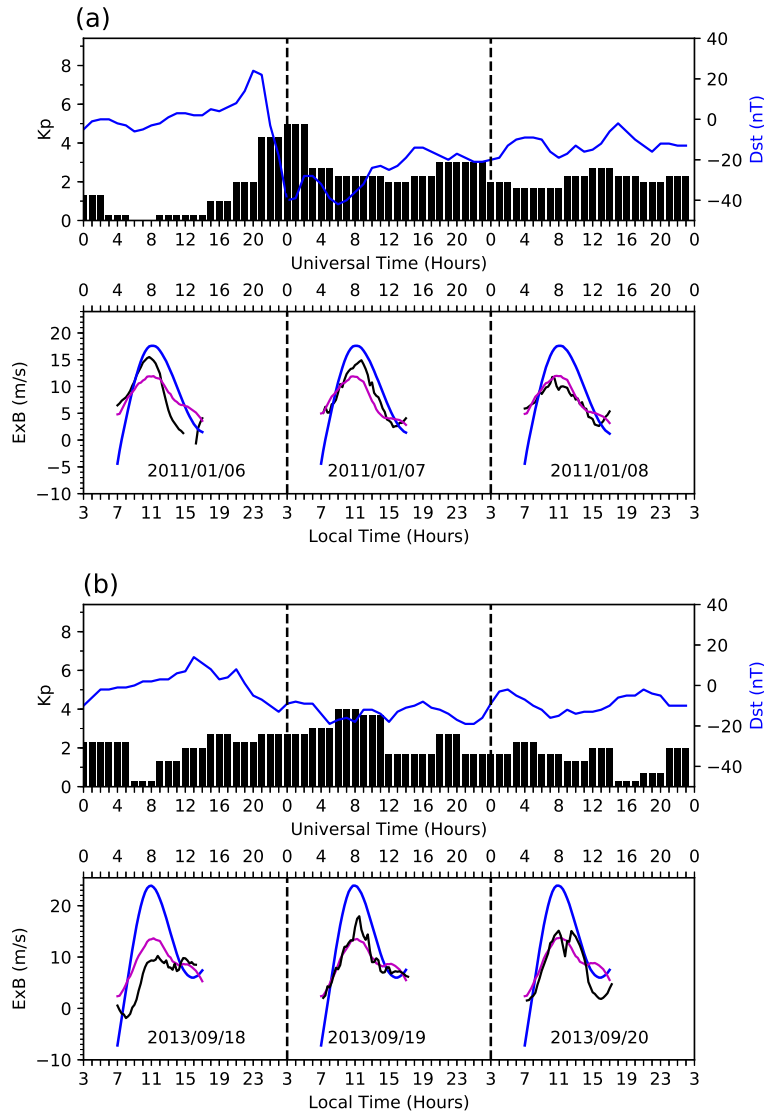
Figure 4.11: Lower panels: Diurnal variation of $\mathbf{E} \times \mathbf{B}$ drift (black) and vertical drifts estimated with EOF (magenta curve) and SF (blue curve) models, respectively, for $K_p > 3$. Top panels: Changes of K_p and Dst indices with time for the period indicated. The disturbed periods shown are for (a) 06-08 January 2011 and (b) 18-20 September 2013.

respectively. For both storm periods, the EOF emerges as a better empirical model. It should again be emphasized that the SF model is being compared with a dataset which is derived in the same way as the data used to develop the EOF model. Unfortunately, there was no available C/NOFS data to perform direct comparison with both SF and EOF models during the selected disturbed conditions.

Figure 4.12: Scatter plot of $\mathbf{E} \times \mathbf{B}$ drift versus EOF model results during disturbed days (07 Jan 2011 and 19 Sept 2013) (a), and with climatological model values (SF model) (b) during relatively disturbed conditions ($K_p > 3$)
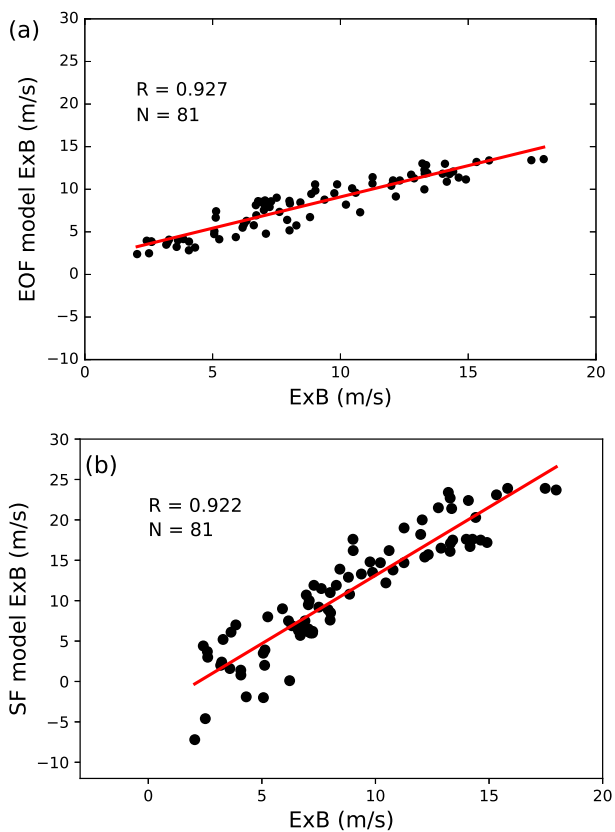
4.5 Summary

An empirical model for the African low latitude region of daytime vertical $\mathbf{E} \times \mathbf{B}$ drift, based on the EOF decomposition, is proposed here. Our estimation of $\mathbf{E} \times \mathbf{B}$ drift was based on EEJ determination using low latitude magnetometer data (e.g. Rastogi and Klobuchar, 1990; Anderson et al., 2002; Yizengaw et al., 2012), and the empirical formula developed by Anderson et al. (2004) which has been found to be applicable in the Peruvian, Philippine, Indian and African sectors (Anderson et al., 2006; Anghel et al., 2007; Yizengaw et al., 2012). A comparison between corresponding outputs and those measured shows that the technique is promising, also when compared with the climatological model. At the same time, we have also shown that the empirical formula introduced by Anderson et al. (2004) presents some problem for very low values of solar activity like those characterizing the passage between solar cycles 23 and 24, with a poor correlation between the $\mathbf{E} \times \mathbf{B}$ drift and the solar index F10.7.

Chapter 5

High resolution $\mathbf{E} \times \mathbf{B}$ drift models based on magnetometer and satellite observations

5.1 Introduction

In this chapter, high resolution empirical models based on partial least squares (PLS) and artificial neural networks (ANN) techniques are developed and used in the estimation of the vertical $\mathbf{E} \times \mathbf{B}$ drift over the African sector. In contrast to EOF model which is based on vertical $\mathbf{E} \times \mathbf{B}$ drift data at 15-minute intervals, PLS and ANN are considered high resolution models since they were developed from 1-minute data. Some of the results and description in this chapter are also presented in the paper by Dubazane and Habarulema (2017). While ANN have previously been used in modelling ionospheric vertical drifts in other longitudinal sectors (e.g., Anderson et al., 2004; Anghel et al., 2007), this chapter presents the first results where PLS and ANN techniques are being used in modelling vertical $\mathbf{E} \times \mathbf{B}$ drift over the African longitudinal sector. Due to a general lack of observations over the African sector, an expression relating C/NOFS vertical $\mathbf{E} \times \mathbf{B}$ drift and $\triangle H$ observations is developed during 2008–2013. Previously, Anderson et al. (2004) developed a third order polynomial function of $\triangle H$ to estimate $\mathbf{E} \times \mathbf{B}$ drift based on JULIA and magnetometer measurements. Very recently, Habarulema et al. (2017) investigated different functions relating C/NOFS vertical $\mathbf{E} \times \mathbf{B}$ drift and $\triangle H$ over Jicamarca (11.8°S, 77.2°W; 0.8°N geomagnetic) and validated the approaches with JULIA and ISR measurements from 2008–2014. The third order

polynomial function emerged as a better expression to derive vertical $\mathbf{E} \times \mathbf{B}$ drift from $\triangle H$ from quantitative relationship,

$$v_{Drift} = -1.872 + 0.399\triangle H - 0.0002\triangle H^2 - 6 \times 10^6 \triangle H^3,\tag{5.1}$$

This chapter presents the expression/equation (5.1) based on Habarulema et al. (2017) results relating C/NOFS $\mathbf{E} \times \mathbf{B}$ drift and $\triangle H$. Thereafter, the $\mathbf{E} \times \mathbf{B}$ drift values derived from our developed quantitative relationship are used as observations in the modelling process.

5.2 Magnetometer and $\mathbf{E} \times \mathbf{B}$ drift observations over Jicamarca

As mentioned earlier, studies of $\mathbf{E} \times \mathbf{B}$ drift started years ago over Jicamarca (e.g., Woodman and Hagfors, 1969). Over this longitude sector, there exists more instruments for providing vertical $\mathbf{E} \times \mathbf{B}$ drift measurements such as pair of low latitude magnetometers (for local daytime EEJ), Jicamarca's Incoherent Scatter Radar (ISR) (e.g., Woodman and Hagfors, 1969; Anderson et al., 2004; Stoneback et al., 2011). It is for this reason that Habarulema et al. (2017) chose to investigate the long-term estimation of C/NOFS vertical $\mathbf{E} \times \mathbf{B}$ drift velocities from magnetometer $\triangle H$ over Jicamarca so that it would be possible to validate the developed expression with actual data. In their analysis, linear, quadratic, third to fifth order polynomial functions were investigated and validated using ISR measurements during 2008–2014.

Figure 5.1 shows a scatter plot of vertical ionospheric drifts from ISR (red-dots) and JULIA (black-dots) and derived vertical $\mathbf{E} \times \mathbf{B}$ drift using the third order polynomial of $\triangle H$. The computed R values of 0.78 and 0.83 for ISR and JULIA, respectively, confirm the reliability of the quantitative relationship (equation (5.1)) developed by Habarulema et al. (2017). Diurnally, Figure 5.2 shows a comparison of the observed ISR and derived vertical $\mathbf{E} \times \mathbf{B}$ drift velocities for days (2014-04-23, 2014-05-06, 2014-11-26 and 2014-12-16) which were not covered during the derivation of the relationship.

Table 5.1 shows a summary of the correlation coefficient (R) and root mean square error $(RMSE)$ values obtained for different functions, showing that the third order polynomial yields high R and low $RMSE$ making it the most appropriate for estimating vertical $\mathbf{E} \times \mathbf{B}$ drift from $\triangle H$. Habarulema et al. (2017) stated that their expression was developed using data from September
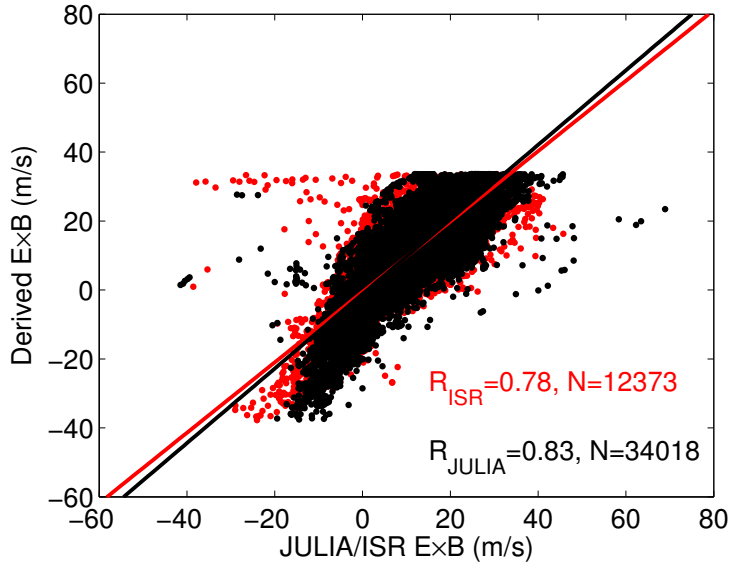
Figure 5.1: Scatter plots of vertical $\mathbf{E} \times \mathbf{B}$ drift, from the ISR (red-dots) and JULIA (black-dots) and derived $\mathbf{E} \times \mathbf{B}$ (m/s) derived from $\triangle H$ measurements (Habarulema et al., 2017).

Table 5.1: Correlation coefficient (R) and root mean square error $(RMSE)$ values between $\mathbf{E} \times \mathbf{B}$ drift estimated from the C/NOFS $\mathbf{E} \times \mathbf{B}$ drift-magnetometer $\triangle H$ relationship and ISR observations over Jicamarca for period 2008–2014 (Habarulema et al., 2017).

Function of $\triangle H$ for $\mathbf{E} \times \mathbf{B}$ estimation	R	$RMSE$ (m/s)
Linear	0.762	7.27
Quadratic	0.774	7.309
Cubic	0.777	7.134
Fourth order polynomial	0.774	7.198
Fifth order polynomial	0.756	7.437

2008 to March 2014 and results in Figure 5.2 indicate that the relationship achieves generalization. While there are some slight overestimations and underestimations, their results showed that the vertical ionospheric drift derived from third order polynomial of $\triangle H$ agrees well with vertical $\mathbf{E} \times \mathbf{B}$ drift observations from ISR. Based on these results, the third order polynomial function was adopted in deriving the quantitative relationship between C/NOFS $\mathbf{E} \times \mathbf{B}$ drift and $\triangle H$ over the African longitude sector. It is however noted that Anderson et al. (2004) used the same order of polynomial in estimating JULIA $\mathbf{E} \times \mathbf{B}$ drift from $\triangle H$ over Jicamarca during 2001–2003.
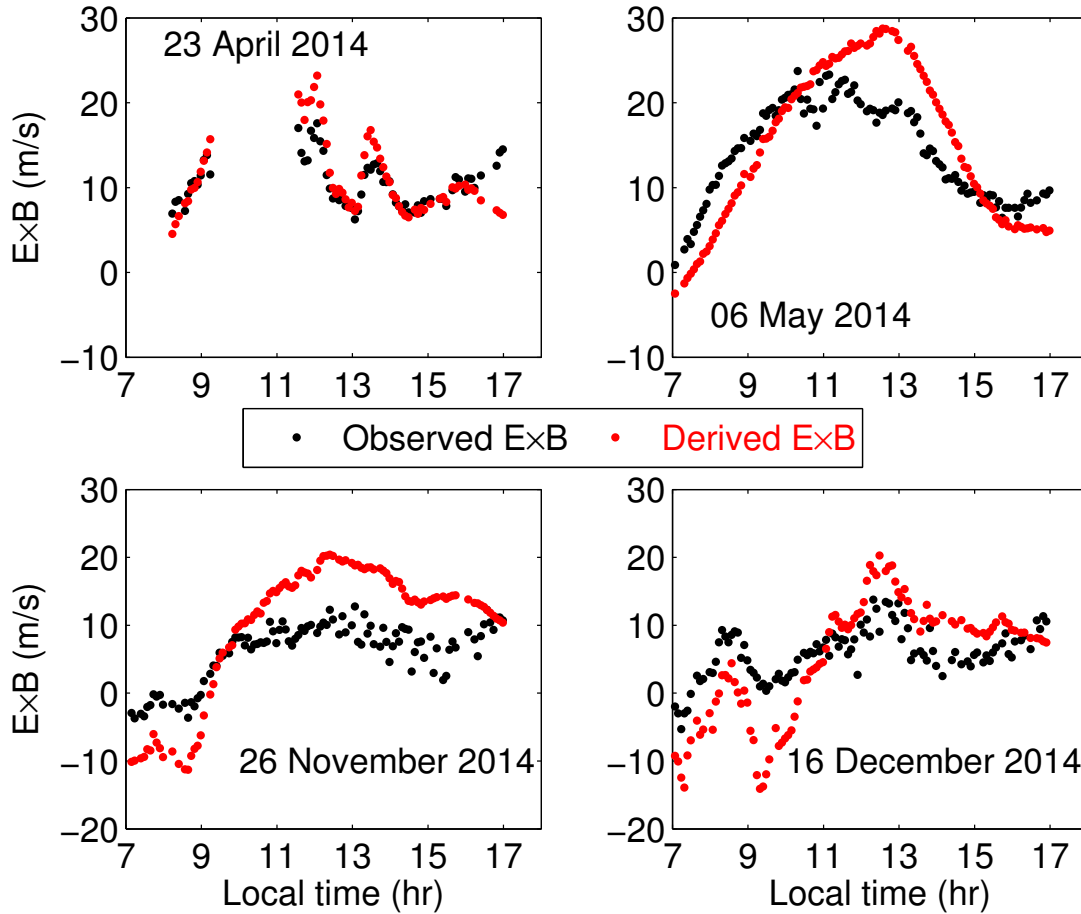
Figure 5.2: Comparison of ISR observed and derived $\mathbf{E} \times \mathbf{B}$ (m/s) for randomly selected days in 2014 where measured data exists. Observed and derived $\mathbf{E} \times \mathbf{B}$ (m/s) are plotted in black and red dots respectively (Habarulema et al., 2017).

5.3 Relationship between $\triangle H$ and C/NOFS vertical drift over the African sector

As mentioned in Chapter 3 (section 3.2.1) and Chapter 4, the difference of horizontal component of geomagnetic field ($\triangle H$) were derived from magnetic field data using Addis Ababa, AAE (9.0°N, 38.8°E; 0.18°N geomagnetic) and Adigrat, ETHI (14.3°N, 39.5°E; 6.0°N geomagnetic) stations. The IVM sensor on-board C/NOFS satellite was a source of vertical $\mathbf{E} \times \mathbf{B}$ drift (Stoneback et al., 2011; Rodrigues et al., 2011) as described in section 3.2.2. The development of the expression is limited to 2008–2013 when the two magnetometer stations were simultaneously operational to

allow for the estimation of EEJ. During the period of this research, publicly available C/NOFS data was from 2008–2014.
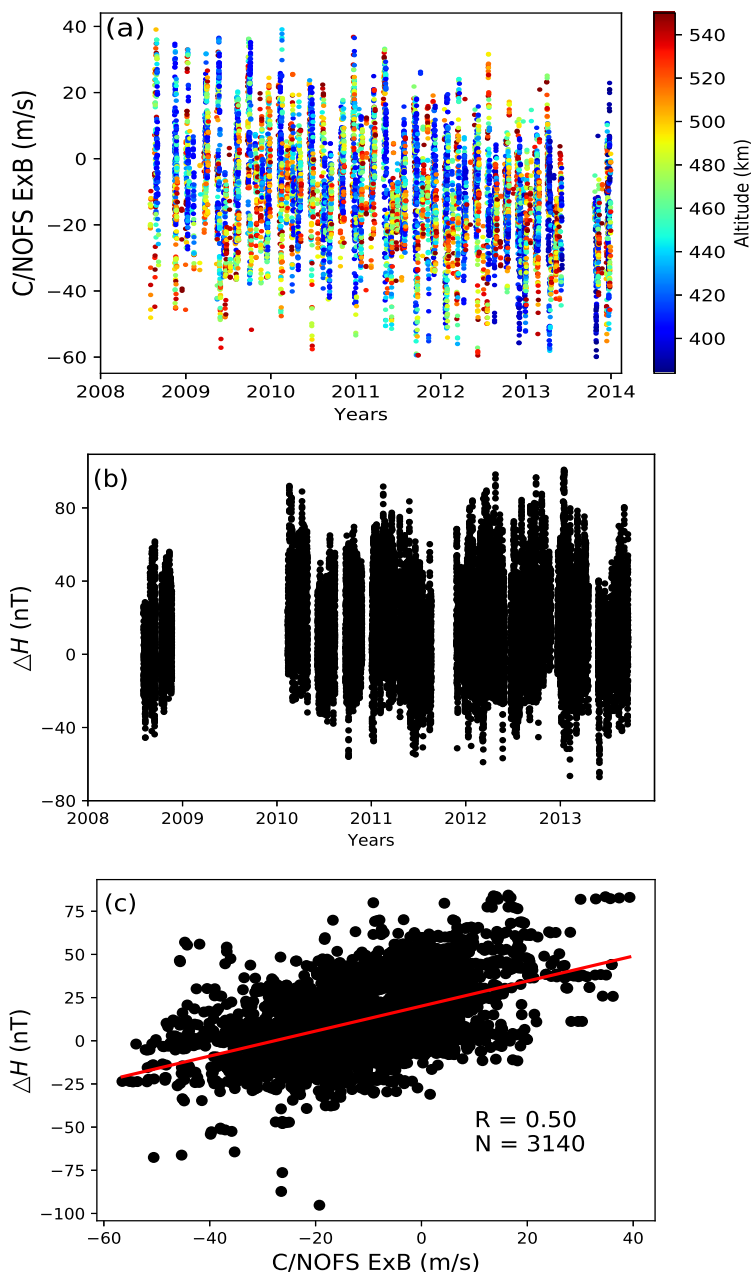
Figure 5.3: (a) Distribution of C/NOFS $\mathbf{E} \times \mathbf{B}$ observations over AAE (0.18°N ±8° geomagnetic, 38.8°E ±3.5°), (b) daytime $\triangle H$ measurements used in the period of study (2008–2013) , (c) comparison of the variability of daytime magnetic field perturbation ($\triangle H$) and C/NOFS $\mathbf{E} \times \mathbf{B}$ at 1-minute intervals.

Figure 5.3 (a)-(b) shows the distribution of C/NOFS $\mathbf{E} \times \mathbf{B}$ drift and $\triangle H$ dataset used in the effort to investigate their quantitative relationship. It can be seen that these datasets do not always

occur at similar times. The relationship is developed based on dataset for a period 2008–2013 (excluding 2009 where $\triangle H$ measurements are missing). C/NOFS observations are not uniformly distributed in the period investigated with data mostly missing in 2008 and in the second half of 2013. Also a significant amount of $\triangle H$ data are missing in 2008, 2011 and 2013, in addition to the gap for the whole 2009. Figure 5.3 (c) shows a scatter plot of local daytime $\triangle H$ and C/NOFS $\mathbf{E} \times \mathbf{B}$ values taken at one-minute intervals (when both datasets were available) from where a mathematical relationship between the two sets of data was deduced. Longitudinal variations of vertical $\mathbf{E} \times \mathbf{B}$ drift are taken at 38.8±11.2 to avoid large local time difference in observations, while C/NOFS observations within ±4 degrees geomagnetic latitude from the geomagnetic equator are based on the fact that the EEJ is a narrow strip of enhanced current within ±3° from the dip equator. C/NOFS $\mathbf{E} \times \mathbf{B}$ observations within altitude range (400–500 km) have been used in other investigations (e.g., Stoneback et al., 2011; Yizengaw et al., 2014a; Rodrigues et al., 2015).

The correlation coefficient (R) value of 0.50 was computed based on $N=3140$ data-points of C/NOFS $\mathbf{E} \times \mathbf{B}$ and $\triangle H$. Although this R value seems to be low, other studies have reported comparable results using satellite and magnetometer observations. For example, recently using $\mathbf{E} \times \mathbf{B}$ drift from Republic of China Satellite 1 (ROCSAT-1) and EEJ (from ground-magnetometer data) over the Indian and Japanese sectors during solar maximum period (2001–2003), Kumar et al. (2016) showed R values of $\approx$ 0.61 and 0.56 over the Indian and Japanese sectors, respectively. They attributed the low R values to altitude difference since ROCSAT-1 provides $\mathbf{E} \times \mathbf{B}$ at 600 km, while EEJ is a narrow band of current flowing at lower altitude within the E region ($\approx$ 105 km). Figure 5.4 shows seasonal variation of ionospheric vertical drifts from ISR and JULIA at different altitudes (Hui, 2015).

Investigations of quiet time $\mathbf{E} \times \mathbf{B}$ drift variability has shown that the bimonthly vertical ionospheric drifts change linearly with altitude, it can be often increasing and decreasing during morning and afternoon hours (Hui, 2015). From Figure 5.4, large bimonthly averaged vertical $\mathbf{E} \times \mathbf{B}$ drift velocities were observed in March–April and September–October. Largest averaged upward vertical $\mathbf{E} \times \mathbf{B}$ drift was seen in September–October (Hui, 2015). The differences in altitudes is one of the major reasons for the low correlation between C/NOFS $\mathbf{E} \times \mathbf{B}$ and $\triangle H$ due to the different physical mechanisms at different heights (e.g., Heelis et al., 1974; Rishbeth, 1997). Nevertheless, using C/NOFS and $\triangle H$ data that gave R value of 0.57 over Jicamarca, Habarulema et al. (2017), showed that it was still possible to estimate ISR vertical $\mathbf{E} \times \mathbf{B}$ drift
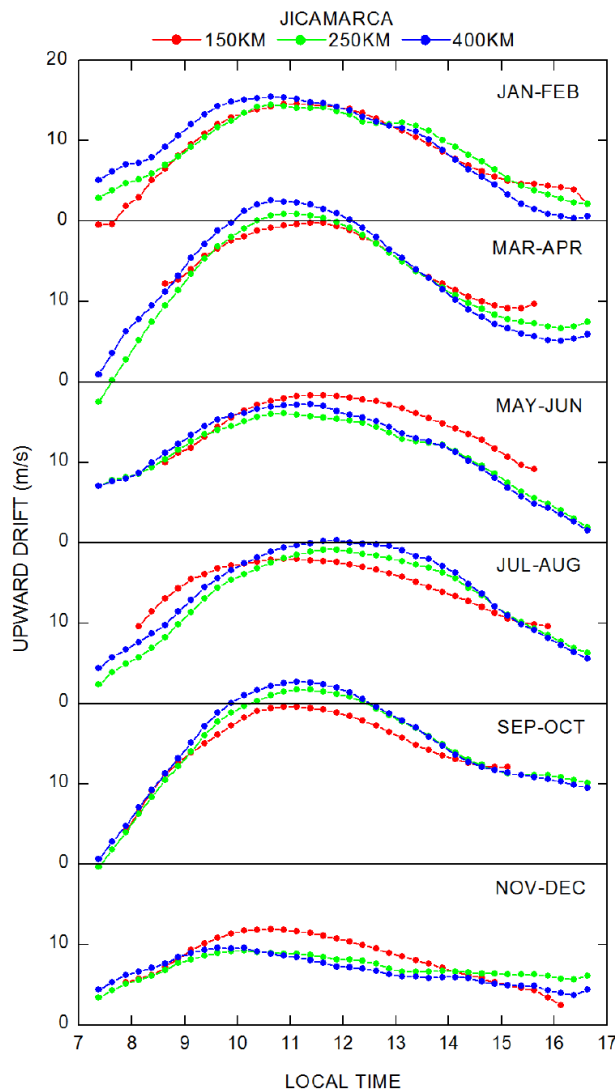
Figure 5.4: Bimonthly averaged seasonal variations of vertical $\mathbf{E} \times \mathbf{B}$ drift measured at different altitudes (Hui, 2015).

from $\triangle H$. Kumar et al. (2016) reported low R values of ≈ 0.60 and 0.52 between $\mathbf{E} \times \mathbf{B}$ and $\triangle H$ during quiet conditions ($K_p < 3$) over Indian and Japanese sectors, respectively. While we have not performed the study based on different geomagnetic activity levels, the R value of 0.50 obtained in our study is consistent/comparable with reported results (Kumar et al., 2016) and suggests that C/NOFS $\mathbf{E} \times \mathbf{B}$ drift and $\triangle H$ may be driven by different processes which depend on altitude. Neutral winds at both E and F regions potentially lead to vertical $\mathbf{E} \times \mathbf{B}$ drift. However, the effect of winds at the different altitudes also depends on the strength of the Pedersen and Hall conductivity at different local times (e.g., Fambitakoye et al., 1976; Crain et al., 1993; Fang et al., 2008; Maute et al., 2012). In the E-region, the Hall conductivity is dominant, while the Pedersen

conductivity governs F region dynamo. Winds in the low altitude correlates positively with $\triangle H$, while westward winds in the high altitudes generates an upward/poleward electric polarization field which governs eastward currents around magnetic equator (Fang et al., 2008). Based on simulated results, Maute et al. (2012) concluded that only winds below about 200 km are contributing in the upward vertical $\mathbf{E} \times \mathbf{B}$ drift.

Using dataset shown in Figure 5.3 (c), a relationship between the C/NOFS $\mathbf{E} \times \mathbf{B}$ drift and $\triangle H$ observations (at 1-minute interval) was developed based on the similar procedure in Anderson et al. (2004) and Habarulema et al. (2017), yielding the following expression

$$v_{drift} = -14.726 + 0.3098\triangle H + 0.0005\triangle H^2 + 0.0000032\triangle H^3, \tag{5.2}$$

where v_{drift} is the estimated vertical $\mathbf{E} \times \mathbf{B}$. Equation (5.2) was developed based on C/NOFS observations and hence it contains less data than the overall $\triangle H$ data available. However $\triangle H$ data is completely missing during 2009, hence this dataset is not included in the development of the quantitative relationship. The expression in equation (5.2) was used to derive $\mathbf{E} \times \mathbf{B}$ drift values from the entire $\triangle H$ dataset during 2008–2013. Figure 5.5 (a) shows a sample of $\mathbf{E} \times \mathbf{B}$ drift results extracted at 15-minutes intervals plotted with solar flux index ($F_{10.7}$), while Figure 5.5 (b) shows scatter plot of $\mathbf{E} \times \mathbf{B}$ drift derived from our relationship and equation (1) in Anderson et al. (2004). High R value of ≈ 0.99 was calculated based on N=30 996 data-points of $\mathbf{E} \times \mathbf{B}$ values (with a resolution of 15-minute intervals). Therefore, these quantitative relationships compare well with each other, although our equation (5.2) gives larger negative $\mathbf{E} \times \mathbf{B}$ values. Large negative $\mathbf{E} \times \mathbf{B}$ values from equation (5.2) could be due to the magnitudes of C/NOFS observations which have an average $\approx$ -10 m/s over the entire period of study. Based on Thermosphere-Ionosphere-Electrodynamics General Circulation Model (TIE-GCM) simulation, Fang et al. (2008) observed the negative intercept in a linear relationship between $\mathbf{E} \times \mathbf{B}$ and $\triangle H$ datasets and the physical meaning was centered on the EEJ and off-equatorial wind-driven current system at different altitudes. However, large negative values of $\triangle H$ can also be seen in Figure 5.3 (b)–(c) and may be attributed to reversal of EEJ current mainly during quiet conditions. The reversal of EEJ during daytime is known as counter-electrojet (CEJ) and is more common during low solar activity periods (Rastogi, 1974; Patil et al., 1990). It was realized by Mayaud (1977) that during most magnetically quiet conditions, CEJ events were from minimum solstice months. Daytime $\triangle H$ measurements consists of $\approx$ 40% of total observations within this period of study which are most quiet ($K_p \leq 2$) and some have large negative values at different local times. This number

rises to $\approx 72\%$ when considering $K_p \leq 3$ as a criterion for selecting quiet periods. Therefore, large depression of $\triangle H$ (CEJ signatures) are also expected to contribute to negative $\mathbf{E} \times \mathbf{B}$ values derived from equation (5.2). Solar semi-diurnal tidal modes were reported by Alex and Mukherjee (2001) to be source of CEJ over Addis Ababa, AAE (9.0°N, 38.8°E geographic) and Trivandrum, TRD (8.5°N, 77.0°E geographic) for the period 1991–1993. They reported that the varying amplitude of semi-diurnal tides influence the local time distribution of CEJ. Alex and Mukherjee (2001) observed CEJ during morning (0600–0800 LT), noon (1100–1200 LT), afternoon (1300–1400 LT) and evening (1500–1800 LT).
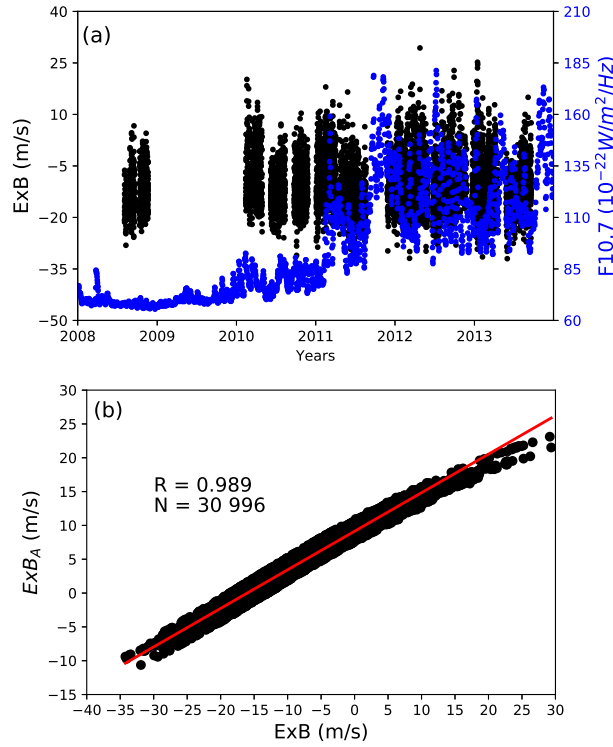
Figure 5.5: (a) Long-term variability of $\mathbf{E} \times \mathbf{B}$ drift derived from our relationship and $F10.7$ index for 2008-2013, (b) scatter plot of $\mathbf{E} \times \mathbf{B}$ values derived from our relationship and equation (1) in Anderson et al. (2004) denoted as $\mathbf{E} \times \mathbf{B}_A$, respectively.

Recently, geomagnetic field data recorded in 2009 (mean annual sunspot number $R_z = 3.1$) over South American, Philippine and African sectors were used by Rabiu et al. (2017) to investigate longitudinal variation of EEJ and CEJ during quiet conditions ($K_p \leq 3$). Their results revealed larger occurrence of CEJ over the African sector; AAE and Ilorin (8.50°N, 4.68°E) which dominated during morning and evening periods. CEJ occurrence during morning and afternoon hours over the western Africa longitudinal sectors was reported as seasonal effect (Doumouya et al., 1998).

74

Our period of study included one of the anomalous and prolonged solar minimum conditions that were extremely quiet (e.g., Ezquer et al., 2014; Perna and Pezzopane, 2016) and as a result the variability analyses relating ionospheric and solar activity behavior were very complicated (e.g., Chen et al., 2011; Solomon et al., 2013). From Figure 5.5 (a) it can be observed that there is some correlation between $F_{10.7}$ and ionospheric vertical drifts, although the investigated period have a significant amount of missing $\mathbf{E} \times \mathbf{B}$ drift data. Previously, a correlation coefficient of 0.53 between EEJ and $F_{10.7}$ datasets for a period 1996–2005 in the east Asian region was reported (Yamazaki et al., 2010) based on quiet condition ($K_p \leq 2^+$). Hamid et al. (2013) used EEJ and $F_{10.7}$ datasets in 2011 and revealed a 5-day and 7-day peaks when performing the auto-correlation of EEJ, and they suggested that modulation of the EEJ by variations from lower atmosphere could have resulted in lower correlation with $F_{10.7}$ index. Due to a close relationship between EEJ and vertical $\mathbf{E} \times \mathbf{B}$ drift, waves from lower atmosphere may contribute to the low correlation observed between the derived $\mathbf{E} \times \mathbf{B}$ drift and $F_{10.7}$ index during some periods shown in Figure 5.5(a). Using the derived vertical $\mathbf{E} \times \mathbf{B}$ drift values (with equation (5.2)), $\mathbf{E} \times \mathbf{B}$ drift models have been developed based on PLS and ANN approaches with relevant physical/geophysical inputs described in the next section.

5.4 Modelling Inputs

Different physical/geophysical input parameters which potentially influence vertical $\mathbf{E} \times \mathbf{B}$ drift were investigated before developing vertical drift models. Thus diurnal and seasonal variations (including geomagnetic activity) of $\mathbf{E} \times \mathbf{B}$ drift were considered during modeling.

5.4.1 Diurnal variations

Observations have shown that daytime vertical $\mathbf{E} \times \mathbf{B}$ drift peaks at local noon and is a minimum at sunrise and sunset (e.g., Farley et al., 1986; Haile, 2003; Adebesin et al., 2013). Post-sunset upward plasma drift (pre-reversal enhancements) is seasonal and solar cycle dependent (e.g., Fejer et al., 1991; Vichare et al., 2012; Adebesin et al., 2013) and thereafter the vertical $\mathbf{E} \times \mathbf{B}$ drift is directed downwards. EEJ which is a basis of our investigation is a local time phenomenon and hence short term temporal $\mathbf{E} \times \mathbf{B}$ drift changes can be represented by local time, t. To ensure data continuity between consecutive days t was decomposed into cyclic components (Poole and McKinnell, 2000),

$$tc = cos\left(\frac{2\pi t}{24}\right), \quad ts = sin\left(\frac{2\pi t}{24}\right) \tag{5.3}$$

where tc and ts refer to cosine and sine components of the t, respectively.

5.4.2 Seasonal variations

Vertical $\mathbf{E} \times \mathbf{B}$ drift largely shows annual variations where it peaks during equinox and is minimum at solstice (e.g., Woodman et al., 1977; Fejer et al., 1979; Yamazaki et al., 2010). Characterization of EEJ revealed annual variations, however semi-annual variations have been reported predominant (e.g., Stening, 1995; Yamazaki et al., 2009, 2010). Figure 5.6 shows variation of EEJ (and therefore $\mathbf{E} \times \mathbf{B}$ drift due to their close relationship) in the eastern Asian region with day of the year (d) for the period 1996–2005 during quiet condition ($K_p \leq 2^+$).
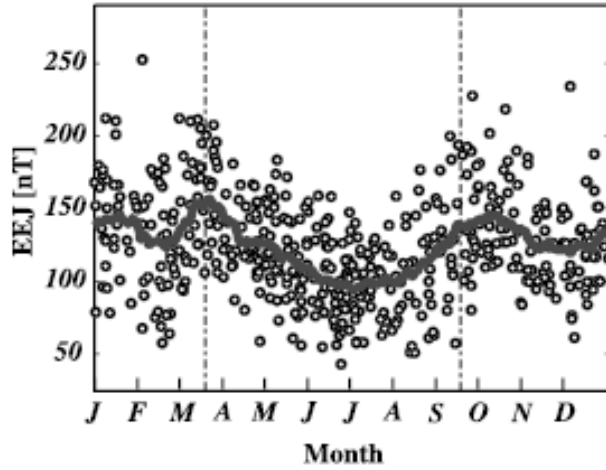
Figure 5.6: Variation of EEJ at Davao station (7.0°N, 125.4°E) as a function of the day number. The solid gray-line refers to 30–day–centered moving average of the data. The vertical dashed lines indicate the equinoxes (Yamazaki et al., 2010).

Annual and semi-annual periodic structure of the $\mathbf{E} \times \mathbf{B}$ drift can be represented by Fourier series of day of the year (e.g., Alken, 2009) as shown below,

$$dc_a = cos\left(\frac{2\pi d}{365.25}\right), \quad ds_a = sin\left(\frac{2\pi d}{365.25}\right) \tag{5.4}$$

$$dc_s = cos\left(\frac{4\pi d}{365.25}\right), \quad ds_s = sin\left(\frac{4\pi d}{365.25}\right) \tag{5.5}$$

where dc_a and ds_a are cosine and sine components of day of the year (d) capturing annual -variations, while dc_s and ds_s represent cosine and sine components of d for semi-annual variations. A factor of 0.25 was added in 365 days of the year to account for leap years.

From Figure 5.6, it is clear that EEJ has a predominant semi-annual variation in accordance with the work by Stening (1995). Yamazaki et al. (2010) suggested that the observed semi-annual variations are associated with geometric effects as they cause semi-annual changes of solar ionization and heating of the ionosphere at equatorial latitudes.

5.4.3 Geomagnetic activity

Magnetospheric electric fields during intense geomagnetic storms could partially penetrate to the low latitude ionosphere as prompt penetration electric field (PPEF) thereby modifying electrodynamics (e.g., Fejer and Scherliess, 1995). If the B_z component of IMF is southward, the resultant electric field is eastward (westward) during daytime (nighttime), respectively. This additional eastward field enhances the magnitude of daytime vertical $\mathbf{E} \times \mathbf{B}$ drift causing significant changes in ionospheric density structure which could be felt even at midlatitude ionosphere (e.g., Nishida, 1968). Other phenomena of geomagnetic activities such as ionospheric disturbance dynamo could cause westward current (reducing the normal daytime eastward EEJ) and thus downward vertical $\mathbf{E} \times \mathbf{B}$ drift during daytime (e.g., Nishida, 1968; Blanc and Richmond, 1980), in low latitude ionosphere. Figure 5.7 shows the correlation between changes in $\triangle H$ (and therefore $\mathbf{E} \times \mathbf{B}$ drift), and Bz component of the interplanetary magnetic field (IMF Bz) and interplanetary electric field (IEF) for 09 August 2008 (Yizengaw et al., 2011b). The $\triangle H$ and vertical $\mathbf{E} \times \mathbf{B}$ drift data are over AAE, African sector. They reported reduction in the $\triangle H$ during daytime and therefore CEJ signatures. Yizengaw et al. (2011b) noticed a complete reversal of $\triangle H$ around 0730–0840 UT when IMF B_z turns north for a short duration, thus leading to westward zonal electric field and CEJ as suggested in (e.g., Kikuchi et al., 2000).

Disturbance storm time (Dst) and symmetric H-component (SYM-H) indices measure storm time ring currents (Sugiura, 1963; Scherliess and Fejer, 1997; Wanliss and Showalter, 2006). In our modeling, we used the SYM-H index due to its high time resolution and ability to show fast changes in equatorial ring current during storms. Equatorial electric field during active geomagnetic conditions were reported to depend on the history and present geomagnetic activity levels (e.g., Scherliess and Fejer, 1997; Yamazaki and Kosch, 2015). Therefore, the history of geomag-
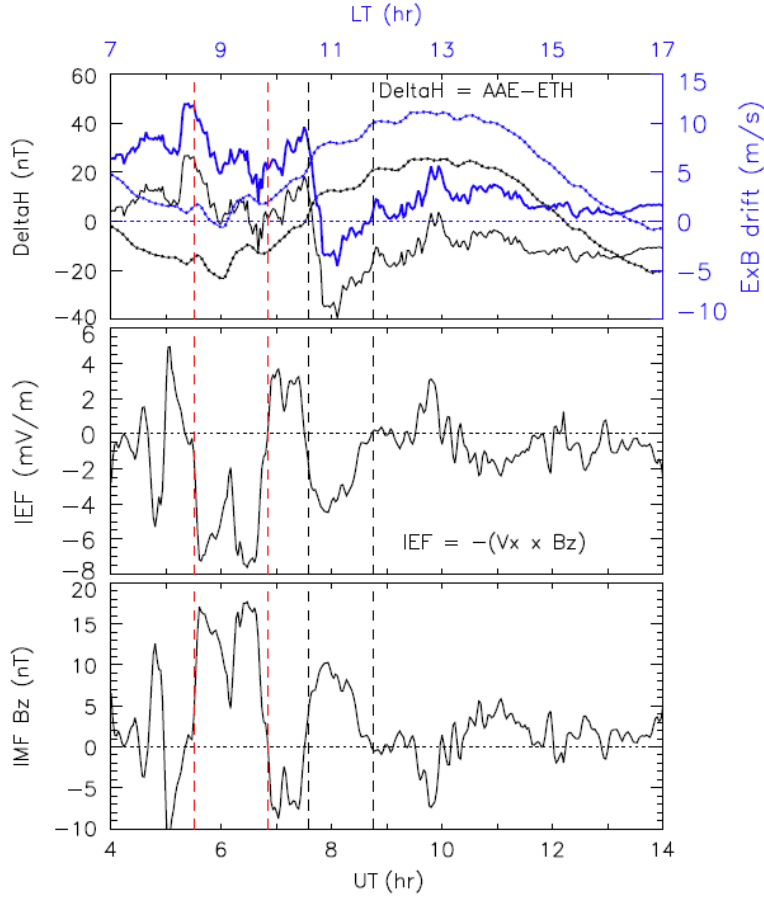
Figure 5.7: (Top panel) Variation of $\triangle H$ (solid black curve) obtained from magnetometer data near dip equator (AAE) and off the equator (ETHI) used in the estimation of vertical $\mathbf{E} \times \mathbf{B}$ drift (solid blue curve). The dashed-dotted curves are H variations after baseline correction for AAE (blue) and ETHI (black). The middle and bottom panels show the interplanetary electric field (IEF) and Bz component of interplanetary magnetic field (IMF Bz) on 09 August 2008 (middle panel) solar wind electric field estimated from ACE data, and (bottom panel) IMF B_z orientation (Yizengaw et al., 2011b).

netic activity level is represented in modeling as a rate of change of SYM-H ($\frac{d}{dt}$(SYM-H)). Other geomagnetic indices include Auroral Electrojet (AE) which measures geomagnetic activities in the auroral region (Davis and Sugiura, 1966) and K_p (Bartels, 1963) index that provides a general measure of geomagnetic activity level using magnetic field observations of the mid and high latitudes.

5.4.4 Solar activity

Solar flux index $F_{10.7}$ is a proxy of Extreme Ultraviolet radiation (EUV) released by the Sun (e.g., Hinteregger, 1976; Warren et al., 1998). The EUV ionizes neutral atoms in the Earth's atmosphere and thus different amounts of electrons and ions exist at different layers of the atmosphere. Post sunset upward $\mathbf{E} \times \mathbf{B}$ drift observations from Jicamarca were reported to significantly change with $F_{10.7}$ than daytime drifts (e.g., Fejer et al., 1991). Vichare et al. (2012) confirmed these findings using observations in the Philippine sector at 120°E longitude. E-region ionospheric conductivity σ and peak electron density $N_m E$ change throughout the day and they are roughly related to the solar flux index $F_{10.7}$ (e.g., Richmond, 1973) as follows,

$$EEJ \propto \sigma \mathbf{E} \propto N_m E \propto F_{10.7} + \text{other factors} \tag{5.6}$$

where $\mathbf{E}$ is the eastward electric field. With exception of the extended solar minimum (2008–2010), Figure 5.5 shows that the derived $\mathbf{E} \times \mathbf{B}$ drift approximately has a linear relationship with solar flux index $F10.7$ and hence the latter was used as a modelling input.

5.5 Selection of inputs for modelling $\mathbf{E} \times \mathbf{B}$ drift

A total of 15 combinations were developed using linear regression (also known as LS) to quantify the influence of each parameter on $\mathbf{E} \times \mathbf{B}$ drift. The combinations (LS1–LS15) use different sets of inputs shown in Table 5.2. LS is a well-known statistical learning technique (Pearson, 1896) that has been previously used in estimating EEJ and daytime $\mathbf{E} \times \mathbf{B}$ (e.g., Anderson et al., 2004; Stolle et al., 2008; Alken, 2009; Yamazaki et al., 2010). Vertical $\mathbf{E} \times \mathbf{B}$ drift data inferred from pair AAE-ETHI from 2008-2013 (except 2009) were divided into modeling and validation datasets. Four quiet ($K_p \leq 3$) days in each year, and four disturbed ($K_p > 3$) periods in years (2008, 2010, 2011, and 2012) were reserved for validation. The combinations are developed based on 1-minute datasets, however for presentation purposes $\mathbf{E} \times \mathbf{B}$ drift datasets taken at 3-minute intervals were used in validating the models. This is possible since these datasets (3-minute intervals) were not averaged, merely taken at every 3-minute intervals. Figure 5.8 shows the performance of 15–combinations of input parameters investigated in the effort to estimate the vertical $\mathbf{E} \times \mathbf{B}$ drift. Performance of each combination was evaluated based on the validation dataset described above and compared statistically using root mean square error ($RMSE$) and correlation coefficient R.
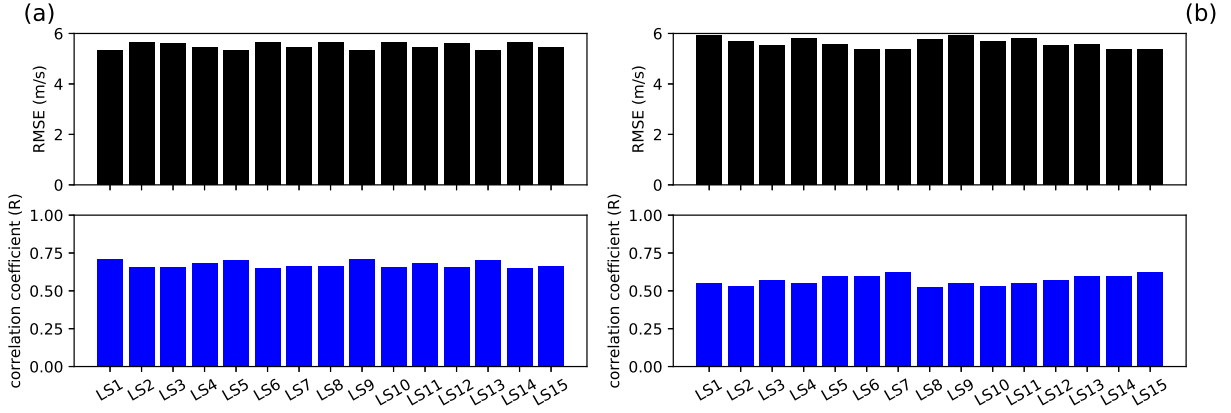
Figure 5.8: A statistical comparison of LS models of quiet time (a) and storm (b) $\mathbf{E} \times \mathbf{B}$ drift using $RMSE$ and R.

A better model is described by lower $RMSE$ calculated using,

$$RMSE = \sqrt{\frac{1}{N} \sum_{i=1}^{N} \left(\mathbf{E} \times \mathbf{B}_{mod} - \mathbf{E} \times \mathbf{B}_{obs}\right)^2} \qquad (5.7)$$

where $\mathbf{E} \times \mathbf{B}_{mod}$ and $\mathbf{E} \times \mathbf{B}_{obs}$ are modeled and observed $\mathbf{E} \times \mathbf{B}$ values, respectively.

From Figure 5.8 (a) it is clear that combinations LS1, LS4, LS5, LS7, LS9, LS11, LS13 and LS15 models have comparable $RMSE$ and R values during quiet conditions. Figure 5.8 (b) which represents the performance of the models during disturbed condition ($K_p > 3$), clearly shows that LS7 and LS15 are better combinations with comparable R and $RMSE$ values. LS7 and LS15 showed identical R and $RMSE$ values of ≈ 0.62 and 5.35 m/s. Based on statistical analysis and physical importance of each investigated input, LS15 was chosen as an ideal/representative combination. The LS quantitative relationship of $\mathbf{E} \times \mathbf{B}$ drift from model set of inputs described by LS15 is as follows,

$$
\begin{aligned}
v_{lm} =\ & -22.790 + 1.275 dc_a + 0.3275 ds_a - 1.9420 dc_s + 0.1111 ds_s \\
& -11.680 tc + 0.8074 ts + 0.05703 \text{SYM-H} + 0.04488 F_{10.7} + 0.1934 \frac{d}{dt}(\text{SYM-H})
\end{aligned}
$$

$$(5.8)$$

where v_{lm} is a plasma drift velocity estimated using least-squares (LS) model.

Before proceeding with the final model development, we investigated the Gaussian-like functions Gt_μ of local time to describe the diurnal variation of EEJ and therefore $\mathbf{E} \times \mathbf{B}$ drift

Table 5.2: Parameters used to develop different LS models of $\mathbf{E} \times \mathbf{B}$ drift.

Model	Input combinations
LS1	t, d
LS2	$t, F10.7$
LS3	$t, \text{SYM-H}$
LS4	$t, d, F10.7$
LS5	$t, d, \text{SYM-H}$
LS6	$t, F10.7, \text{SYM-H}$
LS7	$t, d, F10.7, \text{SYM-H}$
LS8	$t, \frac{d}{dt}(\text{SYM-H})$
LS9	$t, d, \frac{d}{dt}(\text{SYM-H})$
LS10	$t, F10.7, \frac{d}{dt}(\text{SYM-H})$
LS11	$t, d, F10.7, \frac{d}{dt}(\text{SYM-H})$
LS12	$t, \text{SYM-H}, \frac{d}{dt}(\text{SYM-H})$
LS13	$t, d, \text{SYM-H}, \frac{d}{dt}(\text{SYM-H})$
LS14	$t, F10.7, \text{SYM-H}, \frac{d}{dt}(\text{SYM-H})$
LS15	$t, d, F10.7, \text{SYM-H}, \frac{d}{dt}(\text{SYM-H})$

(Doumouya et al., 2003),

$$Gt_\mu = exp\left(-\frac{t - \mu}{w_0}\right) \tag{5.9}$$

where μ (= 10, 11, 12, and 13) is a parameter which represents occurrence of peak values of EEJ (and thus $\mathbf{E} \times \mathbf{B}$ drift) at different local times with respect to different days and seasons, w_0 is the fitting parameter governing the time window of the Gaussian-like functions (e.g., Haile, 2003; Doumouya et al., 2003). This parameter is data-driven and it was determined by trial and error; where $w_0 = 1$hour was used in our analysis. Figure 5.9 shows the diurnal variation of $\triangle H$ (EEJ) taken from observations in the period 2008–2013 at different years and seasons to illustrate different local time occurrence of day-to-day peak EEJ.

From Figure 5.9, it can be seen that peak $\triangle H$ occurs at different local times for such different periods. Settings with either one or more combinations of Gt_μ centered at different local times defined by parameter $\mu = 10, 11, 12,$ and 13 were investigated and the input space with all μ values (10, 11, 12, and 13) was found to have an effect on improving $\mathbf{E} \times \mathbf{B}$ results.

Using the same validation dataset, the resulting setting (re-formulated LS15) was performing better ($RMSE \approx 6.22$ m/s and $R \approx 0.72$) than the one based on cyclic components local time ($RMSE \approx 7.02$ m/s and $R \approx 0.58$). Hence, the Gt_μ centered at $\mu = 10, 11, 12,$ and 13 along with other inputs were used to develop the functions estimating $\mathbf{E} \times \mathbf{B}$ drift. Subsequently, the artificial neural network (ANN) and partial least squares (PLS) models were developed using Gaussian functions of t, centered at $\mu = 10, 11, 12,$ and 13 which replaced cyclic components of local time.
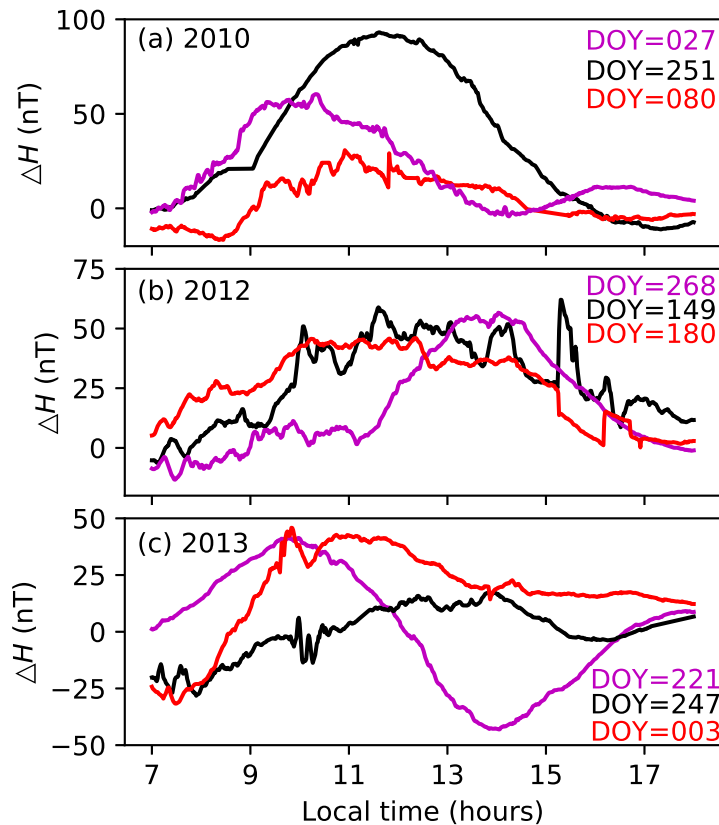
Figure 5.9: The diurnal variation of the $\triangle H$ illustrating seasonal dependence and day-to-day occurrence of peak EEJ at different local times for some days during the period 2008–2013.

5.6 Developing high resolution models

5.6.1 PLS technique

Regression based on PLS technique was used to model the vertical $\mathbf{E} \times \mathbf{B}$ drift velocities derived from $\triangle H$ measurements during the period 2008–2013. For a number of predictors which could be correlated, it is possible to over-fit a PLS model during the development. In this work, 10-fold cross-validation was used to test the significance of each PLS component (Höskuldsson, 1988; Wold et al., 1993). In cross-validation the data, $\mathbf{X}$ and $\mathbf{Y}$, is split into a number of blocks, M, and a one orthogonal vector model is built from remaining (M-1) blocks of data. Based on this one orthogonal vector model, the excluded block of data is used for testing and an individual PRedicted Error of Sum of Squares ($PRESS$),

$$PRESS_1 = \sum_i^{10} |y_i - \hat{y}_i|^2, \tag{5.10}$$

82

is calculated for one orthogonal vector, where y_i and $\hat{y}_i$ are the actual and predicted response of the $i-$th excluded block of data. The procedure is repeated, excluding each block of data once, and then the total of $PRESS$ values corresponding to respective 10-blocks of excluded data is calculated for one orthogonal vector by summing the individual PRESS values. $PRESS$ estimates the predictive ability of the model. Figure 5.10 shows a procedure of cross-validation based on $PRESS$ for choosing optimal number of latent/orthogonal vectors (Geladi and Kowalski, 1986).

$$PRESS = \sum_{l=1}^{p}\sum_{i=1}^{k}(y_{li} - \hat{y}_{li})^2\,, \tag{5.11}$$

where y_{li} and $\hat{y}_{li}$ are the actual and predicted response of excluded block of data for each l orthogonal vector. The procedure is repeated for each orthogonal vector ($l = 2, 3, 4, ..., p$) until $PRESS$ reaches a minimum value.
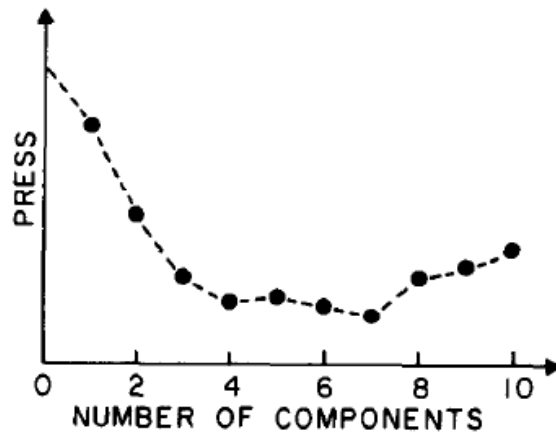
Figure 5.10: Schematic illustrating the cross-validation process of choosing the optimal PLS components (orthogonal/latent vectors) using $PRESS$ (Geladi and Kowalski, 1986).

Therefore, optimal number of orthogonal vectors which are PLS components are taken around minimum $PRESS$ value (Stone, 1974; Wold, 1978; Geladi and Kowalski, 1986). From Figure 5.10, it is clear that $PRESS$ reached a minimum value near the PLS component of 7, hence similar procedure was used in our study. It should be emphasized that the cross-validation above was performed to train/optimize the PLS model. From a set of 11-inputs described in section 5.4 and 5.5, the estimated ionospheric vertical drift $\hat{\mathbf{Y}}$ was calculated from seven orthogonal components,

$$\hat{\mathbf{Y}} = \sum_{i=1}^{7} \mathbf{t}_i \mathbf{b}_i \quad \text{where,} \quad \mathbf{b}_i = \mathbf{u}_i^T \mathbf{t}_i (\mathbf{t}_i^T \mathbf{t}_i)^{-1} \tag{5.12}$$

83

For each set of orthogonal vectors ($\mathbf{t}_i$ and $\mathbf{u}_i$), $\mathbf{b}_i$ represents a set of coefficients associated with each input parameter as described in details in Chapter 3, section 3.3.2. The resulting relationship between ionospheric vertical drift and the inputs considered was obtained as,

$$
\begin{aligned}
v_{pls} \;=\; & -18.090 + 8.410Gt_{10} + 3.937Gt_{11} + 4.705Gt_{12} + 3.182Gt_{13} + 1.297dc_a + 0.3225ds_a \\
& -1.942dc_s + 0.09268ds_s + 0.05754\text{SYM-H} + 0.04536F_{10.7} + 0.1856\frac{d}{dt}(\text{SYM-H})
\end{aligned}
$$

$$(5.13)$$

where v_{pls} is the $\mathbf{E} \times \mathbf{B}$ drift estimated from the PLS technique. PLS was discovered in the field of econometrics by Wold et al. (1966). It neglects the fundamental assumption of linear regression where a response is estimated from independent variables and no collinearity. We have used PLS modeling approach based on Non-linear Iterative Partial Least Squares (NIPALS) described in section 3.3.2.1. This work presents the PLS technique in the ionospheric studies for the first time.

5.6.2   ANN technique

Estimation of vertical $\mathbf{E} \times \mathbf{B}$ drift has also been performed with ANN, since it has the ability to learn underlying rules and therefore attractive over traditional classification and regression techniques (e.g., Rumelhart and Mcclelland, 1986; Fausett, 1994). Back-propagation algorithm has been used due to its popular supervised procedure of updating connection weights in multi-layered neural network (Rumelhart and Mcclelland, 1986; Le Cun et al., 1988).

A set of 11-inputs described in section 5.4 and 5.5 and $\mathbf{E} \times \mathbf{B}$ drift values were used in the development of the neural network. Large fraction of dataset was used for training (90%), while the remaining data was used for validation or optimization (5%) and testing (5%) the performance of the resulting ANN model. For neural network training, the Levenberg-Marquardt back-propagation algorithm was used due to its fast and stable convergence (Levenberg, 1944; Marquardt, 1963). Number of neurons for hidden layers of a neural network were determined statistically using the $RMSE$ between observed and predicted $\mathbf{E} \times \mathbf{B}$ drift values. Figure 5.11 (a) shows a schematic illustration of the neural network setup, where L_1, L_2, L_3 are sets of neurons defining the input, hidden and output layers, respectively. Figure 5.11 (b) shows $RMSE$ values between the observed and predicted $\mathbf{E} \times \mathbf{B}$ drift values when the number of neurons in the hidden layer (L_2) were varied from 11-20. From Figure 5.11, the left pointed arrow in the direction where errors are propagation backward from output layer for updating the connection weights, while right pointed arrow refers
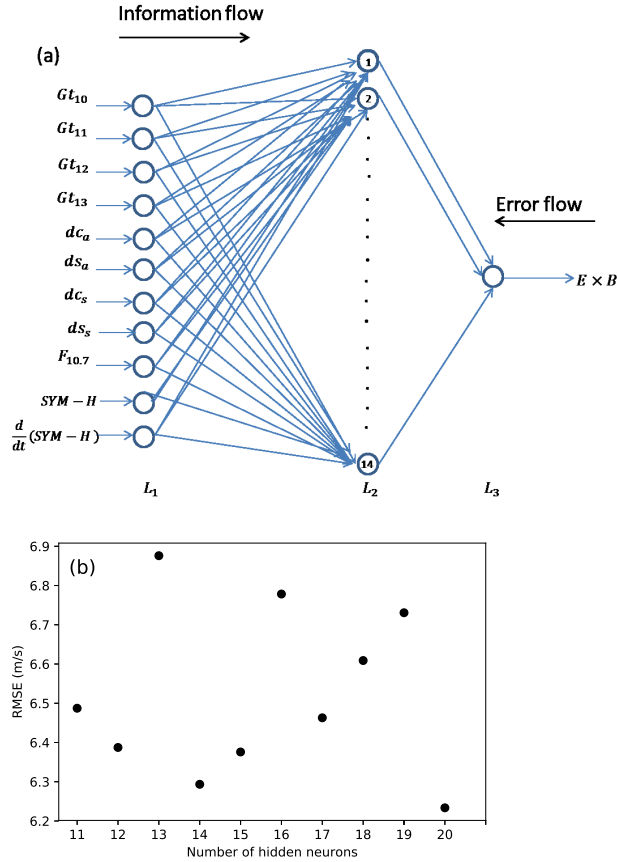
Figure 5.11: (a) Schematic showing architecture of feed-forward artificial neural network, (b) variation of $RMSE$ computed from predicted and observed $\mathbf{E} \times \mathbf{B}$ drift values (for all validation dataset) when the number of neurons in a hidden layer varies from 11-20.

to information fed into the network for the learning process. Low $RMSE$ values of ≈ 6.29 m/s and 6.23 m/s were seen when 14 and 20 neurons were used, respectively. However, for artificial neural network (ANN) model generalization 14-neurons were used for the neural network architecture.

Since the ANN can reveal most underlying complex relationships governing a process, it has also been used in ionospheric studies, for example, in the modeling of vertical $\mathbf{E} \times \mathbf{B}$ drift (e.g., Anderson et al., 2004; Anghel et al., 2007; Joshi and Sripathi, 2016) and other ionospheric parameters (e.g., Uwamahoro and Habarulema, 2015; Altinay et al., 1997; Cander, 2015). Cander (2015) modeled $f_\circ F2$ and $MUF(3000)F2$, and the resulting model gave RMS values of around 0.4 MHz between the actual observations and modeled results. Cander (2015) model was good considering the period of study, 6–10 February 1986 characterized by a minimum value of the Dst index equal to 307 nT. Anderson et al. (2004) estimated vertical $\mathbf{E} \times \mathbf{B}$ drift from JULIA using $\triangle H$ as the input. They achieved $RMSE$ value of ~ 4.0 m/s when comparing the observations with ANN

modeled results.

5.7   RESULTS AND DISCUSSION

In this section, both measured and modeled results are presented at 3-minute intervals during local daytime (07:00-18:00 LT) for the sake of limiting the size of graphics for a thesis. For quiet ($K_p \leq 3$) conditions, four days in each year were selected for validating the ANN and PLS models, while four storm periods for each year (except 2013 and 2009) were reserved for validation during disturbed ($K_p > 3$) conditions. Model validation was therefore performed on independent dataset that was not used in developing it. An attempt was also made to compare the ANN and PLS modeled values with corresponding $\mathbf{E} \times \mathbf{B}$ drift values from Scherliess-Fejer (SF) model (Scherliess and Fejer, 1997, 1999). Where possible C/NOFS vertical $\mathbf{E} \times \mathbf{B}$ drift observations were used as independent validation source.

5.7.1   Quiet conditions

Figure 5.12 shows the diurnal variations of the $\mathbf{E} \times \mathbf{B}$ drift during quiet ($K_p \leq 3$) conditions for selected periods. Vertical $\mathbf{E} \times \mathbf{B}$ drift is shown as black curve, while ANN and PLS modeled values are represented as green and blue curves, respectively.

When validating with the quiet conditions $\mathbf{E} \times \mathbf{B}$ dataset (Figure 5.12), the $RMSE$ values of 5.27 m/s and 6.00 m/s were calculated for the ANN and PLS modeled results, respectively. Our models were also compared with the Scherliess-Fejer model (hereafter, SF model) (Scherliess and Fejer, 1999) and the available C/NOFS $\mathbf{E} \times \mathbf{B}$ drift observations (plotted as red dots) in Figure 5.12. Few data-points (N=28) of vertical $\mathbf{E} \times \mathbf{B}$ drift velocities from C/NOFS satellite were compared with those estimated by ANN and PLS models. $RMSE$ values of 19.93 m/s and 19.51 m/s were computed for ANN and PLS models, respectively.

In comparison with results in Anderson et al. (2004), our models showed larger $RMSE$ values. However, it should be noted that Anderson et al. (2004) used radar and geomagnetic field ($\triangle H$) data to perform the modeling, while our model utilized satellite and geomagnetic field ($\triangle H$) datasets.

Figure 5.13(a) shows scatter plots of measured and ANN modeled vertical $\mathbf{E} \times \mathbf{B}$ drift for selected quiet periods ($K_p \leq 3$), shown in Figure 5.12. A correlation coefficient value of 0.810
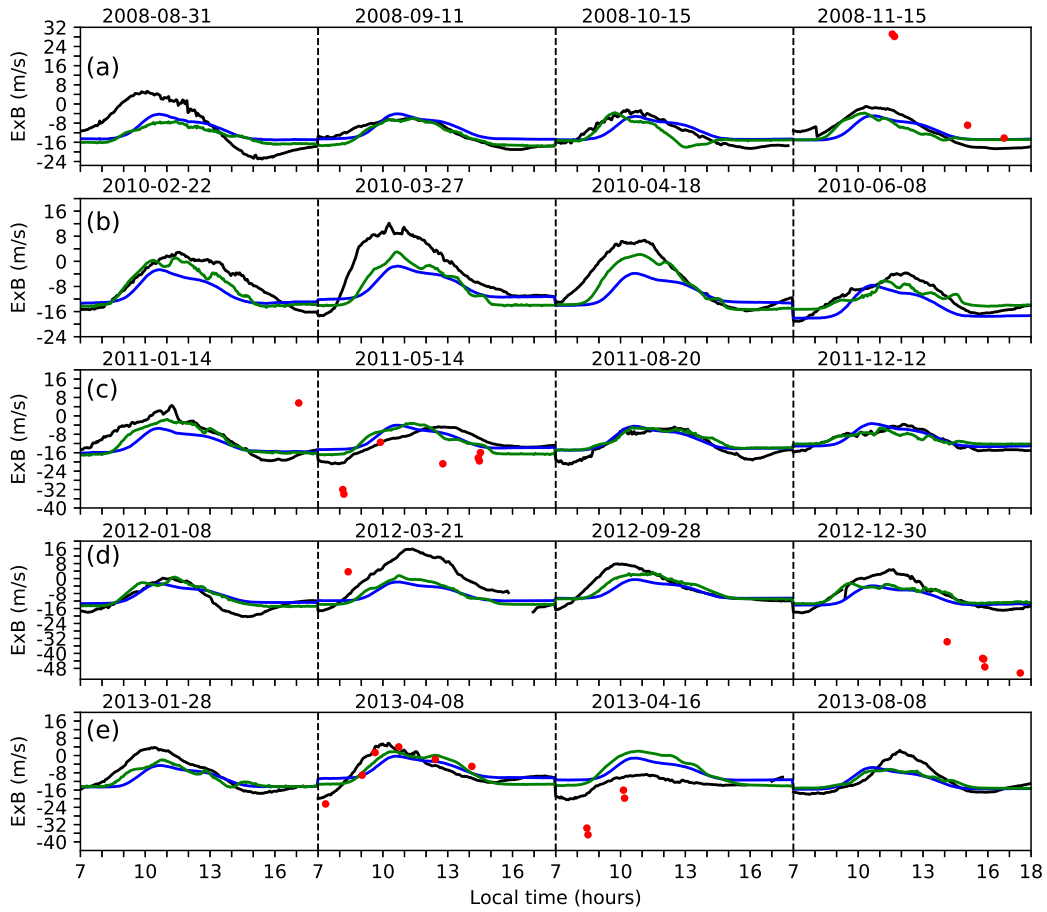
Figure 5.12: Comparisons of PLS (blue) and ANN (green) models' results in estimating the quiet time $\mathbf{E} \times \mathbf{B}$ drift (black). In-situ C/NOFS $\mathbf{E} \times \mathbf{B}$ drift observations are shown as red-dots.
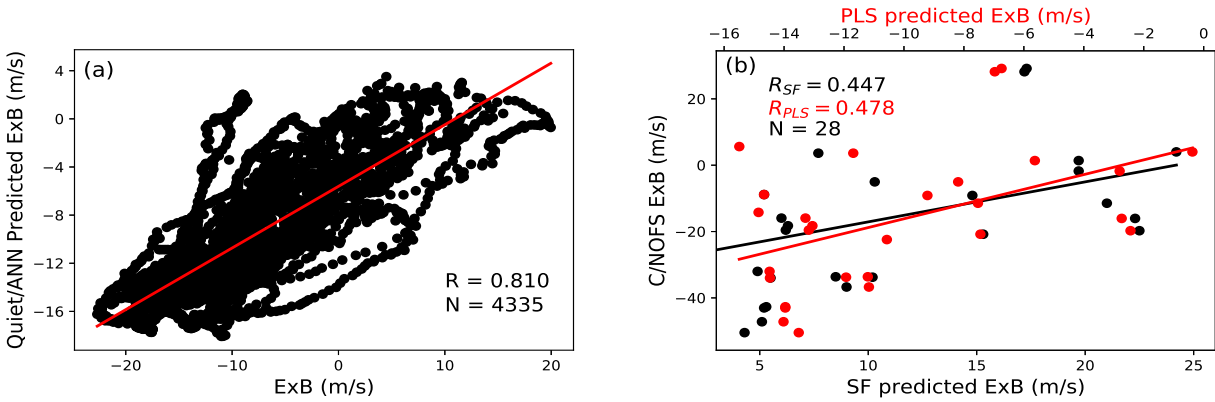
Figure 5.13: (a) Scatter plots of ANN modeled results with derived $\mathbf{E} \times \mathbf{B}$, (b) C/NOFS $\mathbf{E} \times \mathbf{B}$ drift and estimated results from SF (black dots) and PLS (red dots) models for quiet conditions. R and N represent the correlation coefficient and number of observations used.

Figure 5.14: Scatter of C/NOFS $\mathbf{E} \times \mathbf{B}$ drift and modeled results from (a) SF (black), and PLS (blue) models (b) SF and ANN (green) models during quiet conditions ($K_p <= 3$) in 2009.

based on 4335 data-points was computed based on ANN. Using the same dataset of vertical $\mathbf{E} \times \mathbf{B}$ drift in Figure 5.12, the PLS modeled results gave R values of 0.761. Despite slightly large $RMSE$ v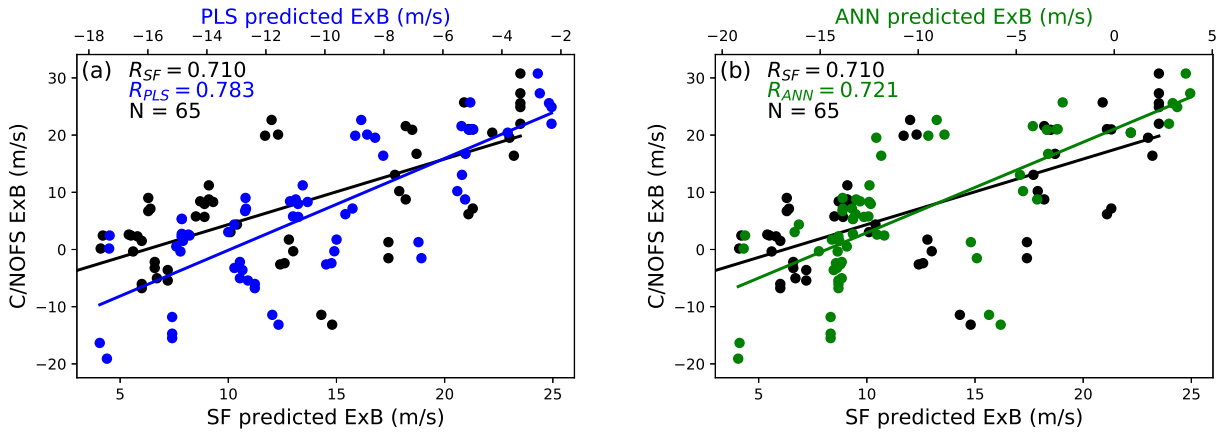alues, the ANN and PLS models showed high R values (0.810 and 0.761) when estimating the magnetometer-derived $\mathbf{E} \times \mathbf{B}$ drift observations. Figure 5.13(b) shows a scatter plot of C/NOFS vertical $\mathbf{E} \times \mathbf{B}$ drift velocities (shown as red-dots in Figure 5.12) and modeled values from PLS and SF models. When quiet times C/NOFS $\mathbf{E} \times \mathbf{B}$ drift plotted in Figure 5.13 (b) are estimated with SF and PLS models, R values of 0.447 and 0.478 were calculated based on N=28 data-points.

The correlation coefficient value of 0.46 was also calculated for the ANN model based on the same C/NOFS $\mathbf{E} \times \mathbf{B}$ drift observations. Similarly, the calculated $RMSE$ values for SF, PLS and ANN models were 29.42 m/s, 17.26 m/s and 17.32 m/s, respectively. These results demonstrate that the developed PLS and ANN models provide closer values to C/NOFS $\mathbf{E} \times \mathbf{B}$ drift velocities than the climatological SF model.

Figure 5.14 shows the performance of ANN (green dots and line of best fit), SF (black dots and line of best fit) and PLS (blue dots and line of best fit) models when validated on randomly chosen quiet days in 2009 where $\triangle H$ measurements are missing. Although the data may not be enough to conclude on the performance of both models, the calculated R values between C/NOFS $\mathbf{E} \times \mathbf{B}$ and modeled values (N=65) were ~ 0.78, 0.72, and 0.71 for the PLS, ANN and SF models, respectively. PLS model has clearly shown larger R values than other models when C/NOFS $\mathbf{E} \times \mathbf{B}$ drift were used in validation process. Figure 5.15 shows the diurnal variation of C/NOFS $\mathbf{E} \times \mathbf{B}$ drift observations (shown in Figure 5.14) estimated from ANN, PLS and SF models. Based
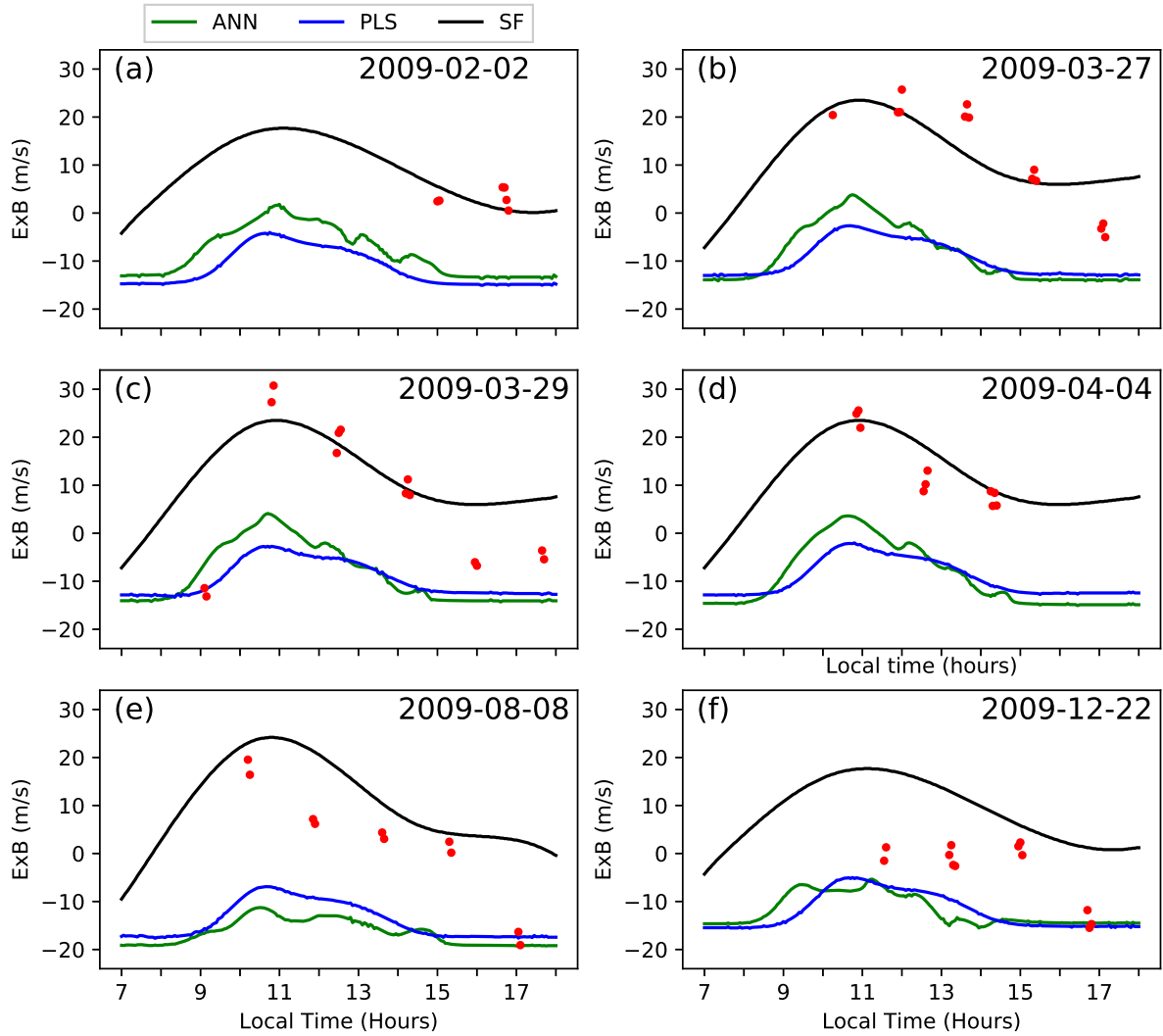
Figure 5.15: Comparison of C/NOFS $\mathbf{E} \times \mathbf{B}$ drift velocities (red dots) with values of ionospheric vertical drifts (at 3-minute intervals) estimated from ANN (green) and PLS (blue) during quiet conditions ($K_p <= 3$) in 2009.

on the limited C/NOFS $\mathbf{E} \times \mathbf{B}$ dataset in Figure 5.15, the calculated $RMSE$ values were 18.77 m/s, 18.61 m/sand 10.01 m/s for PLS, ANN and SF models, respectively, showing that the SF model is better in this case. Reliable long-term data is required to comprehensively validate these modelling approaches. Despite the obtained large $RMSE$ values in comparisons with earlier studies (Alken, 2009; Patra et al., 2014), our correlation coefficient values based on few data-points are comparable. However, due to very limited C/NOFS observations, it is difficult to make final conclusions on the performance of our developed models. Patra et al. (2014) validated the SF model's results during quiet conditions with C/NOFS observations (in January, June, July

and December 2009) over Kototabang (10.36°S magnetic latitude, Indonesia) and Gadanki (6.5°N magnetic latitude, India) and they found correlation coefficient values of 0.66 and 0.67 (when using 170 and 179 data points), respectively. A similar analysis using radar observations gave correlation coefficient values of $R = 0.59$ and $R = 0.51$ based on 207 and 407 observations over Kototabang and Gadanki, respectively (Patra et al., 2014). The correlation coefficient of about 0.50 was also reported when validating JVDM with $\mathbf{E} \times \mathbf{B}$ drift observations from JULIA (Alken, 2009). The PLS and ANN models perform better on estimating the vertical ionospheric drifts derived from magnetometer compared with those from C/NOFS satellite. While the ANN model was better in estimating magnetometer-derived $\mathbf{E} \times \mathbf{B}$ drift, PLS performs better when estimating C/NOFS $\mathbf{E} \times \mathbf{B}$ based on few data-points. A maximum R value of ~ 0.78, was obtained for the PLS method when compared with C/NOFS $\mathbf{E} \times \mathbf{B}$ drift observations.

5.7.2   Disturbed conditions

Figure 5.16 (a)-(d) shows diurnal variation of $\mathbf{E} \times \mathbf{B}$ drift and modeled values during disturbed $(K_p > 3)$ conditions. The onset and duration of disturbed periods are shown using the variation of Dst and K_p indices. During storm conditions the $RMSE$ values of 9.64 m/s and 10.82 m/s were calculated from 4-periods of $\mathbf{E} \times \mathbf{B}$ observations in Figure 5.16 (a)-(d), using ANN and PLS models' results, respectively.

Table 5.3: Performance of the ANN, PLS and SF models during disturbed conditions.

Event	$RMSE_{PLS}$(m/s)	R_{PLS}	$RMSE_{ANN}$(m/s)	R_{ANN}
03-05 Sept-2008	4.08	0.871	4.31	0.803
11-13 April 2010	3.48	0.740	7.11	0.725
28 Feb-02 Mar 2011	5.47	0.922	4.88	0.901
24-26 Jan 2012	16.70	0.841	14.26	0.890

The models' performance degrade during disturbed conditions. Table 5.3 shows the $RMSE$ and R values calculated for each storm period indicated in Figure 5.16 (a)-(d).

In comparison with PLS results, lower $RMSE$ values were obtained between the observed and ANN modeled $\mathbf{E} \times \mathbf{B}$ drift values during both quiet and disturbed conditions suggesting that ANN is slightly a better model. Comparison of the PLS and ANN results with limited C/NOFS
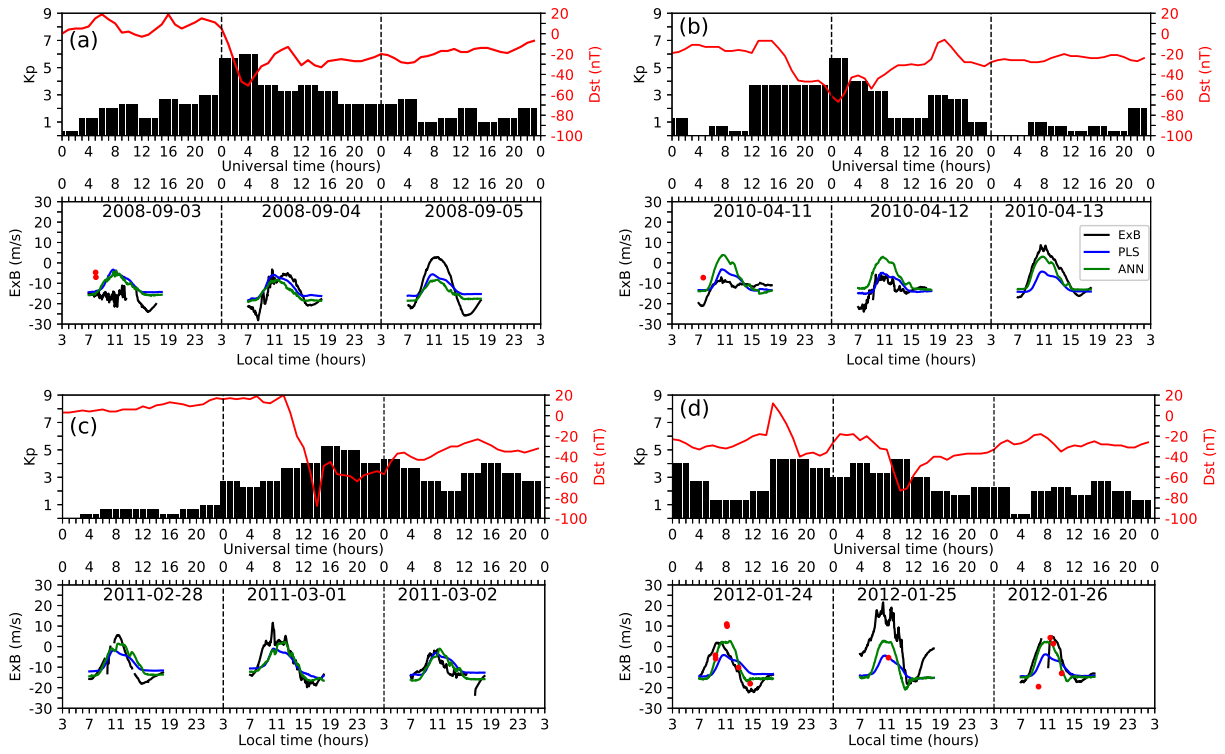
Figure 5.16: Comparison of $\mathbf{E} \times \mathbf{B}$ drift velocities with values estimated from ANN (green) and PLS (blue) during storm conditions of (a) 03-05 Sept 2008, (b) 11-13 April 2010, (c) 28 Feb-02 March 2011 and (d) 24-26 Jan 2012. Intensities of the storms are shown by K_p and Dst indices. The C/NOFS $\mathbf{E} \times \mathbf{B}$ observations (red dots) are also shown.

$\mathbf{E} \times \mathbf{B}$ drift in Figure 5.16 gave $RMSE$ values of 11.10 m/s and 10.10 m/s, respectively. Although different data-points were used in these statistical analyses, the deviation of the models from either C/NOFS $\mathbf{E} \times \mathbf{B}$ drift or magnetometer derived $\mathbf{E} \times \mathbf{B}$ drift is almost the same. The SF model gave large $RMSE$ value of 22.16 m/s when validated with the same C/NOFS $\mathbf{E} \times \mathbf{B}$ drift observations. Figure 5.17 shows scatter plots of measured and ANN modeled vertical $\mathbf{E} \times \mathbf{B}$ drift for selected disturbed periods ($K_p > 3$) within 2008–2013.

The performances of the ANN and PLS models during disturbed conditions gave R value of ≈ 0.656 and 0.658, respectively, based on 865 observations. Although the ANN model performs slightly better on $\triangle H$-derived $\mathbf{E} \times \mathbf{B}$ drift than the PLS model, during disturbed period (shown in Table 5.3) their performance is very comparable.
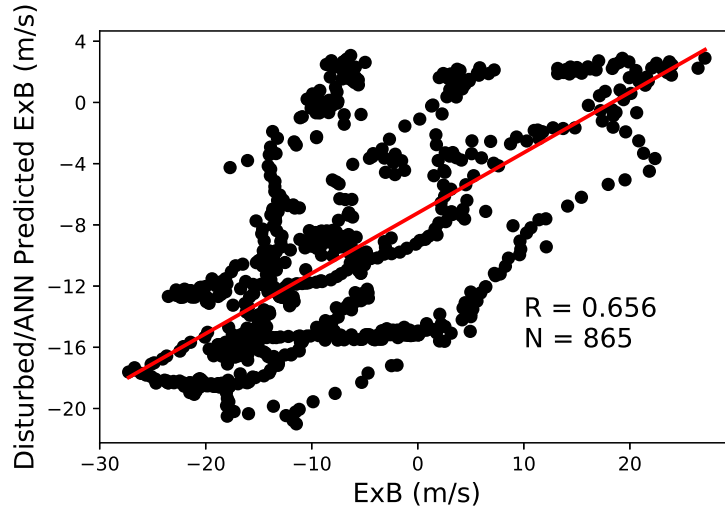
Figure 5.17: Comparison of ANN modeled results with measured $\mathbf{E} \times \mathbf{B}$ for disturbed condition. R and N represent the correlation coefficient and number of observations used.

5.8 Summary

In-situ $\mathbf{E} \times \mathbf{B}$ drift from IVM instrument on-board C/NOFS satellite and ground-based magnetometers at low and equatorial latitudes have been used to develop an expression for estimating ionospheric vertical drifts. The $\triangle H$ from ground-based magnetometer observations at low and equatorial latitudes were subsequently used to derive and model $\mathbf{E} \times \mathbf{B}$ drift within the African region (over AAE) using ANN and PLS approaches. Input parameters which potentially influence the $\mathbf{E} \times \mathbf{B}$ drift were selected based on statistical analysis. While the performance of the two models were comparable, the ANN gave slightly better results than the PLS method. The calculated $RMSE$ values between observed and ANN modeled $\mathbf{E} \times \mathbf{B}$ drift were smaller during quiet and disturbed conditions in comparison with those estimated with the PLS technique. Maximum correlation coefficient values of ~ 0.81 and 0.66 during quiet and disturbed conditions have been achieved when our results were validated with $\triangle H$ inferred $\mathbf{E} \times \mathbf{B}$ drift. Maximum R value of ~ 0.78, obtained for the PLS method, was computed between the modeled results and C/NOFS $\mathbf{E} \times \mathbf{B}$ drift observations during quiet conditions. Although, we have limited C/NOFS $\mathbf{E} \times \mathbf{B}$ drift observations, the correlation coefficient values between our models and C/NOFS $\mathbf{E} \times \mathbf{B}$ drift are comparable (sometimes better) with those in earlier studies (e.g., Alken, 2009; Patra et al., 2014). It should be mentioned that sources of $\mathbf{E} \times \mathbf{B}$ drift observations and the period studied (e.g., Alken, 2009; Patra et al., 2014) are different.

Chapter 6

Summary, Conclusions and Future work

6.1 Introduction

The main objective of this work was developing an empirical model to estimate vertical $\mathbf{E} \times \mathbf{B}$ drift from $\triangle H$ data over Addis Ababa, AAE (9.02°N, 38.77°E) at all geomagnetic conditions. EOF, ANN and PLS are modelling methods that were used to achieve this objective. This chapter presents conclusions regarding vertical $\mathbf{E} \times \mathbf{B}$ drift modelling. Challenges, summary and possible future work are also presented in this chapter.

6.2 Challenges

The complexity in changes of low latitude vertical $\mathbf{E} \times \mathbf{B}$ drifts with various contributions such as local time and longitudinal effects being driven by effects of E-region tides on the equatorial electric field (e.g., Millward et al., 2001; Fejer et al., 2008; Maute et al., 2012), coupling between E and F-region electrodynamical phenomena (e.g., Anderson, 1973; Patra et al., 2004), geomagnetic activity effects (e.g., Fejer et al., 1979; Gonzales et al., 1979; Fejer, 1997) and solar activity on long-term scale in different seasons (e.g., Fejer et al., 1991; Chandra et al., 1997) necessitates the comprehensive understanding of vertical $\mathbf{E} \times \mathbf{B}$ drifts variability in different longitude sectors. The vertical $\mathbf{E} \times \mathbf{B}$ modelling study over the African sector is therefore a contribution to the ongoing $\mathbf{E} \times \mathbf{B}$ drift investigations in this regard.

6.3 Summary and Conclusions

A first time attempt to estimate and model low latitude vertical $\mathbf{E}\times\mathbf{B}$ drifts over the African region has been presented. Two broad approaches were investigated. The first one utilised an existing empirical expression developed by Anderson et al. (2004) and $\triangle H$ measurements over the African sector to derive vertical $\mathbf{E}\times\mathbf{B}$ drift data from 2008–2013. The derived $\mathbf{E}\times\mathbf{B}$ drifts were used as a database to develop an empirical model over the African low latitude region using empirical orthogonal functions for the first time (Dubazane et al., 2017). During the model development, model inputs considered were the solar flux index (F10.7) to take into account vertical $\mathbf{E}\times\mathbf{B}$ drift solar activity dependence (e.g., Richmond, 1973; Fejer et al., 1991) and Disturbance storm time (Dst) index to account for changes in $\mathbf{E}\times\mathbf{B}$ drifts as a result of changing magnetic activity over time. During geomagnetic storms, the low latitude electrodynamics may be modified either by prompt penetrating electric field (e.g., Fejer and Scherliess, 1995) or ionospheric disturbed dynamo electric field (Blanc and Richmond, 1980; Fejer and Scherliess, 1995). At some times, both these electric field sources are present during one geomagnetic storm condition (e.g., Fejer and Scherliess, 1995). One of the observations from this first modelling effort was the low or no correlation between EEJ/$\mathbf{E}\times\mathbf{B}$ drift and the solar activity during the extended solar minimum period of 2009–2010 (Dubazane et al., 2017); disagreeing with the established understanding that $\mathbf{E}\times\mathbf{B}$ drift depends on solar activity (Richmond, 1973; Fejer et al., 1991). This highlights that modelling $\mathbf{E}\times\mathbf{B}$ drift as a function of a solar activity indicator only would have missed the $\mathbf{E}\times\mathbf{B}$ drift response during 2008–2009. The other significant finding was that the climatological SF model (Scherliess and Fejer, 1999) strongly overestimates the $\triangle H$ derived vertical $\mathbf{E}\times\mathbf{B}$ drifts during local day-time over the African low latitudes. Independent validation was done using C/NOFS $\mathbf{E}\times\mathbf{B}$ drift measurements which were found to be closer to $\triangle H$ derived $\mathbf{E}\times\mathbf{B}$ drift (and the corresponding modelled values) than the SF model. The second step of the investigation dealt with C/NOFS $\mathbf{E}\times\mathbf{B}$ data processing during 2008–2013 and restricting the $\mathbf{E}\times\mathbf{B}$ drift data within $\pm$ 4 degrees latitude from the geomagnetic equator (to remain within the EEJ variability range which is 3 degrees), 38.8°$\pm$11.2° longitude around the location with $\triangle H$ measurements, and altitude of 400-450 km that has been used in several investigations comparing C/NOFS data with ground-based based observations (e.g., Rodrigues et al., 2011; Stoneback et al., 2011; Yizengaw et al., 2014a; Rodrigues et al., 2015). This was followed by finding coincidental times when C/NOFS $\mathbf{E}\times\mathbf{B}$ drift and $\triangle H$ measurements were simultaneously present which formed the data base used to

develop the expression relating the two sets of observations. The resulting database had 3140 datapoints from 2008–2013. A third order polynomial was then derived relating $\mathbf{E} \times \mathbf{B}$ and $\triangle H$ (Dubazane and Habarulema, 2017), following the results by Habarulema et al. (2017) showing that this is the suitable function to reconstruct $\mathbf{E} \times \mathbf{B}$ drift. The developed expression was then used to derive $\mathbf{E} \times \mathbf{B}$ drift data for the entire $\triangle H$ database (455 012 data-points) that was subsequently used in developing the partial least squares and neural network models. Both PLS and neural network models were developed using similar set of inputs comprising representations of diurnal variation, seasonal variation, solar and magnetic activities; and validated on dataset not used in models' development. Models' validation showed neural network model to be better in estimating vertical $\mathbf{E} \times \mathbf{B}$ drifts better than the PLS model during both quiet and disturbed conditions.

Both approaches investigated have a similar challenge of lack of ground-based observations from radars to validate the magnitude of the derived/modelled vertical $\mathbf{E} \times \mathbf{B}$ drifts. However results compare relatively well with C/NOFS measurements that were not used in models' construction. It has however been reported that C/NOFS provides downward vertical drifts in the afternoon hours which are absent in ground-based data such as the JULIA observations (e.g., Rodrigues et al., 2015). Unfortunately, C/NOFS data is not continuous to validate modelled data over the entire day. Vertical $\mathbf{E} \times \mathbf{B}$ drift values derived from $\triangle H$ using our quantitative relationship are mostly smaller than those derived using the relationship by Anderson et al. (2004). It is difficult to conclude on the most reliable results, although Anderson et al. (2004) was developed over a different longitude sector (Jicamarca) and coefficients will therefore not contain local effects over the African sector such as effects of E-region tides on the electric field which mostly determine the local and longitudinal effects of vertical $\mathbf{E} \times \mathbf{B}$ drifts (e.g., Millward et al., 2001; Lühr et al., 2004; Maute et al., 2012).

6.4   Future work

The reported results of vertical $\mathbf{E} \times \mathbf{B}$ drift over the African region are promising. Once validated with ground-based radar measurements, the approach of deriving separate expressions to infer vertical $\mathbf{E} \times \mathbf{B}$ drift has potential to increase day-day data coverage during local daytime in other longitude sectors which has previously been confined to areas with radars. This would in turn lead to development of equatorial vertical $\mathbf{E} \times \mathbf{B}$ drift models in all longitude sectors thereby increasing

the accuracy of estimating the vertical drifts on a global scale. The current most used model for low latitude vertical $\mathbf{E} \times \mathbf{B}$ drift specification and available data offer an opportunity to update the existing models for accurate specification of the equatorial vertical drifts (e.g., Fejer and Scherliess, 1995; Rodrigues et al., 2015).

Finally, it is proposed that inexpensive radar to determine Doppler velocities of the 150 km echoes (e.g., Woodman and Hagfors, 1969; Kudeki and Fawcett, 1993; Chau, 1998) similar to those is operational in Indonesia (Patra et al., 2008) and India (Patra and Rao, 2006) be installed in the African sector to validate our modelling results.

Bibliography

A, E., Zhang, D. H., Xiao, Z., Hao, Y. Q., Ridley, A. J. and Moldwin, M. (2011), 'Modeling ionospheric foF2 by using empirical orthogonal function analysis', *Annales Geophysicae* **29**(8), 1501–1515.

Abdu, M., Batista, I., Walker, G., Sobral, J., Trivedi, N. and De Paula, E. (1995), 'Equatorial ionospheric electric fields during magnetospheric disturbances: local time/longitude dependences from recent EITS campaigns', *Journal of Atmospheric and Terrestrial Physics* **57**(10), 1065–1083.

Adams, G. W., Brosnahan, J. W., Walden, D. C. and Nerney, S. F. (1986), 'Mesospheric observations using a 2.66-MHz radar as an imaging Doppler interferometer: Description and first results', *Journal of Geophysical Research: Space Physics* **91**(A2), 1671–1683.

Adebesin, B., Adeniyi, J., Adimula, I. and Reinisch, B. (2013), 'Equatorial vertical plasma drift velocities and electron densities inferred from ground-based ionosonde measurements during low solar activity', *Journal of Atmospheric and Solar-Terrestrial Physics* **97**, 58–64.

Adeniyi, J., Adebesin, B., Adimula, I., Oladipo, O., Olawepo, A., Ikubanni, S. and Reinisch, B. (2014), 'Comparison between African equatorial station ground-based inferred vertical E× B drift, Jicamarca direct measured drift, and IRI model', *Advances in Space Research* **54**(8), 1629–1641.

Alex, S. and Mukherjee, S. (2001), 'Local time dependence of the equatorial counter electrojet effect in a narrow longitudinal belt', *Earth, planets and space* **53**(12), 1151–1161.

Alken, P. (2009), 'A quiet time empirical model of equatorial vertical plasma drift in the Peruvian sector based on 150 km echoes', *Journal of Geophysical Research: Space Physics* **114**(A2).

Altinay, O., Tulunay, E. and Tulunay, Y. (1997), 'Forecasting of ionospheric critical frequency using neural networks', *Geophysical Research Letters* **24**(12), 1467–1470.

Anderson, D. (1973), 'A theoretical study of the ionospheric F region equatorial anomaly-I. Theory', *Planetary and Space Science* **21**, 409–419.

Anderson, D. (1981), 'Modeling the ambient, low latitude F-region ionosphere—A review', *Journal of Atmospheric and Terrestrial physics* **43**(8), 753–762.

Anderson, D., Anghel, A., Chau, J. and Veliz, O. (2004), 'Daytime vertical E× B drift velocities inferred from ground-based magnetometer observations at low latitudes', *Space Weather* **2**(11).

Anderson, D., Anghel, A., Chau, J., Yumoto, K., Bhattacharyya, A. and Alex, S. (2006), 'Daytime, low latitude, vertical ExB drift velocities, inferred from ground-based magnetometer observations in the Peruvian, Philippine and Indian longitude sectors under quiet and disturbed conditions'.

Anderson, D., Anghel, A., Yumoto, K., Ishitsuka, M. and Kudeki, E. (2002), 'Estimating daytime vertical ExB drift velocities in the equatorial F-region using ground-based magnetometer observations', *Geophysical Research Letters* **29**(12), 4–7.

Anderson, D. and Araujo-Pradere, E. A. (2010), 'Sudden stratospheric warming event signatures in daytime ExB drift velocities in the Peruvian and Philippine longitude sectors for January 2003 and 2004', *Journal of Geophysical Research: Space Physics* **115**(A8).

Anghel, A., Anderson, D., Maruyama, N., Chau, J., Yumoto, K., Bhattacharyya, A. and Alex, S. (2007), 'Interplanetary electric fields and their relationship to low-latitude electric fields under disturbed conditions', *Journal of Atmospheric and Solar-Terrestrial Physics* **69**(10), 1147–1159.

Baker, W. and Martyn, D. (1952), 'Conductivity of the ionosphere', *Nature* **170**(4339), 1090–1092.

Bakunina, I. A., Abramov-Maximov, V. E., Nakariakov, V. M., Lesovoy, S. V., Soloviev, A. A., Tikhomirov, Y. V., Melnikov, V. F., Shibasaki, K., Nagovitsyn, Y. A. and Averina, E. L. (2013), 'Long-period oscillations of sunspots by NoRH and SSRT observations', *Publications of the Astronomical Society of Japan* **65**(sp1).

Balan, N., Otsuka, Y., Bailey, G. and Fukao, S. (1998), 'Equinoctial asymmetries in the ionosphere and thermosphere observed by the MU radar', *Journal of Geophysical Research: Space Physics* **103**(A5), 9481–9495.

Bartels, J. (1963), Discussion of time-variations of geomagnetic activity, indices Kp and Ap, 1932-1961, *in* 'Annales de Geophysique', Vol. 19, p. 1.

Bataineh, M. and Marler, T. (2017), 'Neural network for regression problems with reduced training sets', *Neural Networks* **95**(Supplement C), 1–9.

Batista, I., Medeiros, R. d., Abdu, M., Souza, J. d., Bailey, G. and Paula, E. d. (1996), 'Equatorial ionospheric vertical plasma drift model over the Brazilian region', *Journal of Geophysical Research: Space Physics* **101**(A5), 10887–10892.

Bertoni, F., Batista, I., Abdu, M., Reinisch, B. and Kherani, E. (2006), 'A comparison of ionospheric vertical drift velocities measured by Digisonde and Incoherent Scatter Radar at the magnetic equator', *Journal of atmospheric and solar-terrestrial physics* **68**(6), 669–678.

Bhardwaj, S. (2009), 'Equatorial and low latitude geomagnetic field oscillations in the Indian region'.

Bilitza, D., Obrou, O., Adeniyi, J. and Oladipo, O. (2004), 'Variability of f o F2 in the equatorial ionosphere', *Advances in Space Research* **34**(9), 1901–1906.

Bilitza, D. and Reinisch, B. W. (2008), 'International reference ionosphere 2007: improvements and new parameters', *Advances in Space Research* **42**(4), 599–609.

Björnsson, H. and Venegas, S. (1997), 'A manual for EOF and SVD analyses of climatic data', *CCGCR Report* **97**(1), 112–134.

Blanc, M. and Richmond, A. (1980), 'The ionospheric disturbance dynamo', *Journal of Geophysical Research: Space Physics* **85**(A4), 1669–1686.

Borovsky, J. E. and Denton, M. H. (2006), 'Differences between CME-driven storms and CIR-driven storms', *Journal of Geophysical Research: Space Physics* **111**(A7).

Breit, G. and Tuve, M. A. (1926), 'A test of the existence of the conducting layer', *Physical Review* **28**(3), 554.

Brueckner, G., Delaboudiniere, J.-P., Howard, R., Paswaters, S., St Cyr, O., Schwenn, R., Lamy, P., Simnett, G., Thompson, B. and Wang, D. (1998), 'Geomagnetic storms caused by coronal mass

ejections (CMEs): March 1996 through June 1997', *Geophysical Research Letters* **25**(15), 3019–3022.

Butzer, P. L. and Nessel, R. J. (1971), 'Fourier analysis and approximation, Vol. 1', *New York: Academic* .

Cander, L. R. (2015), 'Forecasting foF2 and MUF (3000) F2 ionospheric characteristics–A challenging space weather frontier', *Advances in Space Research* **56**(9), 1973–1981.

Chandra, H., Vyas, G. and Sharma, S. (1997), 'Long-term changes in ionospheric parameters over Ahmedabad', *Advances in Space Research* **20**(11), 2161–2164.

Chapman, S. (1931), 'The absorption and dissociative or ionizing effect of monochromatic radiation in an atmosphere on a rotating earth', *Proceedings of the Physical Society* **43**(1), 26.

Chapman, S. and Bartels, J. (1940), *Geomagnetism*, Vol. 2, Clarendon Press.

Chapman, S. and Rao, K. R. (1965), 'The H and Z variations along and near the equatorial electrojet in India, Africa and the Pacific', *Journal of Atmospheric and Terrestrial Physics* **27**(4), 559–581.

Chau, J. (1998), 'Examination of various techniques for measuring wind velocities using clear-air radars, with emphasis on vertical wind measurements (Ph. D.), University of Colorado, Estados Unidos'.

Chau, J. L. and Woodman, R. F. (2004), 'Daytime vertical and zonal velocities from 150-km echoes: Their relevance to F-region dynamics', *Geophysical research letters* **31**(17).

Chen, Y., Liu, L. and Wan, W. (2011), 'Does the F10. 7 index correctly describe solar EUV flux during the deep solar minimum of 2007–2009?', *Journal of Geophysical Research: Space Physics* **116**(A4).

Chen, Y., Liu, L. and Wan, W. (2012), 'The discrepancy in solar EUV-proxy correlations on solar cycle and solar rotation timescales and its manifestation in the ionosphere', *Journal of Geophysical Research: Space Physics* **117**(A3).

Chen, Y., Wang, W., Burns, A. G., Liu, S., Gong, J., Yue, X., Jiang, G. and Coster, A. (2015), 'Ionospheric response to CIR-induced recurrent geomagnetic activity during the declining phase of solar cycle 23', *Journal of Geophysical Research: Space Physics* **120**(2), 1394–1418.

Ciclo, I. and Stefania, D. Z. (2013), 'The PLS regression model : algorithms and application to chemometric data Candidate ', *Università degli Studi di Udine* .

Clausen, L. B., H Baker, J., Ruohoniemi, J. M., Milan, S. E., Coxon, J., Wing, S., Ohtani, S. and Anderson, B. (2013), 'Temporal and spatial dynamics of the regions 1 and 2 Birkeland currents during substorms', *Journal of Geophysical Research: Space Physics* **118**(6), 3007–3016.

Coley, W. and Heelis, R. (1989), 'Low-latitude zonal and vertical ion drifts seen by DE 2', *Journal of Geophysical Research: Space Physics* **94**(A6), 6751–6761.

Cowley, S. (2000), 'Magnetosphere-ionosphere interactions: A tutorial review', *Magnetospheric current systems* pp. 91–106.

Coxon, J., Milan, S., Clausen, L., Anderson, B. and Korth, H. (2014), 'The magnitudes of the regions 1 and 2 Birkeland currents observed by AMPERE and their role in solar wind-magnetosphere-ionosphere coupling', *Journal of Geophysical Research: Space Physics* **119**(12), 9804–9815.

Craig, R. A. (2016), *The upper atmosphere: Meteorology and Physics*, Elsevier.

Crain, D., Heelis, R., Bailey, G. and Richmond, A. (1993), 'Low-latitude plasma drifts from a simulation of the global atmospheric dynamo', *Journal of Geophysical Research: Space Physics* **98**(A4), 6039–6046.

Cummer, S. A., Inan, U. S. and Bell, T. F. (1998), 'Ionospheric D region remote sensing using VLF radio atmospherics', *Radio Science* **33**(6), 1781–1792.

Daglis, I. A., Thorne, R. M., Baumjohann, W. and Orsini, S. (1999), 'The terrestrial ring current: Origin, formation, and decay', *Reviews of Geophysics* **37**(4), 407–438.

Davies, K. (1990), *Ionospheric radio*, number 31, IET.

Davis, T. N. and Sugiura, M. (1966), 'Auroral electrojet activity index AE and its universal time variations', *Journal of Geophysical Research* **71**(3), 785–801.

Dayal, B. S. and MacGregor, J. F. (1997), 'Recursive exponentially weighted PLS and its applications to adaptive control and prediction', *Journal of Process Control* **7**(3), 169–179.

De Jong, S. (1993), 'SIMPLS: an alternative approach to partial least squares regression', *Chemometrics and intelligent laboratory systems* **18**(3), 251–263.

de La Beaujardiere, O., Retterer, J. M., Pfaff, R. F., Roddy, P. A., Roth, C., Burke, W. J., Su, Y. J., Kelley, M. C., Ilma, R. R., Wilson, G. R. et al. (2009), 'C/NOFS observations of deep plasma depletions at dawn', *Geophysical Research Letters* **36**(18).

de La Beaujardière, O. et al. (2004), 'C/NOFS: A mission to forecast scintillations', *Journal of Atmospheric and Solar-Terrestrial Physics* **66**(17), 1573–1591.

Dhanjal, C., Gunn, S. R. and Shawe-Taylor, J. (2009), 'Efficient sparse kernel feature extraction based on partial least squares', *IEEE Transactions on Pattern Analysis and Machine Intelligence* **31**(8), 1347–1361.

Doumouya, V., Cohen, Y., Arora, B. and Yumoto, K. (2003), 'Local time and longitude dependence of the equatorial electrojet magnetic effects', *Journal of atmospheric and solar-terrestrial physics* **65**(14), 1265–1282.

Doumouya, V., Vassal, J., Cohen, Y., Fambitakoye, O. and Menvielle, M. (1998), 'Equatorial electrojet at African longitudes: first results from magnetic measurements', *Angeo* **16**, 658.

Dubazane, M. B. and Habarulema, J. B. (2017), 'An empirical Model of vertical Plasma drift over the African sector', *Space Weather* (Under Review).

Dubazane, M. B., Habarulema, J. B. and Uwamahoro, J. C. (2017), 'Modelling ionospheric vertical drifts over Africa low latitudes using Empirical Orthogonal functions and comparison with climatological model.', *Advances in Space Research* **61**(1), 326–336.

Elias, A. G. (2014), 'Filtering ionosphere parameters to detect trends linked to anthropogenic effects', *Earth, Planets and Space* **66**(1), 113.

Elman, J. L. (1990), 'Finding structure in time', *Cognitive science* **14**(2), 179–211.

England, S. L., Immel, T. J., Sagawa, E., Henderson, S. B., Hagan, M. E., Mende, S. B., Frey, H. U., Swenson, C. M. and Paxton, L. J. (2006), 'Effect of atmospheric tides on the morphology

of the quiet time, postsunset equatorial ionospheric anomaly', *Journal of Geophysical Research: Space Physics* **111**(10), 1–12.

Ezquer, R. G., López, J., Scidá, L., Cabrera, M., Zolesi, B., Bianchi, C., Pezzopane, M., Zuccheretti, E. and Mosert, M. (2014), 'Behaviour of ionospheric magnitudes of F2 region over Tucumán during a deep solar minimum and comparison with the IRI 2012 model predictions', *Journal of Atmospheric and Solar-Terrestrial Physics* **107**, 89–98.

Fambitakoye, O., Mayaud, P. and Richmond, A. (1976), 'Equatorial electrojet and regular daily variation SR—III. Comparison of observations with a physical model', *Journal of Atmospheric and Terrestrial Physics* **38**(2), 113–121.

Fang, T., Richmond, A., Liu, J. and Maute, A. (2008), 'Wind dynamo effects on ground magnetic perturbations and vertical drifts', *Journal of Geophysical Research: Space Physics* **113**(A11).

Farley, D., Bonelli, E., Fejer, B. G. and Larsen, M. (1986), 'The prereversal enhancement of thezonal electric field in the equatorial ionosphere', *Journal of Geophysical Research* **91**(A12).

Fausett, L. (1994), *Fundamentals of neural networks: architectures, algorithms, and applications*, number 006.3, Prentice-Hall,.

Fejer, B. G. (1997), 'The electrodynamics of the low-latitude ionosphere: Recent results and future challenges', *Journal of Atmospheric and Solar-Terrestrial Physics* **59**(13), 1465–1482.

Fejer, B. G. (2011), 'Low latitude ionospheric electrodynamics', *Space Science Reviews* **158**(1), 145–166.

Fejer, B. G., De Paula, E., Heelis, R. and Hanson, W. (1995), 'Global equatorial ionosphericvertical plasma drifts measured by the AE-E satellite', *Journal of Geophysical Research* **100**(A4).

Fejer, B. G. and Emmert, J. (2003), 'Low-latitude ionospheric disturbance electric field effects during the recovery phase of the 19–21 October 1998 magnetic storm', *Journal of Geophysical Research: Space Physics* **108**(A12).

Fejer, B. G., Farley, D., Woodman, R. and Calderon, C. (1979), 'Dependence of equatorial F region vertical drifts on season and solar cycle', *Journal of Geophysical Research: Space Physics* **84**(A10), 5792–5796.

Fejer, B. G., Jensen, J. W. and Su, S.-Y. (2008), 'Quiet time equatorial F region vertical plasma drift model derived from ROCSAT-1 observations', *Journal of Geophysical Research: Space Physics* **113**(A5).

Fejer, B. G., Paula, E. d., Gonzalez, S. and Woodman, R. (1991), 'Average vertical and zonal F region plasma drifts over Jicamarca', *Journal of Geophysical Research: Space Physics* **96**(A8), 13901–13906.

Fejer, B. G. and Scherliess, L. (1995), 'Time dependent response of equatorial ionospheric electric fields to magnetospheric disturbances', *Geophysical Research Letters* **22**(7), 851–854.

Fesen, C. G., Hysell, D. L., Meriwether, J. M., Mendillo, M., Fejer, B. G., Roble, R. G., Reinisch, B. W. and Biondi, M. A. (2002), 'Modeling the low-latitude thermosphere and ionosphere', *Journal of Atmospheric and Solar-Terrestrial Physics* **64**(12-14), 1337–1349.

Finlayson-Pitts, B. J. and Pitts Jr, J. N. (1999), *Chemistry of the upper and lower atmosphere: theory, experiments, and applications*, Academic press.

Forbes, J. M. (1981), 'The equatorial electrojet', *Reviews of Geophysics* **19**(3), 469–504.

Forbes, J. M. (1982), 'Atmospheric tides: 1. Model description and results for the solar diurnal component', *Journal of Geophysical Research: Space Physics* **87**(A7), 5222–5240.

Forbes, J. M. (1995), 'Tidal and planetary waves', *The upper mesosphere and lower thermosphere: a review of experiment and theory* pp. 67–87.

Fuller, M., Ritter, G. and Draper, C. (1988), 'Partial least-squares quantitative analysis of infrared spectroscopic data. Part I: Algorithm implementation', *Applied Spectroscopy* **42**(2), 217–227.

Fuller-Rowell, T., Codrescu, M., Fejer, B. G., Borer, W., Marcos, F. and Anderson, D. (1997), 'Dynamics of the low-latitude thermosphere: Quiet and disturbed conditions', *Journal of Atmospheric and Solar-Terrestrial Physics* **59**(13), 1533–1540.

Geladi, P. and Kowalski, B. R. (1986), 'Partial least-squares regression: a tutorial', *Analytica chimica acta* **185**, 1–17.

Golub, G. H. and Van Loan, C. F. (1996), 'Matrix computations. 1996', *Johns Hopkins University, Press, Baltimore, MD, USA* pp. 374–426.

Gonzales, C., Kelley, M., Fejer, B. G., Vickrey, J. and Woodman, R. (1979), 'Equatorialelectric fields during magnetically disturbed conditions, 2. Implications of simultaneousauroral and equatorial measurements', *Journal of Geophysical Research* **84**(A10).

Gopalswamy, N., Xie, H., Mäkelä, P., Akiyama, S., Yashiro, S., Kaiser, M., Howard, R. and Bougeret, J.-L. (2010), 'Interplanetary shocks lacking type II radio bursts', *The Astrophysical Journal* **710**(2), 1111.

Grodji, F., Doumbia, V., Boka, K., Amory-Mazaudier, C., Cohen, Y. and Fleury, R. (2017), 'Estimating some parameters of the equatorial ionosphere electrodynamics from ionosonde data in West Africa', *Advances in Space Research* **59**(1), 311–325.

Habarulema, J. B. (2011), A contribution to TEC modelling over Southern Africa using GPS data, PhD thesis, Rhodes University.

Habarulema, J. B., Dubazane, M. B., Katamzi, Z. T., Yizengaw, E., Moldwin, M. B. and Uwamahoro, J. C. (2017), 'Long-term estimation of day-day vertical E B drift velocities using C/NOFS and ground-based magnetometer observations', *JOURNAL OF GEOPHYSICAL RESEARCH* (Under Review).

Habarulema, J. B., Katamzi, Z. T., Yizengaw, E., Yamazaki, Y. and Seemala, G. (2016), 'Simultaneous storm time equatorward and poleward large-scale TIDs on a global scale', *Geophysical Research Letters* **43**(13), 6678–6686.

Hagan, M. and Forbes, J. (2002), 'Migrating and nonmigrating diurnal tides in the middle and upper atmosphere excited by tropospheric latent heat release', *Journal of Geophysical Research: Atmospheres* **107**(D24).

Hagan, M., Maute, A., Roble, R., Richmond, A., Immel, T. and England, S. (2007), 'Connections between deep tropical clouds and the Earth's ionosphere', *Geophysical Research Letters* **34**(20).

Haile, T. (2003), 'Equatorial electrojet strength in the African sector during high and low solar activity years', *SINET: Ethiopian Journal of Science* **26**(1), 77–81.

Hamid, N. S. A., Liu, H., Uozumi, T., Yumoto, K. et al. (2013), 'Equatorial electrojet dependence on solar activity in the Southeast Asia sector', *Antarctic Record* **57**(3), 329–337.

Hannachi, A. (2004), 'A primer for EOF analysis of climate data', *Department of Meteorology, University of Reading* pp. 1–33.

Hannachi, A., Jolliffe, I. and Stephenson, D. (2007), 'Empirical orthogonal functions and related techniques in atmospheric science: A review', *International journal of climatology* **27**(9), 1119–1152.

Hargreaves, J. K. (1979), 'The upper atmosphere and solar-terrestrial relations-An introduction to the aerospace environment', *New York, Van Nostrand Reinhold Co., 1979. 312 p.* .

Hargreaves, J. K. (1992), *The solar-terrestrial environment: an introduction to geospace-the science of the terrestrial upper atmosphere, ionosphere, and magnetosphere*, Cambridge University Press.

Haykin, S. (1994), *Neural networks: a comprehensive foundation*, Prentice Hall PTR.

Haykin, S. and Network, N. (2004), 'A comprehensive foundation', *Neural Networks* **2**(2004), 41.

Hecht-Nielsen, R. (1990), 'Neurocomputing.', *Reading: Addison-Wesley Google Scholar* .

Heelis, R., Kendall, P., Moffett, R., Windle, D. and Rishbeth, H. (1974), 'Electrical coupling of the E-and F-regions and its effect on F-region drifts and winds', *Planetary and Space Science* **22**(5), 743–756.

Helland, K., Berntsen, H. E., Borgen, O. S. and Martens, H. (1992), 'Recursive algorithm for partial least squares regression', *Chemometrics and intelligent laboratory systems* **14**(1-3), 129–137.

Hertz, J. A., Krogh, A. S. and Palmer, R. G. (1991), *Introduction to the theory of neural computation*, Vol. 1, Basic Books.

Hines, C. (1965), 'Dynamical heating of the upper atmosphere', *Journal of Geophysical Research* **70**(1), 177–183.

Hinteregger, H. (1976), 'EUV fluxes in the solar spectrum below 2000 Å', *Journal of Atmospheric and Terrestrial Physics* **38**(8), 791–806.

Hirono, M. (1952), 'A theory of diurnal magnetic variations in equatorial regions and conductivity of the ionosphere E region', *Journal of geomagnetism and geoelectricity* **4**(1), 7–21.

Höskuldsson, A. (1988), 'PLS regression methods', *Journal of chemometrics* **2**(3), 211–228.

Huba, J., Joyce, G. and Fedder, J. (2000), 'Sami2 is Another Model of the Ionosphere (SAMI2): A new low-latitude ionosphere model', *Journal of Geophysical Research: Space Physics* **105**(A10), 23035–23053.

Huber, P. (1981), 'J. 1981. Robust Statistics', *New York: John Wiley* .

Hui, D. (2015), 'Altitudinal Variability of Quiet-time Plasma Drifts in the Equatorial Ionosphere', *Ph.D. Thesis, 113 pp., Utah State Univ., Logan, 25 June* .

Iijima, T. and Potemra, T. A. (1978), 'Large-scale characteristics of field-aligned currents associated with substorms', *Journal of Geophysical Research: Space Physics* **83**(A2), 599–615.

Immel, T. J., Sagawa, E., England, S. L., Henderson, S. B., Hagan, M. E., Mende, S. B., Frey, H. U., Swenson, C. M. and Paxton, L. J. (2006*a*), 'Control of equatorial ionospheric morphology by atmospheric tides', *Geophysical Research Letters* **33**(15), 1–16.

Immel, T. J., Sagawa, E., England, S. L., Henderson, S. B., Hagan, M. E., Mende, S. B., Frey, H. U., Swenson, C. M. and Paxton, L. J. (2006*b*), 'Control of equatorial ionospheric morphology by atmospheric tides', *Geophysical Research Letters* **33**(15), 1–16.

Jaeger, H. (2001), *Short term memory in echo state networks*, Vol. 5, GMD-Forschungszentrum Informationstechnik.

Jain, A. K., Mao, J. and Mohiuddin, K. M. (1996), 'Artificial neural networks: A tutorial', *Computer* **29**(3), 31–44.

Jesan, J. P. and Lauro, D. M. (2003), 'Human brain and neural network behavior: a comparison', *Ubiquity* **2003**(November), 2–2.

Jolliffe, I. (2002), *Principal component analysis*, Wiley Online Library.

Joshi, L. M. and Sripathi, S. (2016), 'On the utility of the ionosonde Doppler-derived EXB drift during the daytime', *Journal of Geophysical Research: Space Physics* **121**(3), 2795–2811.

Jursa, A. S. et al. (1985), *Handbook of geophysics and the space environment*, NTIS Springfield, VA.

Kalman, B. L. and Kwasny, S. C. (1992), Why tanh: choosing a sigmoidal function, *in* 'Neural Networks, 1992. IJCNN., International Joint Conference on', Vol. 4, IEEE, pp. 578–581.

Kane, R. (1996), 'Quasi-biennial oscillations in quiet-day ranges of low latitude geomagnetic H component'.

Karunanithi, N., Whitley, D. and Malaiya, Y. K. (1992), 'Using neural networks in reliability prediction', *IEEE Software* **9**(4), 53–59.

Kelley, M. C. (2009), *The Earth's ionosphere: plasma physics and electrodynamics*, Vol. 96, Academic press.

Kelley, M. C., Makela, J. J., Chau, J. L. and Nicolls, M. J. (2003), 'Penetration of the solar wind electric field into the magnetosphere/ionosphere system', *Geophysical Research Letters* **30**(4).

Kelley, M., Fejer, B. G. and Gonzales, C. (1979), 'An explanation for anomalous equatorial ionospheric electric fields associated with a northward turning of the interplanetary magnetic field', *Geophysical Research Letters* **6**(4), 301–304.

Kelly, K. A. (1985), 'The influence of winds and topography on the sea surface temperature patterns over the northern California slope', *Journal of Geophysical Research: Oceans* **90**(C6), 11783–11798.

Kelly, M. C. (1989), 'The Earth's ionosphere', *Int. Geophys. Ser* **43**, 71.

Kikuchi, T., Liihr, H., Schlegel, K., Tachihara, H. and Shinohara, M. (2000), 'Penetration of auroral electric fields to the equator', *Journal of geophysical research* **105**(A10), 23251–23261.

Kil, H., Oh, S.-J., Kelley, M., Paxton, L., England, S., Talaat, E., Min, K.-W. and Su, S.-Y. (2007), 'Longitudinal structure of the vertical E$\times$ B drift and ion density seen from ROCSAT-1', *Geophysical Research Letters* **34**(14).

Krishna Murthy, B., Hari, S. and Somayajulu, V. (1990), 'Nighttime equatorial thermospheric meridional winds from ionospheric h'F data', *Journal of Geophysical Research: Space Physics* **95**(A4), 4307–4310.

Kudeki, E. and Fawcett, C. D. (1993), 'High resolution observations of 150 km echoes at Jicamarca', *Geophysical research letters* **20**(18), 1987–1990.

Kumar, S., Veenadhari, B., Ram, S. T., Su, S.-Y. and Kikuchi, T. (2016), 'Possible relationship between the equatorial electrojet (EEJ) and daytime vertical E× B drift velocities in F region from ROCSAT observations', *Advances in Space Research* **58**(7), 1168–1176.

Lay, E. H. and Shao, X.-M. (2011), 'High temporal and spatial-resolution detection of D-layer fluctuations by using time-domain lightning waveforms', *Journal of Geophysical Research: Space Physics* **116**(A1).

Le Cun, Y., Touresky, D., Hinton, G. and Sejnowski, T. (1988), A theoretical framework for back-propagation, *in* 'Proceedings of the 1988 Connectionist Models Summer School', CMU, Pittsburgh, Pa: Morgan Kaufmann, pp. 21–28.

Levenberg, K. (1944), 'A Method for the Solution of Certain Problems in Least Squares. Quart. Appl. Math. 2.'.

Lin, C., Wang, W., Hagan, M. E., Hsiao, C., Immel, T., Hsu, M., Liu, J., Paxton, L., Fang, T.-W. and Liu, C. (2007), 'Plausible effect of atmospheric tides on the equatorial ionosphere observed by the FORMOSAT-3/COSMIC: Three-dimensional electron density structures', *Geophysical Research Letters* **34**(11).

Lindberg, W., Persson, J.-A. and Wold, S. (1983), 'Partial least-squares method for spectrofluorimetric analysis of mixtures of humic acid and lignin sulfonate', *Analytical Chemistry* **55**(4), 643–648.

Lippmann, R. (1987), 'An introduction to computing with neural nets', *IEEE Assp magazine* **4**(2), 4–22.

Liu, L., Wan, W., Chen, Y. and Le, H. (2011), 'Solar activity effects of the ionosphere: A brief review', *Csb* **56**(12), 1202–1211.

Lorenz, E. N. (1956), 'Empirical orthogonal functions and statistical weather prediction', *Cambridge Massachusetts, Scientific Report No. 1* .

Lühr, H., Maus, S. and Rother, M. (2004), 'Noon-time equatorial electrojet: Its spatial features as determined by the CHAMP satellite', *Journal of Geophysical Research: Space Physics* **109**(A1).

Lühr, H., Rother, M., Häusler, K., Alken, P. and Maus, S. (2008), 'The influence of nonmigrating tides on the longitudinal variation of the equatorial electrojet', *Journal of Geophysical Research: Space Physics* **113**(A8).

Lühr, H., Rother, M., Häusler, K., Fejer, B. and Alken, P. (2012), 'Direct comparison of nonmigrating tidal signatures in the electrojet, vertical plasma drift and equatorial ionization anomaly', *Journal of Atmospheric and Solar-Terrestrial Physics* **75**, 31–43.

Ma, X., Maruyama, T., Ma, G. and Takeda, T. (2005), 'Three-dimensional ionospheric tomography using observation data of GPS ground receivers and ionosonde by neural network', *Journal of Geophysical Research: Space Physics* **110**(A5).

Mallat, S. G. (1989), 'A theory for multiresolution signal decomposition: the wavelet representation', *IEEE transactions on pattern analysis and machine intelligence* **11**(7), 674–693.

Manne, R. (1987), 'Analysis of two partial-least-squares algorithms for multivariate calibration', *Chemometrics and Intelligent Laboratory Systems* **2**(1-3), 187–197.

Marquardt, D. W. (1963), 'An algorithm for least-squares estimation of nonlinear parameters', *Journal of the society for Industrial and Applied Mathematics* **11**(2), 431–441.

Marra, S. and Morabito, F. C. (2005), A New Technique for Solar Activity Forecasting using Recurrent Elman Networks., *in* 'IEC (Prague)', pp. 68–73.

Martins, J. P. A., Teofilo, R. F. and Ferreira, M. (2010), 'Computational performance and cross-validation error precision of five PLS algorithms using designed and real data sets', *Journal of Chemometrics* **24**(6), 320–332.

Maute, A., Richmond, A. and Roble, R. (2012), 'Sources of low-latitude ionospheric E× B drifts and their variability', *Journal of Geophysical Research: Space Physics* **117**(A6).

Mayaud, P. (1977), 'The equatorial counter-electrojet—a review of its geomagnetic aspects', *Journal of Atmospheric and Terrestrial Physics* **39**(9-10), 1055–1070.

McCulloch, W. S. and Pitts, W. (1943), 'A logical calculus of the ideas immanent in nervous activity', *The bulletin of mathematical biophysics* **5**(4), 115–133.

McKinnell, L. and Poole, A. (2001), 'Ionospheric variability and electron density profile studies with neural networks', *Advances in Space Research* **27**(1), 83–90.

McNamara, L. F. (1991), *The ionosphere: communications, surveillance, and direction finding*, Krieger publishing company.

Mechtly, E. and Smith, L. (1968), 'Growth of the D-region at sunrise', *Journal of Atmospheric and Terrestrial Physics* **30**(3), 363–369.

Meggs, R. W. (2005), Mapping of ionospheric total electron content using global navigation satellite systems, PhD thesis, University of Bath;.

Millward, G., Moffett, R., Quegan, S. and Fuller-Rowell, T. (1996), 'A coupled thermosphere-ionosphere-plasmasphere model (CTIP)', *STEP Handbook on Ionospheric Models* pp. 239–279.

Millward, G., Müller-Wodarg, I., Aylward, A., Fuller-Rowell, T., Richmond, A. and Moffett, R. (2001), 'An investigation into the influence of tidal forcing on F region equatorial vertical ion drift using a global ionosphere-thermosphere model with coupled electrodynamics', *Journal of Geophysical Research: Space Physics* **106**(A11), 24733–24744.

Miyoshi, Y. and Kataoka, R. (2005), 'Ring current ions and radiation belt electrons during geomagnetic storms driven by coronal mass ejections and corotating interaction regions', *Geophysical research letters* **32**(21).

Montgomery, D. C., Peck, E. A. and Vining, G. G. (2012), *Introduction to linear regression analysis*, Vol. 821, John Wiley & Sons.

Müller, B., Reinhardt, J. and Strickland, M. T. (1990), 'Physics of Neural Networks', *Neural Networks An Introduction* .

Muller-Wodarg, I. (1997), 'Modelling perturbations propagating through the mesopause into the Earth's upper atmosphere', *The Observatory* **117**, 388–388.

Nishida, A. (1968), 'Coherence of geomagnetic DP 2 fluctuations with interplanetary magnetic variations', *Journal of Geophysical Research* **73**, 5549–5559.
  URL: *http://onlinelibrary.wiley.com/doi/10.1029/JA073i017p05549/full*

Ondo, T. and Marubashi, K. (2000), 'Wave Summit Course Science of Space Environment'.

Oyekola, O. and Kolawole, L. (2010), 'Equatorial vertical E× B drift velocities inferred from ionosonde measurements over Ouagadougou and the IRI-2007 vertical ion drift model', *Advances in Space Research* **46**(5), 604–612.

Oyekola, O. S. and Oluwafemi, C. C. (2007), 'Morphology of F -region vertical E B drifts in the African sector using ionosonde measurements', **50**(N. 5), 615–625.

Oyeyemi, E. O., McKinnell, L.-A. and Poole, A. W. (2007), 'Neural network-based prediction techniques for global modeling of M (3000) F2 ionospheric parameter', *Advances in Space Research* **39**(5), 643–650.

Patil, A., Rao, D. and Rastogi, R. (1990), 'Equatorial electrojet strengths in the Indian and American sectors', *Journal of geomagnetism and geoelectricity* **42**(7), 801–811.

Patra, A., Chaitanya, P. P. and Bhattacharyya, A. (2012), 'On the nature of radar backscatter and 250 MHz scintillation linked with an intense daytime Es patch', *Journal of Geophysical Research: Space Physics* **117**(A3).

Patra, A. K., Chaitanya, P. P., Otsuka, Y., Yokoyama, T., Yamamoto, M., Stoneback, R. A. and Heelis, R. A. (2014), 'Vertical ExB drifts from radar and C/NOFS observations in the Indian and Indonesian sectors: Consistency of observations and model', *Journal of Geophysical Research: Space Physics* **119**(5), 3777–3788.

Patra, A. and Rao, N. V. (2006), 'Radar observations of daytime 150-km echoes from outside the equatorial electrojet belt over Gadanki', *Geophysical research letters* **33**(3).

Patra, A., Sripathi, S. and Tiwari, D. (2004), 'Coupling effect of the equatorial F region irregularities on the low latitude E region instability processes', *Geophysical research letters* **31**(17).

Patra, A., Yokoyama, T., Otsuka, Y. and Yamamoto, M. (2008), 'Daytime 150-km echoes observed with the Equatorial Atmosphere Radar in Indonesia: First results', *Geophysical Research Letters* **35**(6).

Pearson, K. (1896), 'Mathematical contributions to the theory of evolution. III. Regression, heredity, and panmixia', *Philosophical Transactions of the Royal Society of London. Series A, containing papers of a mathematical or physical character* **187**, 253–318.

Perna, L. and Pezzopane, M. (2016), 'foF2 vs solar indices for the Rome station: Looking for the best general relation which is able to describe the anomalous minimum between cycles 23 and 24', *Journal of Atmospheric and Solar-Terrestrial Physics* **148**, 13–21.

Peymirat, C., Richmond, A. and Kobea, A. (2000), 'Electrodynamic coupling of high and low latitudes: Simulations of shielding/overshielding effects', *Journal of Geophysical Research: Space Physics* **105**(A10), 22991–23003.

Poole, A. W. and McKinnell, L.-A. (2000), 'On the predictability of f0F2 using neural networks', *Radio Science* **35**(1), 225–234.

Prölss, G. (1993), 'Common origin of positive ionospheric storms at middle latitudes and the geomagnetic activity effect at low latitudes', *Journal of Geophysical Research: Space Physics* **98**(A4), 5981–5991.

Prölss, G. W. and Bird, M. K. (2004), *Physics of the Earth's space environment: an introduction*, Springer.

Qiao, J., Wang, G., Li, W. and Li, X. (2017), 'A deep belief network with {PLSR} for nonlinear system modeling', *Neural Networks* pp. –.
URL: *https://www.sciencedirect.com/science/article/pii/S0893608017302496*

Qin, S. (1993), A recursive PLS algorithm for system identification, *in* 'AIChE Annual Meeting', St. Louis USA.

Qin, S. J. (1998), 'Recursive PLS algorithms for adaptive data modeling', *Computers & Chemical Engineering* **22**(4-5), 503–514.

Rabiu, A. B., Folarin, O. O., Uozumi, T., Hamid, N. S. A. and Yoshikawa, A. (2017), Longitudinal variation of equatorial electrojet and the occurrence of its counter electrojet, *in* 'Annales Geophysicae', Vol. 35, Copernicus GmbH, p. 535.

Rabiu, A. B., Yumoto, K., Falayi, E. O., Bello, O. R. and Group, M. C. (2011), 'Ionosphere over Africa : Results from Geomagnetic Field Measurements During International Heliophysical Year IHY', **6**(2), 63–66.

Rabiu, A., Onwumechili, C., Nagarajan, N. and Yumoto, K. (2013), 'Characteristics of equatorial electrojet over India determined from a thick current shell model', *Journal of Atmospheric and Solar-Terrestrial Physics* **92**, 105–115.

Rangarajan, G. (1985), 'Quasi-biennial oscillation in geomagnetic disturbance field', *Proceedings of the Indian Academy of Sciences-Earth and Planetary Sciences* **94**(1), 29–34.

Rao, D. and Rangarajan, G. (1978), 'The pole-tide signal in the geomagnetic field at a low-latitude station', *Geophysical Journal International* **53**(3), 617–621.

Rasmusson, E. M., Arkin, P. A., Chen, W.-Y. and Jalickee, J. B. (1981), 'Biennial variations in surface temperature over the United States as revealed by singular decomposition', *Monthly Weather Review* **109**(3), 587–598.

Rastogi, R. (1974), 'Westward equatorial electrojet during daytime hours', *Journal of Geophysical Research* **79**(10), 1503–1512.

Rastogi, R. G. and Chandra, H. (2015), 'Equatorial electrojet in the African sector', *Indian Journal of Radio and Space Physics* **44**(4), 187–198.

Rastogi, R. and Klobuchar, J. (1990), 'Ionospheric electron content within the equatorial F 2 layer anomaly belt', *Journal of Geophysical Research: Space Physics* **95**(A11), 19045–19052.

Rees, M. H. (1989), *Physics and chemistry of the upper atmosphere*, Vol. 1, Cambridge University Press.

Retterer, J. and Kelley, M. (2010), 'Solar wind drivers for low-latitude ionosphere models during geomagnetic storms', *Journal of Atmospheric and Solar-Terrestrial Physics* **72**(4), 344–349.

Richardson, I. G. (2013), 'Geomagnetic activity during the rising phase of solar cycle 24', *Journal of Space Weather and Space Climate* **3**, A08.

Richmond, A. (1973), 'Equatorial electrojet—I. Development of a model including winds and instabilities', *Journal of Atmospheric and Terrestrial physics* **35**(6), 1083–1103.

Richmond, A. (1995*a*), 'Modeling equatorial ionospheric electric fields', *Journal of Atmospheric and Terrestrial Physics* **57**(10), 1103–1115.

Richmond, A. (1995*b*), 'The ionospheric wind dynamo: effects of its coupling with different atmospheric regions', *The upper mesosphere and lower thermosphere: a review of experiment and theory* pp. 49–65.

Richmond, A. D. (1995*c*), 'Ionospheric electrodynamics', *Handbook of atmospheric electrodynamics* **2**, 249–290.

Richmond, A. D. (1995*d*), 'Modeling equatorial ionospheric electric fields', *Journal of Atmospheric and Terrestrial Physics* **57**(10), 1103–1115.

Richmond, A., Ridley, E. and Roble, R. (1992), 'A thermosphere/ionosphere general circulation model with coupled electrodynamics', *Geophysical Research Letters* **19**(6), 601–604.

Riley, K., Hobson, M. and Bence, S. (1999), 'Mathematical methods for physics and engineering'.

Rishbeth, H. (1971), 'Polarization fields produced by winds in the equatorial F-region', *Planetary and Space Science* **19**(3), 357–369.

Rishbeth, H. (1977), 'Dynamics of the equatorial F-region', *Journal of atmospheric and terrestrial physics* **39**(9-10), 1159–1168.

Rishbeth, H. (1997), 'The ionospheric E-layer and F-layer dynamos—a tutorial review', *Journal of Atmospheric and Solar-Terrestrial Physics* **59**(15), 1873–1880.

Rishbeth, H. and Garriott, . K. (1969), 'Introduction to Ionospheric Physics', *International Physics Series* **14**.

Rodrigues, F., Crowley, G., Azeem, S. and Heelis, R. (2011), 'C/NOFS observations of the equatorial ionospheric electric field response to the 2009 major sudden stratospheric warming event', *Journal of Geophysical Research: Space Physics* **116**(A09316).

Rodrigues, F. S., Smith, J. M., Milla, M. and Stoneback, R. A. (2015), 'Daytime ionospheric equatorial vertical drifts during the 2008–2009 extreme solar minimum', *Journal of Geophysical Research: Space Physics* **120**(2), 1452–1459.

Rosipal, R. and Krämer, N. (2006), Overview and recent advances in partial least squares, *in* 'Subspace, latent structure and feature selection', Springer, pp. 34–51.

Rumelhart, D. E. and Mcclelland, J. L. (1986), 'Parallel distributed processing: Explorations in the microstructure of cognition: Foundations (Parallel distributed processing)'.

Sagawa, E., Immel, T., Frey, H. and Mende, S. (2005), 'Longitudinal structure of the equatorial anomaly in the nighttime ionosphere observed by IMAGE/FUV', *Journal of Geophysical Research: Space Physics* **110**(A11).

Sastri, J. H. (1988), 'Equatorial electric-fields of ionospheric disturbance dynamo orgin'.

Sastri, J. H. (1990), 'Equatorial anomaly in F-region—A review'.

Sastri, J. H. (1996), 'Longitudinal dependence of equatorial F region vertical plasma drifts in the dusk sector', *Journal of Geophysical Research: Space Physics* **101**(A2), 2445–2452.

Scherliess, L. and Fejer, B. G. (1997), 'Storm time dependence of equatorial disturbance dynamo zonal electric fields', *Journal of Geophysical Research: Space Physics* **102**(A11), 24037–24046.

Scherliess, L. and Fejer, B. G. (1999), 'Radar and satellite glo bal equatorial F region vertical electric only in the American sector during In this case , for a solar flux index of', **104**, 6829–6842.

Schunk, R. and Nagy, A. (2009), *Ionospheres: physics, plasma physics, and chemistry*, Cambridge university press.

Seaton, M. (1955), Theories of the airglow spectrum, *in* 'Annales de Geophysique', Vol. 11, p. 232.

Sechrist, C. (1968), 'Interpretation of pre-sunrise electron densities and negative ions in the D-region', *Journal of Atmospheric and Terrestrial Physics* **30**(3), 371–389.

Selvakumaran, R., Veenadhari, B., Akiyama, S., Pandya, M., Gopalswamy, N., Yashiro, S., Kumar, S., Mäkelä, P. and Xie, H. (2016), 'On the reduced geoeffectiveness of solar cycle 24: A moderate storm perspective', *Journal of Geophysical Research: Space Physics* **121**(9), 8188–8202.

Smith, J., Rodrigues, F. S. and de Paula, E. (2015), Radar and satellite investigations of equatorial evening vertical drifts and spread F, *in* 'Annales Geophysicae', Vol. 33, Copernicus Gesellschaft Mbh.

Smith, N. and Kirby, S. (1937), 'Critical frequencies of low ionosphere layers', *Physical Review* **51**(10), 890.

Solomon, S. C., Qian, L. and Burns, A. G. (2013), 'The anomalous ionosphere between solar cycles 23 and 24', *Journal of Geophysical Research: Space Physics* **118**(10), 6524–6535.

Specht, D. F. (1991), 'A general regression neural network', *IEEE transactions on neural networks* **2**(6), 568–576.

Spiro, R., Wolf, R. and Fejer, B. G. (1988), Penetrating of high-latitude-electric-field effects to low latitudes during SUNDIAL 1984, *in* 'Annales Geophysicae', Vol. 6, pp. 39–49.

Stening, R. (1995), Variations in the strength of the Sq current system, *in* 'Annales Geophysicae', Vol. 13, p. 627.

Stolle, C., Manoj, C., Lühr, H., Maus, S. and Alken, P. (2008), 'Estimating the daytime equatorial ionization anomaly strength from electric field proxies', *Journal of Geophysical Research: Space Physics* **113**(A9).

Stone, M. (1974), 'Cross-validatory choice and assessment of statistical predictions', *Journal of the royal statistical society. Series B (Methodological)* pp. 111–147.

Stoneback, R., Heelis, R., Burrell, A., Coley, W., Fejer, B. G. and Pacheco, E. (2011), 'Observations of quiet time vertical ion drift in the equatorial ionosphere during the solar minimum period of 2009', *Journal of Geophysical Research: Space Physics* **116**(A12327).

Su, S.-Y., Yeh, H. C., Heelis, R. A., Wu, J.-M., Yang, S. C., Lee, L.-F. and Chen, H. L. (1999), 'The ROCSAT-1 IPEI preliminary results: Low-latitude ionospheric plasma and flow variations', *Terrestrial, Atmospheric and Oceanic Sciences* **10**(4), 787–804.

Sugiura, M. (1963), 'Hourly values of equatorial Dst for the IGY'.

Sugiura, M. (1976), 'Quasi-biennial geomagnetic variation caused by the Sun', *Geophysical Research Letters* **3**(11), 643–646.

Tobiska, W. (1996), 'Current status of solar EUV measurements and modeling', *Advances in Space Research* **18**(3), 3–10.

Tsurutani, B. T., Echer, E., Shibata, K., Verkhoglyadova, O. P., Mannucci, A. J., Gonzalez, W. D., Kozyra, J. U. and Pätzold, M. (2014), 'The interplanetary causes of geomagnetic activity during the 7–17 March 2012 interval: a CAWSES II overview', *Journal of Space Weather and Space*

Climate **4**, A02.

URL: *http://www.swsc-journal.org/10.1051/swsc/2013056*

Uwamahoro, J. C. and Habarulema, J. B. (2015), 'Modelling total electron content during geo-magnetic storm conditions using empirical orthogonal functions and neural networks', *Journal of Geophysical Research: Space Physics* **120**(12), 11,000–11,012.

Vichare, G., Ridley, A. and Yiğit, E. (2012), 'Quiet-time low latitude ionospheric electrodynamics in the non-hydrostatic Global Ionosphere–Thermosphere Model', *Journal of Atmospheric and Solar-Terrestrial Physics* **80**, 161–172.

Villard, O. G. (1976), 'The ionospheric sounder and its place in the history of radio science', *Radio Science* **11**(11), 847–860.

Vincent, R. and Lesicar, D. (1991), 'Dynamics of the equatorial mesosphere: First results with a new generation partial reflection radar', *Geophysical Research Letters* **18**(5), 825–828.

Von Storch, H. (1999), Misuses of statistical analysis in climate research, *in* 'Analysis of Climate Variability', Springer, pp. 11–26.

Wang, X., Kruger, U. and Lennox, B. (2003), 'Recursive partial least squares algorithms for monitoring complex industrial processes', *Control Engineering Practice* **11**(6), 613–632.

Wanliss, J. A. and Showalter, K. M. (2006), 'High-resolution global storm index: Dst versus SYM-H', *Journal of Geophysical Research: Space Physics* **111**(A2).

Warren, H., Mariska, J. and Lean, J. (1998), 'A new reference spectrum for the EUV irradiance of the quiet Sun: 1. Emission measure formulation', *Journal of Geophysical Research: Space Physics* **103**(A6), 12077–12089.

Watson, M. (2012), *Common LISP modules: artificial intelligence in the era of neural networks and chaos theory*, Springer Science & Business Media.

Weare, B. C. and Nasstrom, J. S. (1982), 'Examples of extended empirical orthogonal function analyses', *Monthly Weather Review* **110**(6), 481–485.

Wei, Y., Pu, Z., Hong, M., Zong, Q., Ren, Z., Fu, S., Xie, L., Alex, S., Cao, X., Wang, J. et al. (2009), 'Westward ionospheric electric field perturbations on the dayside associated with substorm processes', *Journal of Geophysical Research: Space Physics* **114**(A12).

Wickert, J., Reigber, C., Beyerle, G., König, R., Marquardt, C., Schmidt, T., Grunwaldt, L., Galas, R., Meehan, T. K., Melbourne, W. G. et al. (2001), 'Atmosphere sounding by GPS radio occultation: First results from CHAMP', *Geophysical research letters* **28**(17), 3263–3266.

Wise, B. M. and Ricker, N. L. (1990), The effect of biased regression on the identification of FIR and ARX models, *in* '1990 Annual AIChE meeting, Paper 312v, Chicago'.

Wold, H. et al. (1966), 'Estimation of principal components and related models by iterative least squares', *Multivariate analysis* **1**, 391–420.

Wold, S. (1978), 'Cross-validatory estimation of the number of components in factor and principal components models', *Technometrics* **20**(4), 397–405.

Wold, S., Johansson, E. and Cocchi, M. (1993), 'PLS-partial least squares projections to latent structures', *3D QSAR in drug design* **1**, 523–550.

Wold, S., Ruhe, A., Wold, H. and Dunn, I. W. (1984), 'The collinearity problem in linear regression. The partial least squares (PLS) approach to generalized inverses', *SIAM Journal on Scientific and Statistical Computing* **5**(3), 735–743.

Woodman, R. and Hagfors, T. (1969), 'Methods for the measurement of vertical ionospheric motions near the magnetic equator by incoherent scattering', *Journal of Geophysical Research* **74**(5), 1205–1212.

Woodman, R., Rastogi, R. and Calderon, C. (1977), 'Solar cycle effects on the electric fields in the equatorial ionosphere', *Journal of Geophysical Research* **82**(32), 5257–5261.

Woodman, R. and Villanueva, F. (1995), Comparison of electric fields measured at F region heights with 150 km irregularity drift measurements, *in* '9th international symposium on equatorial aeronomy, Bali, Indonesia'.

Yamazaki, Y. and Kosch, M. J. (2015), 'The equatorial electrojet during geomagnetic storms and substorms', *Journal of Geophysical Research: Space Physics* **120**(3), 2276–2287.

Yamazaki, Y., Yumoto, K., Uozumi, T., Abe, S., Cardinal, M., McNamara, D., Marshall, R., Shevtsov, B. and Solovyev, S. (2010), 'Reexamination of the Sq-EEJ relationship based on extended magnetometer networks in the east Asian region', *Journal of Geophysical Research: Space Physics* **115**(A9).

Yamazaki, Y., Yumoto, K., Uozumi, T., Yoshikawa, A. and Cardinal, M. (2009), 'Equivalent current systems for the annual and semiannual Sq variations observed along the 210 MM CPMN stations', *Journal of Geophysical Research: Space Physics* **114**(A12).

Yizengaw, E., Moldwin, M. B., Mebrahtu, A., Damtie, B., Zesta, E., Valladares, C. E. and Doherty, P. (2011*a*), 'Comparison of storm time equatorial ionospheric electrodynamics in the African and American sectors', *Journal of Atmospheric and Solar-Terrestrial Physics* **73**(1), 156–163.
URL: *http://dx.doi.org/10.1016/j.jastp.2010.08.008*

Yizengaw, E., Moldwin, M. B., Zesta, E., Biouele, C. M., Damtie, B., Mebrahtu, A., Rabiu, B., Valladares, C. F. and Stoneback, R. (2014*a*), 'The longitudinal variability of equatorial electrojet and vertical drift velocity in the African and American sectors', *Annales Geophysicae* **32**(3), 231–238.

Yizengaw, E., Moldwin, M. B., Zesta, E., Biouele, C. M., Damtie, B., Mebrahtu, A., Rabiu, B., Valladares, C. F. and Stoneback, R. A. (2014*b*), The longitudinal variability of equatorial electrojet and vertical drift velocity in the African and American sectors, *in* 'Annales Geophysicae', Vol. 32, Copernicus Gesellschaft Mbh.

Yizengaw, E., Moldwin, M., Mebrahtu, A., Damtie, B., Zesta, E., Valladares, C. and Doherty, P. (2011*b*), 'Comparison of storm time equatorial ionospheric electrodynamics in the African and American sectors', *Journal of Atmospheric and Solar-Terrestrial Physics* **73**(1), 156–163.

Yizengaw, E., Zesta, E., Moldwin, M. B., Damtie, B., Mebrahtu, A., Valladares, C. E. and Pfaff, R. F. (2012), 'Longitudinal differences of ionospheric vertical density distribution and equatorial electrodynamics', *Journal of Geophysical Research: Space Physics* **117**(A07312).

Zakharenkova, I., Krankowski, A., Bilitza, D., Cherniak, I. V., Shagimuratov, I. and Sieradzki, R. (2013), 'Comparative study of foF2 measurements with IRI-2007 model predictions during extended solar minimum', *Advances in Space Research* **51**(4), 620–629.

Zell, A., Mamier, G., Vogt, M., Mache, N., Hubner, R., Doring, S., Herrmann, K.-U., Soyez, T., Schmalzl, M., Sommer, T. et al. (1995), 'Stuttgart neural network simulator', *User Manual, Version* **4**.

Zhang, D.-H., Xiao, Z., Hao, Y.-Q., Ridley, A., Moldwin, M. et al. (2011), Modeling ionospheric foF2 by using empirical orthogonal function analysis, *in* 'Annales Geophysicae', Vol. 29, Copernicus GmbH, p. 1501.

Zhang, M. L., Liu, C., Wan, W., Liu, L. and Ning, B. (2010), 'Evaluation of global modeling of M(3000)F2 and hmF2 based on alternative empirical orthogonal function expansions', *Advances in Space Research* **46**(8), 1024–1031.
URL: *http://dx.doi.org/10.1016/j.asr.2010.06.004*

Zhang, M., Liu, C., Wan, W., Liu, L. and Ning, B. (2009), A global model of the ionospheric F2 peak height based on EOF analysis, *in* 'Annales geophysicae: atmospheres, hydrospheres and space sciences', Vol. 27, pp. 3203–3212.